MODELS AND METHODS OF QUANTITATIVE SINGLE-FIBER REFLECTANCE SPECTROSCOPY OF TISSUE PROPERTIES

By

TENGFEI (OWEN) SUN

Bachelor of Science in Physics
Luoyang Normal University
Luoyang, China
2010

Master of Science in Plasma Physics
University of Chinese Academy of Sciences
Beijing, China
2013

Submitted to the Faculty of the
Graduate College of the
Oklahoma State University
in partial fulfillment of
the requirements for
the Degree of
DOCTOR OF PHILOSOPHY
December, 2019

MODELS AND METHODS OF QUANTITATIVE
SINGLE-FIBER REFLECTANCE SPECTROSCOPY OF
TISSUE PROPERTIES

Dissertation Approved:

Dr. Daqing Piao

Dissertation Adviser

Dr. Charles F. Bunting

Dr. John O'Hara

Dr. Ning Wang

ACKNOWLEDGEMENTS

I would like to give the most thanks and deepest gratitude to my advisor Dr. Piao. I am very lucky to have this strict, responsible and kind-hearted mentor during my Ph.D. training in OSU. He guided me through the difficulties in research with his unlimited enthusiasm and shaped me from a rough rock to a useful stone block with his great patience and skills.

I want to thank my committee professors Dr. Charles F Bunting, Dr. Ning Wang and Dr. John O'Hara and former member Dr. Daniel Grischkowsky for their valuable advices. They taught me the rigor of scientific research and how to present the results effectively.

I also want to express my thanks to Anqi Zhang and Guan Xu for their precious suggestions on my doctoral research and future career development.

Finally, I am greatly indebted to my parents, Gensheng Sun and Aiqin Liu, for their endless love and firm support to my academic pursuit. My thanks must also be extended to my elder sister Xiaorui Sun and brother in law Yonghua Liu. Without their generous support, I cannot make myself here. The words they told me, "Aim high, and work hard to get there", powers me to meet any challenge in front.

Name: TENGFEI SUN

Date of Degree: DECEMBER, 2019

Title of Study: MODELS AND METHODS OF QUANTITATIVE SINGLE-FIBER
REFLECTANCE SPECTROSCOPY OF TISSUE PROPERTIES

Major Field: ELECTRICAL ENGINEERING

Abstract: Single-fiber reflectance spectroscopy has unique clinical applications not amendable to other types of spectroscopy technologies when assessing a very small tissue domain. SfRS aims to quantify light propagation in the sub-diffusive regime by using a detection geometry that has the illumination and collection areas completely overlapped. This work presents models and methods of diffuse reflectance spectroscopy in a sub-diffusive domain that may be translated to single fiber reflectance spectroscopy (SfRS) measurements at steady-state and time-domain. By using Monte Carlo simulations and analytical approaches, this work specifically analyzes diffuse reflectance associated with a center-illuminated and area-collection round geometry (CIAC) that reveals patterns salient to SfRS, including the dependence on scattering anisotropy and scattering coefficient at low-scattering region, and independence on scattering over high-scattering region. Operating in this CIAC geometry with the tissue modeled as a semi-infinite homogeneous medium, this work demonstrates a few methods that are new to the modeling of diffuse reflectance at the scales relevant to SfRS: (1) two models of spatially-resolved diffuse reflectance applying to a scale as small as 10^{-5} of the reduced scattering pathlength that is two orders smaller than previously modeled are developed, (2) the total diffuse reflectance as the measurement is developed by taking the integration of the spatially resolved diffuse reflectance over the entire area of collection, (3) the analytical results reveal quantitatively the saturation level and the transition shoulder point that have been observed in steady-state SfRS measurements but without explanations. The analytical modeling approach demonstrated for steady-state measurements is also extended to time-revolved measurement for assessing the effect of absorption and scattering changes on the measurements. These models will be useful to rapid inversion for recovering tissue optical properties based on diffuse reflectance at a single-fiber scale.

TABLE OF CONTENTS

Chapter Page

Chapter Page

LIST OF TABLES

Table Page

LIST OF FIGURES

Figure Page

Figure Page

CHAPTER I

BACKGROUND AND INTRODUCTION

1.1 Basics of photon propagation in biological tissue

When photons propagate inside biological tissue, they are consistently scattered by various types of ultrastructure ranging from membranes to membrane aggregates to collagen fibers to nuclei to whole cells, as well as being absorbed by many optical absorbers which are primarily hemoglobin of different types, water, lipid, and melanin. Basic optical properties of biological tissue and their definition are summarized in Table below[1].

Table I-1 Basic optical parameters of biological tissue

Parameter	**Symbol**	**Typical value**	**Unit**
Absorption coefficient	μ_a	0.01	mm^{-1}
Scattering coefficient	μ_s	10	mm^{-1}
Anisotropy factor	g	0.9	dimensionless
Reduced scattering coefficient	$\mu_s' = \mu_s(1-g)$	1	mm^{-1}
Refraction index	n	1.4	dimensionless

The probability distribution of scattering angle over the while 4π solid angle is characterized by scattering phase function $p(\theta)$, and the anisotropy g represents the average value of cosine of scattering angle θ, which is expressed by following equation.

$$g = \langle cos\theta \rangle = \int_0^{2\pi} \{ \int_0^{\pi} \cos(\theta)\, p(\theta) \sin(\theta)\, d\theta \} d\phi \tag{I-1}$$

Henyey-Greenstein (HG) phase function, initially developed in astrophysics to describe scattering of light by interstellar dust clouds, is widely used to describe light scattering event in biological tissue due to its simplicity. As express in following equation, the structure of HG phase function is designed to possess these features: 1) giving any $g \in [-1,1]$, the integration of $p_{HG}(\theta)$ over 4π solid angle leads to one; 2) giving any g value in the range of $-1 < g < 1$, such as g = 0.9 corresponding an averaged scattering angle of ~26^0 , $p_{HG}(\theta)$ quantifies the probability distribution of any possible scattering angle between $[0,180^0]$ and meet the anisotropy definition as expressed in Equation (I-1).

$$p_{HG}(\theta) = \frac{1}{4\pi} \frac{1-g^2}{[1-g^2+2g\cos(\theta)]^{3/2}} \tag{I-2}$$

Since most biological tissue is strong scattering medium and anisotropy g only varies in small range, reduced scattering coefficient μ_s', as a compositive property that incorporates scattering coefficient μ_s and the anisotropy g, is commonly used in diffusion theory to describe photon scattering.

Light absorption is weak in the visible and near-infrared (VIS/NIR) spectral region between 400nm-1350nm. Photons take a mean free scattering path length on the order of 0.1mm between two adjoining scattering events, while the mean free absorption path length can range from 10mm to 100mm. Particularly, the wavelength range of 650nm to 1350nm where the light has its maximum penetration depth, is identified as near-infrared (NIR) optical windows and widely used for tissue diagnosis or therapeutical monitoring. The following Figure I-1 presents the absorption spectrum of typical biological absorbers in tissue, and the NIR optical windows are high-lighted with yellow background.

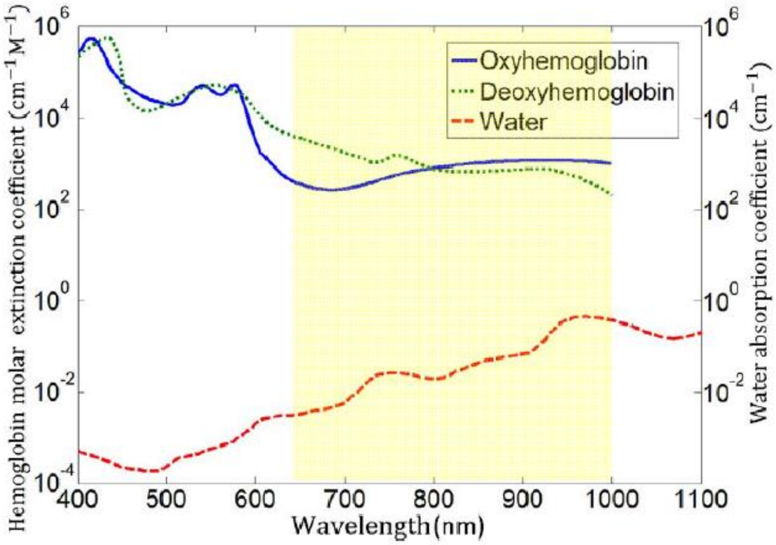

Figure I-1 Absorption spectrum of primary biological absorbers in tissue and NIR optical window ([1]Lihong Wang et.al. 2012)

1.2 Single-fiber reflectance spectroscopy for tissue properties measurement

1.2.1 Single-fiber scale measurement and its unique advantages

Diffuse reflectance spectroscopy using a single-fiber applicator probe both for light delivery and collection, often referred as single-fiber reflectance spectroscopy (SfRS), is featured by small form-factor, simple set-up, compact size and low cost and possess the clinical potentials of bedside use. As pictured by Figure I-2, the single fiber probe can be a single solid fiber, or a pair of fibers bound together, or one fiber bundle that contains many small optical fiber randomly divided to illumination branch and collection branch. The diameter of single fiber probe in biomedical application ranges from $100\mu m$ to $1000\mu m$ for type 1 probe, and 1mm-2mm for type 2 and type 3 probes[2].

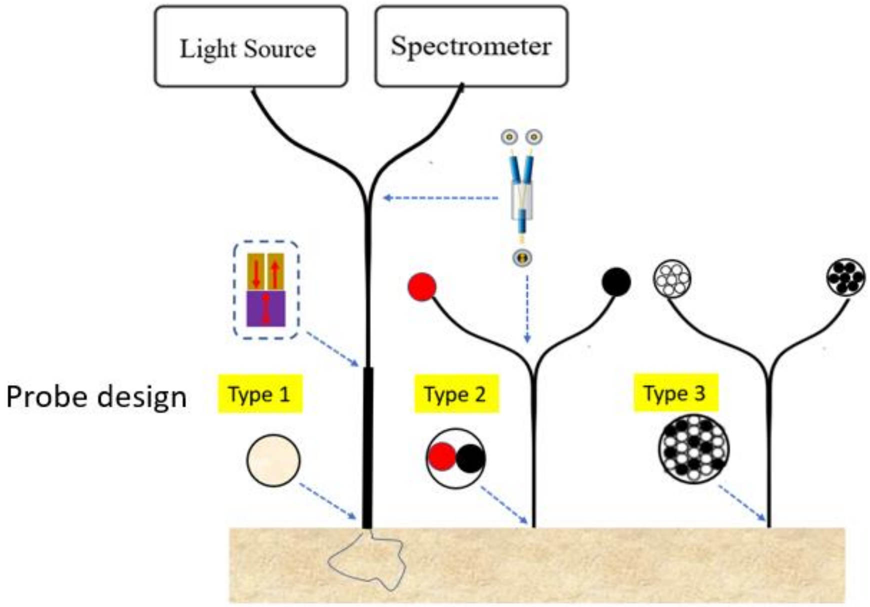

Figure I-2 The probe designs of single-fiber reflectance spectroscopy

The unique advantageous of single fiber scale measurement lies in non-invasive or minimum-invasive tissue diagnosis or monitoring, especially when tissue probing window is spatially constrained or difficult, such as one requiring endoscopic instrument channel or interstitial deployment[3-16].

Single-fiber reflectance spectroscopy can be configured in steady-state (or continue wave), time-domain and frequency-domain. Fluorescence technique that relies on the measurement of fluorescence emission form exogenous fluorophore injected into investigated tissue, can be combined with any of above three configurations, termed as fluorescence SfRS. This work mainly focuses on steady-state and time-domain configurations.

1.2.2 Clinical applications of SfRS

Currently almost all clinical applications with SfRS adopts the steady-state configuration, and only one paper demonstrates time-domain SfRS in a phantom experiment[17]. No literature is found with frequency-domain SfRS. Compared to time-domain and frequency-domain configuration, steady-state SfRS can be instrumented with lowest cost. Another important reason is the availability of an semi-empirical model [2, 18-20]for steady-state SfRS. This steady-state model was initialized in 2009 by a group in Amsterdam and has enabled many clinical applications with SfRS related to diagnosis of lung cancer, hepatics steatosis, bladder cancer, cervical cancer, et.al., as well as in vivo monitoring of oxygen saturation level, as will be described below.

Stephen, et.al., incorporated SfRS probe into the endoscopic ultrasound fine-needle aspiration procedure for lung cancer staging, and demonstrates the capability of SfRS of detecting differences in the physiology between normal and metastatic lymph nodes[21].

Piao, et.al. utilized percutaneous SfRS measurement to assess the scattering change of nucleus pulposus cause by intervertebral disc herniation disease in chondrodystrophic dogs, and found percutaneous SfRS may be useful as an in situ sensing tool for assessing the level of mineral degeneration in intervertebral disc for the prospect of disc-specific dosage adjustment in percutaneous laser disc ablation [11, 14]. This percutaneous SfRS was also applied to assess the scattering change of fatty liver tissue, and it showed that the elevation of scattering power due to morphological change of lipid droplet may be an early indicator of diet-induced hepatic steatosis.[8, 9].

Sun, et.al. applied SfRS to explore the spectroscopic feature associated with bladder cancer in rat model in vivo, and found that the elevated methemoglobin proportion in the context of increased total hemoglobin concentration may indicate different level of cancerous change [12].

Yu, et al, demonstrated a SfRS system that uses reflectance mirrors and beam splitter instead of commonly used bifurcated fibers for light delivery and router, and applied it to the in vivo monitoring of oxygen saturation level in rat deep brain[4, 10].

Paulien L, et.al. applied SfRS to the optical guidance during endoscopic ultrasound-guided fine needle aspirations (EUS-FNA) of pancreatic masses, and demonstrated its ability to distinguish benign from malignant pancreatic tissue [16].

Tabrizi et.al. compared the performance of SfRS in detection of cervical pre-cancerous squamous intraepithelial lesions with the regular colposcopy in a Phase III trial, and the results showed that SfRS can reduced the number of unnecessary biopsies by a factor more than 5.5. [3, 15].

1.2.3 Implementation of steady-state SfRS

Steady-state SfRS is the most common used implementation due to its low cost and simple setup. Figure I-3 illustrates the principle of steady-state SfRS and one example of implementation with bifurcated optical fiber[12, 14, 22, 23]. Steady-state technique only measures the intensity change that is modulated by tissue scattering and absorption. The system consists of a broadband light source, a spectrometer, and light delivery equipment which adopts bifurcated fiber and a single fiber probe. The spectrum of a broadband light source commonly covers from visible to near-infrared range, and may include ultra-violet. The spectrometer detects photons reemitted from tissue and generates spectrally-resolved reflectance signal. The probe at distal end both injecting light into and collecting remitted light from tissue, can be either a single-fiber probe or a single fiber-bundle probe which bundles small fibers together to form a larger probe dimension.

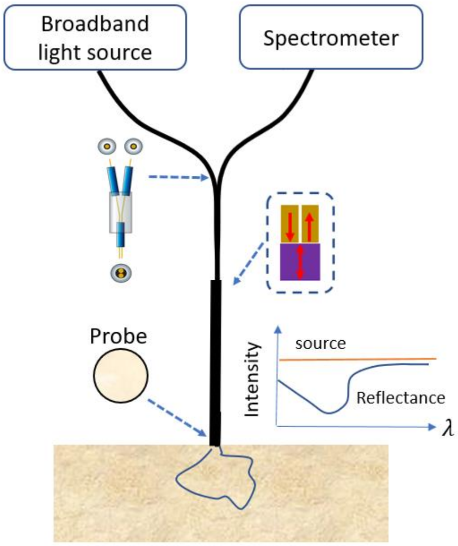

Figure I-3 Principle and implementation of steady-state SfRS

1.2.4 Implementation of time-domain SfRS

Time-domain technique injects an extremely short pulse of light into tissue and measures the arrival time of reemitted photons that represents the path length one photon travels inside tissue. Hence, it provides the richest information about tissue morphology and physiology. However, time-domain implementation is very expensive in cost and requires high-speed gating devices. Until now only one publication was found to experimentally develop the time-domain SfRS system[17].

Figure I-4 presents the principles of time-domain technique, as well as one example of system implementation. Time-domain SfRS utilizes a pulsed laser to fire an extremely short pulse and used an ultrafast time-gated single photon avalanche diode (time-gated SPAD) as detector to measure temporal response from tissue. The probe at distal end both injecting light into and collecting remitted light from tissue, can be either a single-fiber probe or a single fiber-bundle probe which bundles small fibers together to form a larger probe dimension.

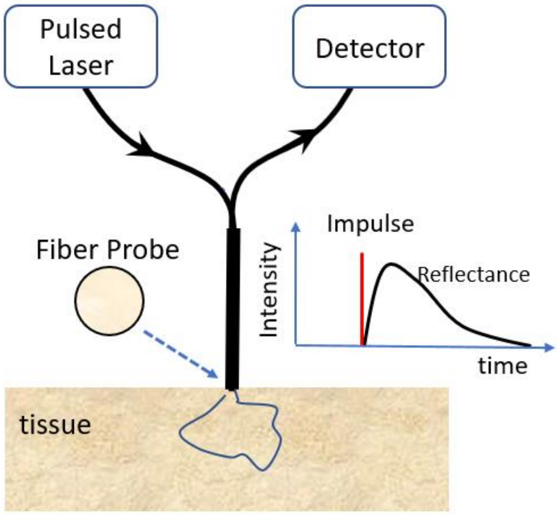

Figure I-4 Principle and implementation of time-domain SfRS

1.3 Reviews of current model development of SfRS

Due to the difficulties of quantifying light transportation in sub-diffusion regime and calculating convolution for an overlapped illumination and collection geometry, the exact analytical solution to spatially resolved diffuse reflectance as well as total diffuse reflectance collected from biological tissue has been void for years. Thus, the current models of steady-state and time-domain SfRS were developed empirically under the framework of beer-lambert law.

1.3.1 Methods of describing of photon propagation in biological tissue

Photon propagation in biological tissue can be modeled analytically by radiative transfer equation (RTE) or Boltzmann equation as expressed below in spherical coordinate system, where L is radiance, $\vec{r}$ is the spatial vector of observation point, $\mu_t = \mu_s + \mu_a$ is extinction coefficient or total interaction coefficient, $\hat{s}$ is unit direction vector, $\hat{s}'$ is the unit direction vector of light propagation, $P(\hat{s}' \cdot \hat{s})$ is scattering phase function, Ω' is solid angle, and $S(\vec{r}, \hat{s}, t)$ is the source.

$$\frac{\partial L(\vec{r},\hat{s},t)}{c\partial t} = -\hat{s} \cdot \nabla L(\vec{r},\hat{s},t) - \mu_t L(\vec{r},\hat{s},t) + \mu_s \int_{4\pi} L(\vec{r},\hat{s}',t) P(\hat{s}' \cdot \hat{s}) d\Omega' + S(\vec{r},\hat{s},t) \qquad \text{(I-3)}$$

The RTE follows the principle of conservation of energy. The left-hand term represents the changing rate or the power of radiation per unit volume per unit solid angle, the first term at right-hand side represents the energy divergence out of the volume element, the second term at right-hand side represents the energy loss due to scattering and absorption, and the third term at right-hand side represents energy incident due to scattering.

Though RTE accurately describes the light propagation in tissue, it is very difficult to solve. Therefore, approximations such as δ-P_N [24-26] which adds a Dirac-δ function to the Nth order of Legendre polynomial expansion of radiance, is sought to arrive at a specific solution to a certain geometry.

Diffusion approximation assumes the radiance in high-albedo ($\mu_a \ll \mu_s$) scattering medium is nearly isotropic after sufficient scattering, under which the radiance is expanded as the 1st order of spherical harmonics. Thus, the RTE could be simplified to diffusion equation (DE) as shown below with the fluence rate term Φ.

$$\frac{\partial\Phi(\vec{r},t)}{c\partial t} = D\nabla^2\Phi(\vec{r},t) - \mu_a\Phi(\vec{r},t) + S(\vec{r},t) \qquad \text{(I-4)}$$

However, the diffusion theory normally fails to quantify the photon propagation in non-diffusion regime and the tissue conditions with strong absorption. Enhanced diffusion-based models[27] were reported to overcome this limit. Piao et.al. reported a master-slave dual source model[28] which is demonstrated to be able to quantify the spatially resolved diffuse reflectance collected from a semi-infinite geometry associated with a pencil beam input over the range of the dimensionless $\rho\mu_s'$ as close as 0.01. Xu reported a model[29] base on small angle approximation (SAA) that pushed the its working range one order closer to incident point, $\rho\mu_s' = 0.001$.

Besides above analytical approaches to describe photon propagation in tissue, Monte-Carlo (MC) method is also utilized to solve RTE as summarized in review article [30]. Compared to standard diffusion approximation, MC method could offer solution of high accuracy with price of high computation cost.

Empirical models that were developed by comparing with MC simulated results and/or phantom experiment are also reported in literatures [2, 20, 31-35]. Artificial neural network based model were also reported to model spatially-resolved diffuse reflectance spectra for retrieving scattering and absorption properties[36-38].

1.3.2 Current steady-state model and its limitation

Steady-state SfRS application currently employs a set of semi-empirical forward models that were initiated in 2009 and finalized in 2012 by Dr. Stephen C. Kanick's group [2, 18-20, 32, 34, 35, 39]. This model sets, built upon observations on and calibrations with data from Monte-Carlo simulations and phantom experiments, adopts the framework of modified beer-lambert law to account for the effects of scattering and absorption as shown in equation below, where μ_a is absorption coefficient, μ_s' is the reduced scattering coefficient, $R_{scat}(\mu_s')$ is the SfRS intensity of absorption-free case, and $< L(\mu_a, \mu_s') >$ is the average photon path length.

$$R_{SfRS}(\mu_a, \mu_s') = R_{scat}(\mu_s') \exp(-\mu_a \langle L(\mu_a, \mu_s') \rangle) \qquad \text{(I-5)}$$

During the four years modeling process, the model sets evolved and brought out several versions. Among which the one most commonly used in many steady-state SfRS clinical studies[3, 4, 8, 9, 11, 14, 15] is their intermediate version as shown in equation below, where η_{lim} is a collecting efficiency of the fiber imposed by the numerical aperture, and $[\, p_1 \;\; p_2 \;\; p_3 \;\; C_{PF}]$ are a set of parameters dependent on scattering phase function of the medium, substituted by an optimal set of constant values $[1.55, 6.82, 0.97, 0.944]$ reported in Kanick's study[34].

$$R_{SfRS}(\mu_a, \mu_s') =$$

$$\eta_{lim}\left[1 + p_1 \cdot exp(-p_2 \mu_s' \, d_{fib})\right]\left[\frac{(\mu_s' \, d_{fib})^{p_3}}{p_2 + (\mu_s' \, d_{fib})^{p_3}}\right] exp\left(-\mu_a \frac{1.54 C_{PF} \, d_{fib}}{(\mu_s' \, d_{fib})^{0.18}[\, p_6 + (\mu_a \, d_{fib})^{0.64}]}\right) \qquad \text{(I-6)}$$

While the final version that represents $[p_1, p_2, p_3, C_{PF}]$ as γ -specific parameter set $[0.63\gamma^2, 2.31\gamma^2, 0.57\gamma, 0.68\gamma^{0.6}]$ is not widely adopted by the community. The reason is that this γ-

specific version need co-work with a novel methodology of multi-diameter single fiber reflectance spectroscopy (MDSfRS) proposed and tested by Kanick's group[33-35, 39, 40] to extract wavelength-dependent $\gamma(\lambda)$, $\mu_s'(\lambda)$ and $\mu_a(\lambda)$. But the MDSfRS methodology also brings disadvantages that may limit its practical use in clinical studies, which includes:

1) Increased system complexity. Need a special apparatus to control the fiber diameter and location of a source-detector spot projected onto the fiber bundle.

2) The difficulty of ensuring a colocalized sampling volume when measuring with different fiber diameter.

3) Increased number of measurements and longer data acquisition time.

The currently used semi-empirical model in above equation has powered many clinical studies. However, its empirical origination of current forward models may limit its practical use in resolving complex tissue. Yu, et.al. reported that a negative value of oxygen saturation level ~ 8% was returned from data fitting by using current semi-empirical model, as shown by the black line in following figure which is directly cropped from Yu's publication[10]. The Oxygen saturation level of ~ 8% which goes beyond the physical range and makes the incorrect sense, may be attributed to empirical nature of current model that separates absorption and scattering by the framework of Beer-Lambert law.

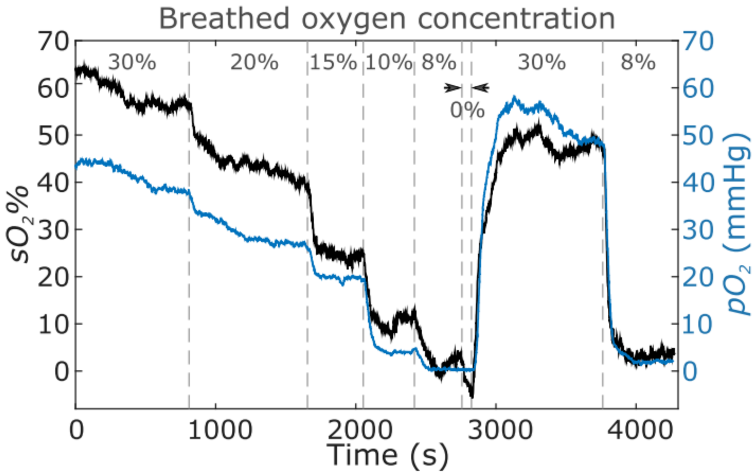

Figure I-5 Negative oxygen saturation level of ~8% was returned from the data fitting with current semi-empirical model (black line)[10]

The author of this dissertation also encountered similar issue when using current model in data fitting to quantify the proportion of methemoglobin from reflectance spectrum measured from rat bladder tissue in vivo as detailed in Chapter II. Certain extracted parameters such as oxygen saturation level, went beyond the physical range of biological tissue when applying the model to data fitting over entire wavelength range. Some fitted curves of reflectance spectrum display artifact of methemoglobin spectral signature around 635nm compared with experimental data, as shown by following figure.

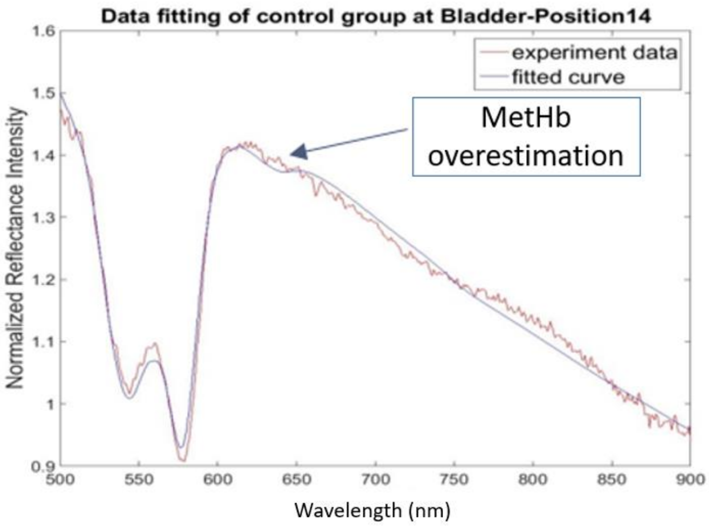

Figure I-6 The fitted curve of reflectance spectrum(blue solid line) shows artifact of methemoglobin spectral signature around 635nm compared with experimental data(red line)

1.3.3 Current time-domain model and its limitation

Time-domain SfRS was first demonstrated experimentally in 2012 by Erik, et al.[17], and so far their study remains the only published work in this field. As shown in Equation 3, an incomplete empirical model that is based on observation on Monte-Carlo simulated data, was adopted to approximately describe time-resolved diffuse reflectance.

$$y_{diff}(\mu_a, \mu_s', t) = k_d(\mu_s')y_0(t)\exp(-\mu_a v t) \tag{I-7}$$

Where $k_d(\mu_s')$ is a coefficient describing the intensity of diffuse reflectance, $y_0(t)$ is the shape of diffusely reflected curve, and v is the light speed in medium.

This is an incomplete empirical model with the framework of beer-lambert law to organize scattering contribution and absorption contribution. Both $k_d(\mu_s')$ and $y_0(t)$ have no concrete expression. To extract μ_a through data fitting, $k_d(\mu_s')$ has to be set as free parameter and $y_0(t)$ is generated by Monte-Carlo simulation at one fixed tissue condition chosen by empirical observation but used for all fittings, as described in their paper. The incompleteness of this model also makes it impossible to extract scattering information from measured time-resolved SfRS signal. More applications of time domain SfRS is impeded by inadequate understanding of the measurement characteristics.

1.4 Overview of this work

Motivated by addressing the limitations of current model encountered in experimental study with steady-state SfRS, the objective of this dissertation includes two aspects: 1) develop analytical-driven models of SfRS in steady-state and time-domain configurations for more robust extraction of tissue optical properties 2) demonstrate the modeling methodology that could be potentially transferred to frequency-domain SfRS and fluorescence SfRS, as well as other probing geometries more complex than single-fiber.

The layout of this dissertation is: Chapter II presents an experimental investigation of spectroscopic feature related to bladder cancer by using steady-state SfRS technique. Chapter III presents an analytical steady-state total diffuse reflectance over a $1/\mu_s'$ scaled dimension of [10^{-5}, 10^{-1}] centered at the point-of-incidence from a semi-infinite medium with an HG anisotropy. Chapter IV demonstrates a model of total diffuse reflectance collected from a center-illumination and area-collection geometry by integrating a spatial diffuse reflectance model constructed by concatenating two models for diffusive and sub-diffusive region, as validated by numerous MC simulations and phantom experiment. Chapter V provides analytical perspectives to three characteristics of steady-state SfRS based on model demonstrated in Chapter IV. Chapter VI presents a promising time-domain model of SfRS by transferring the methodology demonstrated in steady-state work. Chapter VII summarizes the contribution of this dissertation research and projects the future research topics associated with SfRS.

CHAPTER II

IN VIVO STEADY-STATE SFRS STUDY OF BLADDER CANCER IN A RAT MODEL

2.1 Introduction

Urinary bladder cancer ranks as the fourth most common cancer in men and the tenth most common cancer in women in the United States [41]. Bladder cancers are usually detected by cystoscopy [42], and transurethral resection of the bladder tumor (TURBT) is used to remove the tumor [43]. Unfortunately, flat lesions of bladder cancer often evade cystoscopy, making adequate detection as well as complete removal of bladder cancer by TURBT at the time of resection a challenge [44]. Inadequate detection and removal of bladder tumor increases tumor recurrence [5] and the risk of cancer metastasis [45]. The frequent tumor recurrence requiring life-long surveillance and management has made bladder cancer one of the most expensive cancers to treat from diagnose to the death caused by cancer.

Among the new modalities that can be integrated with cystoscopy for bladder cancer detection, two promising techniques are blue-light cystoscopy (BLC) and optical coherence tomography (OCT). BLC visualizes blue-light excited fluorescence of intravesically administered hexylaminolevulinate acid [46] that drives the accumulation of protoporphrin IX (PpIX) in malignant cells. Some other dyes have also been shown to accumulate in bladder tumor [47] as a result of the enhanced permeability and retention effect [48]. OCT is powerful for high-resolution depth-resolved imaging of tissue micromorphology including vasculature [49] These imaging modalities have significantly enhanced the potential of detecting bladder lesions difficult to identify under regular cystoscopy that images surface reflection morphology in high resolution.

This study has used diffuse reflectance spectroscopy (DRS) implemented with a single-fiber probe to explore if bladder cancer reveals potential spectroscopic features associated with neoplastic changes, and if it does, whether there is a correlation between the extent of the spectral features and the extent of neoplastic changes. DRS in the visible and near-infrared band [50] is sensitive to bio-chemical compositions of tissue chromophores including hemoglobin of different oxygen binding capacities, cytochrome oxidase, water and lipid that may collectively infer degraded microenvironment [51], and sensitive to subcellular structural variations that alter tissue scattering properties [52]. The physiological information offered by light interrogation of tissue absorption and scattering has thus rendered DRS useful for meeting some challenging needs, such as tumor margin determination in breast surgery [53-55]. In evaluating the potential of DRS for bladder cancer detection, a single-fiber probe that illuminated tissue and acquired the diffusely reflected light from tissue using the same small fiber was implemented for its potential of future applicability within the instrument channel of a cystoscope. Reflectance spectroscopy using a single-fiber probe or a probe of small end-profile allowing insertion through needle or an endoscopic port has been demonstrated for staging of lung cancer through examination of mediastinal lymph nodes [21], brain tumor detection [22], intra-operative differentiation of healthy and demyelinated peripheral nerves [23], and prediction of cervical squamous intraepithelial lesions [24], etc. In this study, the application of single-fiber reflectance spectroscopy (SfRS) on an orthotopic bladder carcinoma tumor model in rat bladder has revealed a spectral feature in tumorous tissues that is characteristic of methemoglobin (MetHb)—the hemoglobin compound that has lost the oxygen-transporting capacity [25] and shown to associate with neoplastic development of several types of human tumor cells [26]. The study has indicated both an increased total hemoglobin content and an increased MetHb proportion within the total hemoglobin content in tumorous rat bladder tissues, when compared to normal bladder tissue.

2.2 Materials and methods

2.2.1 Single-fiber reflectance spectroscopy system

The diffuse reflectance spectroscopy system using a single-fiber probe as shown in Figure 1(A) was assembled on a custom-modified stainless-steel cart. The system consisted of a broadband light source, a compact spectrometer, a single-fiber-probe mounted on a translation stage with 5-degrees of freedom, a personal computer for acquiring the spectral data, and accessories. A deuterium tungsten halogen light source (model DH2000-FHS, Ocean Optics Inc., Dunedin, FL) [27] was coupled to one branch of a 200-μm diameter bifurcated fiber bundle (BIF 200-VIS/NIR, Ocean Optics Inc., Dunedin, FL). Only the halogen source was used after evaluating the overall spectral response of the system. The other end of the bifurcated fiber bundle was connected to a compact spectrometer (NT58-303; Edmund Optics Inc., Barrington, NJ, USA) [28, 29], which has a spectral response over 450 – 1000 nm as shown in Figure 1(B). The combined end of the bifurcated fiber bundle was connected to a low-OH fiber of 320 μm in diameter (H320R; New Star Lasers Inc., Roseville, CA, USA) for light delivery to and collection from the tissue. The tip of the single-fiber probe was polished in-house to an angle of ~15 degree [27-29] to reduce specular back reflection. The single-fiber probe was mounted on a stage with 3 degrees of freedom for linear translation and two degrees of freedom for rotation, as shown in Figure 1(C). The stage with 5-degrees of freedom rendered quick adjustment of the angle-polished fiber-probe for just-in-contact with the arbitrarily oriented tissue surface. A large vertically translating stage was placed under the single-fiber probe for placing the object to be measured and quickly bringing the object (e.g., the exposed rat bladder as shown in Figure 1(D)) closer to the fiber probe. The single-fiber probe was subsequently adjusted with 5-degrees of freedom to make consistent fiber-tissue contact. The assembly consisting of the fiber-optical probe, the fiber positioning stages, and the sample lifting stage was covered by a black cloth to reduce ambient light. The reflectance spectrum collected by the single-fiber probe from the tissue was acquired and displayed by using a BWSpec 3.26 software (B&W Tek, Newark, DE) after averaging over 10 measurements at an individual exposure time of 500ms. Each spectrum was saved individually for post-processing using the method of analysis as detailed in the later section.

2.2.1Animal Protocol

This study was approved by the Institutional Animal Care and Use Committee of the Oklahoma University Health Sciences Center. The study involved six female Fisher rats (CDF® [F-344]) separated randomly to two rats as controls and four rats as the tumor group that were given intravesical tumor-cell instillation. Of the four rats in the tumor group, a suspension of AY-27 cells was instilled to the urinary bladder by urethral catheterization [30]. At 7 days post-instillation of the AY-27 cells, all animals were anesthetized using isoflurane and placed in a supine position on a water-warmed heating pad (37°C). The abdomen was opened and urinary bladders were bisected to two connected halves to expose the mucosal side of the bladder. The single-fiber probe was then brought into contact with the exposed bladder tissue, in the area grossly inspected to be normal or tumor-bearing. SfRS measurements at fatty tissues in the peripheral of the exposed bladder as well as skin tissue not covered by fur were also performed to establish reference measurements from well identified tissue. On gross examination, the exposed bladder tissue of the rats in the control group appeared normal. On gross examination, the exposed bladder tissue of the rats in the AY-27 instilled group had single or multiple focal lesions indicating abnormal development.

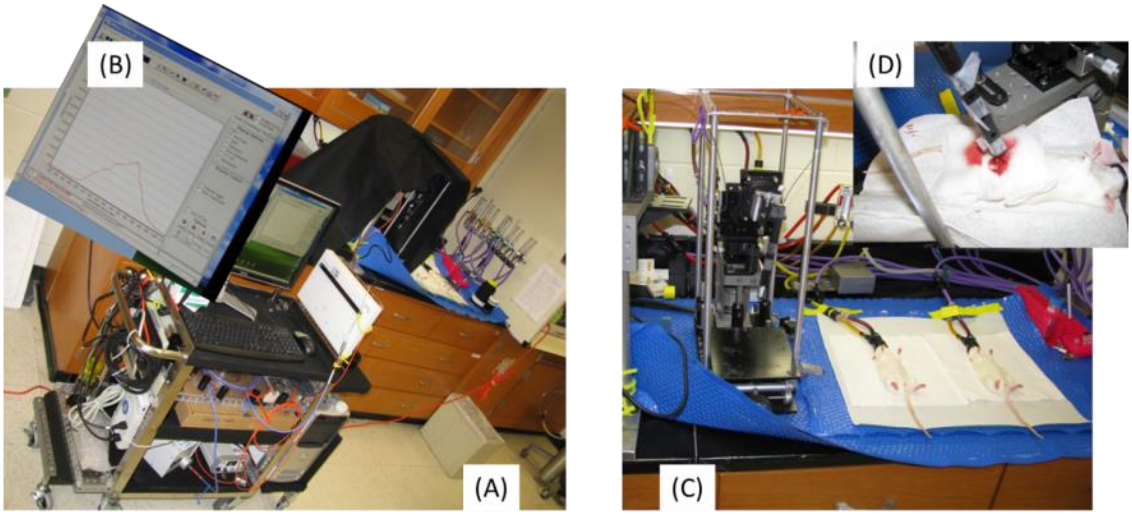

Figure II-1 (A) The experimental setup consisting of the single-fiber reflectance spectroscopy unit and the bench for animal work. (B) Screenshot of the spectrometer display. (C) The single-fiber probe mounted to a stage with 5 degrees of freedom, aside the rats under anesthesia. (D). Close-up view of the single-fiber probe in contact with a halved rat bladder.

A total of 107 SfRS measurements were taken from tissue sites corresponding to grossly normal or tumor-bearing on the bisected halves of the bladders of 6 rats. Among the 107 SfRS measurements, 27 were from grossly-normal bladder tissues of the rats in the control group, and 80 were from bladder tissues of rats in the AY-27 group that were grossly examined as tumor-bearing. After each measurement, the single-fiber probe of 320µm was slightly repositioned to another location; therefore no two SfRS measurements were from the same position on the exposed bladder wall. For any tumor-bearing site of a couple of millimeters in size that was substantially greater than the diameter of the fiber-probe, SfRS measurements were taken from multiple positions within the same tumor-bearing lesion. After completion of the SfRS measurements, the animals were humanly euthanized. The two connected halves of the bladder were then separated, removed, and fixed in 10% buffered formalin. The bladder specimens were embedded in paraffin, and tissue sections of 5 µm were prepared with a cryostat microtome and stained with haematoxylin-eosin (H&E) for histological examination.

2.2.3 Model analysis of the SfRS signal

The analytical method of SfRS used for estimating the chromophore contents of the rat bladder tissue was adapted from a model that has been applied to SfRS studies of two tissue conditions with significantly different chromophore compositions: 1) scattering changes in the degeneration of canine intervertebral disc that had minimal interference from blood absorption because of the avascularity of the intervertebral disc [28, 29] and 2) scattering changes in rat liver as a result of steatosis development that was strongly interfered by absorption [27] of chromophores in hepatic tissue.

The principle of SfRS is schematically illustrated in Figure 2.2. Light from a broadband source is coupled to a single-fiber probe by a bifurcated fiber coupler which is also connected to a compact spectrometer. The bifurcated fiber couple is consisted of fibers of 200µum, and the single-fiber probe has a diameter of 320µm.

The light source has a native spectral profile of $S(\lambda)$ for coupling into the tissue by a fiber-optical probe. The light when recollected by the same fiber-probe used for illumination has experienced many scattering events in tissue in addition to absorbing events associated with tissue chromophores, making the spectrum of the collected light modulated by the chromophore absorption and tissue scattering spectrum. We denote the baseline spectral profile as $S(\lambda)$ and neglect the spectral artifact due to internal reflection. The spectral reflectance from the tissue is then modeled as [27-29]

$$R_{tissue}(\lambda) = \eta_c \cdot \left[\bar{R}_{scat}(\lambda) \cdot exp\{-\mu_a(\lambda)\langle L(\lambda)\rangle\} + \eta_{fiber/tissue}\right]S(\lambda) \tag{II-1}$$

where η_c is the collection efficiency of a single-fiber probe , $\bar{R}_{scat}(\lambda)$ represents the contribution of tissue scattering to single-fiber reflection in the absence of absorption, $\mu_a(\lambda)$ is the absorption coefficient of tissue, $\langle L(\lambda)\rangle$ denotes the average pathlength of the photon between injecting into tissue and collecting by the same fiber [31], and $\eta_{fiber/tissue}$represents the Fresnel reflection at the fiber/tissue interface.

The single-fiber reflectance signal from the tissue was normalized by using reference signals acquired in air and in water [27-29] for isolating the tissue contribution to the measured spectrum. The reference signals from the air and water are respectively modeled as

$$R_{air}(\lambda) = \eta_c \cdot \eta_{fiber/air}S(\lambda) \tag{II-2}$$

$$R_{water}(\lambda) = \eta_c \cdot \eta_{fiber/water}S(\lambda) \tag{II-3}$$

With which the tissue modulation to the single-fiber spectral reflectance is obtained by the following normalization

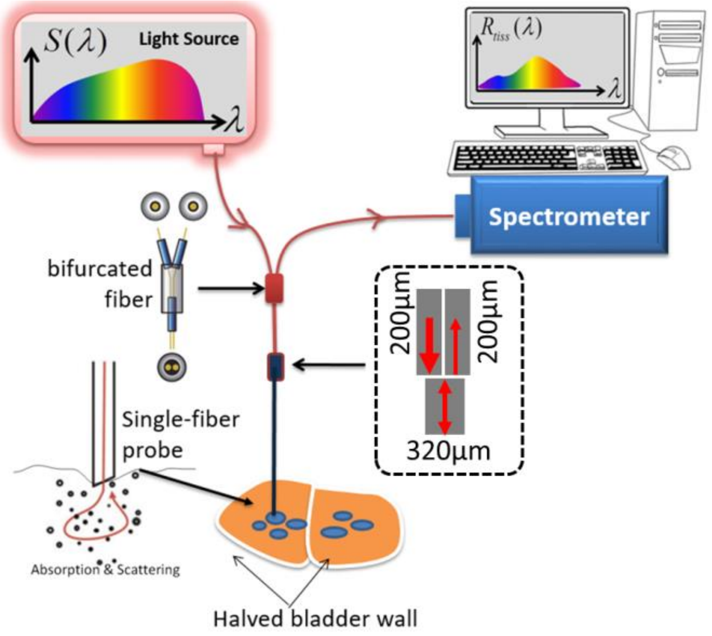

Figure II-2 Schematic diagram of the single-fiber reflectance spectroscopy probing of the mucosal side of the halved urinary bladder.

$$R_{norm}(\lambda) = \frac{R_{tissue}(\lambda)-R_{water}(\lambda)}{R_{air}(\lambda)-R_{water}(\lambda)} = \xi \cdot \bar{R}_{scat}(\lambda) \cdot exp\{-\mu_a(\lambda)\langle L(\lambda)\rangle\} \qquad \text{(II-4)}$$

where ξ is a constant arising during the algebraic procedures. The scattering-contribution to the reflectance as represented by $\bar{R}_{scat}(\lambda)$ and the average photon pathlength in tissue as denoted by $\langle L(\lambda)\rangle$ are reported to follow a set of semi-empirical formulae according to Monte Carlo and experimental SfRS studies [31] as

$$\bar{R}_{scat}(\lambda) = \eta\left(1 + p_1\, exp\left[-p_3\mu_s'(\lambda)d_{fib}\right]\right)\frac{\left[\mu_s'(\lambda)d_{fib}\right]^{p_2}}{p_3+\left[\mu_s'(\lambda)d_{fib}\right]^{p_2}}_{lim} \qquad \text{(II-5)}$$

$$\langle L(\lambda)\rangle = \frac{p_4 \cdot d_{fib}}{\left[\mu_s'(\lambda)d_{fib}\right]^{p_5}\left\langle p_6+\left[\mu_a(\lambda)d_{fib}\right]^{p_6}\right\rangle} \qquad \text{(II-6)}$$

In this study the tissue absorption is attributed to five chromophores, including oxygenated hemoglobin (OxyHb), deoxygenated hemoglobin (DeoxyHb), methemoglobin (MetHb), lipid, and water. Within the total blood content that is represented by $[Hb]_{total}$, the concentration proportion of OxyHb is denoted as

f_{OxyHb} , and MetHb as f_{MetHb} . Within the water-lipid composite that occupies a volume fraction of $V_{Water\&Lipid}$ of tissue, the proportion of lipid is represented as f_{lipid}. The tissue absorption thus becomes

$$\mu_a(\lambda) = \left[\hat{\mu}_a^{OxyHb}(\lambda) f_{OxyHb} + \hat{\mu}_a^{DeoxyHb}(\lambda)(1 - f_{OxyHb} - f_{MetHb}) + \hat{\mu}_a^{MetHb}(\lambda) \times f_{MetHb}\right][Hb]_{total} + \left[\hat{\mu}_a^{Lipid}(\lambda) f_{Lipid} + \hat{\mu}_a^{Water}(\lambda)(1 - f_{Lipid})\right] v_{Water\&Lipid} \quad \text{(II-7)}$$

where $\hat{\mu}_a^{OxyHb}$, $\hat{\mu}_a^{DeoxyHb}$, $\hat{\mu}_a^{MetHb}$, $\hat{\mu}_a^{lipid}$ and $\hat{\mu}_a^{water}$ are respectively the absorption coefficient (unit: mm^{-1}) of 1 μM oxygenated hemoglobin, of 1 μM deoxygenated hemoglobin, 1 μM methemoglobin, of pure lipid (100% volume fraction) and of pure water (100% volume fraction). $[Hb]_{total}$ is the total hemoglobin concentration (unit: μM) combining OxyHb, DeoxyHb, and MetHb. The $\hat{\mu}_a^{OxyHb}$, $\hat{\mu}_a^{DeoxyHb}$, $\hat{\mu}_a^{lipid}$ and $\hat{\mu}_a^{water}$ were extracted from the “Spectral Panel” of VirtualPhotonics [32] with a resolution of 1nm within the spectral range corresponding to the spectral analysis on the tissue measurements. The absorption coefficient of MetHb is converted from its molar extinction coefficient [33] available over a spectral range of 450-680nm with a spectral resolution of 5nm. The MetHb absorption coefficient was interpolated to a resolution of 1nm within 450-680nm, and extrapolated as a flat value beyond 680nm to the upper range of the SfRS model analysis. The water absorption spectrum extracted from VirtualPhotonics varies over the entire SfRS spectrum. The lipid absorption spectrum extracted from VirtualPhotonics varies over the spectral range above 640nm and remains flat at wavelengths shorter than 640nm. The spectral profiles of the five chromophores are collectively displayed in Figure 2.3(A). The $v_{Water\&Lipid}$ in Eq. (II.7) is set at 93% [34]. In the implementation of Eqs (II.6) and (II.7) to Eq. (II.5), the spectral dependence of the reduced scattering coefficient of the soft bladder tissue was assumed to follow the widely-adopted formula of $\mu_s' = A\lambda^{-b}$, where A is the scattering amplitude and b is the scattering power. When all terms are fully expanded, Eq. (II.4) is expressed with seven variables to be determined, including $[Hb]_{total}$, f_{OxyHb}, f_{lipid} , f_{MetHb}, A, b, and P0. The number P0 is an effective intensity value that appears after the full expansion of the model. It has been found that the system had a low composite sensitivity at a spectral range below 500nm, and artifacts of undetermined sources occurred at above 850nm during the spectral fitting process. The spectral analysis was thus performed over the range of 500-850nm for the outcomes to be consistent. The spectra profiles shown in Figure 3 are thus displayed over the 500-850nm range only. The absorption spectra of OxyHb (1 μM), DeoxyHb (1 μM), MetHb (1 μM), lipid (50%) and water (10%). The concentrations are chosen for the peak values to be at similar levels at the linear scale of the ordinate. (B). The chromophore concentrations may be more accurately estimated by fitting the data sequentially within the three non-overlapping segments that have different sensitivity to the chromophore(s) considered. The spectrum segment 1 (500nm-600nm) is sensitive to [OxyHb] and [DeoxyHb]. The spectrum segment 2 (600nm-675nm) reveals [MetHb] according to the spectral dip around 635nm. The contributions of lipid and water is expected to dominate over the spectral segment 3 (675nm-850nm).

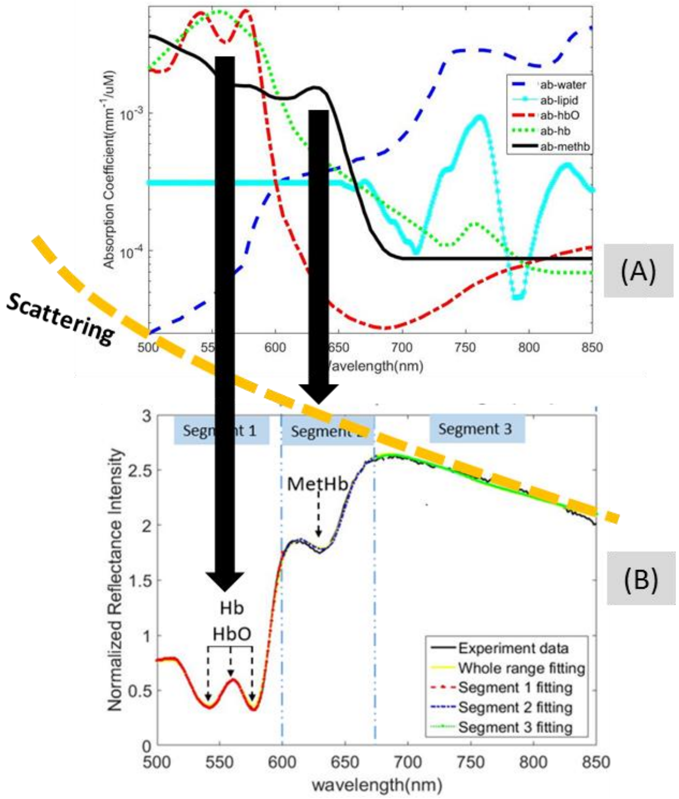

Figure II-3 (A) Absorption spectrum of oxygen-hemoglobin, dioxygen-hemoglobin, methemoglobin, lipid and water. (B) Three wavelength segments for sequential data-fitting

2.2.4 Method of estimating the chromophore compositions using a multi-segment fitting approach

The SfRS measurement was fitted according to the model composition described in the previous section for estimating the chromophore concentrations and scattering parameters. The model-data fitting of each individual SfRS profile was implemented in a sequential order, over the entire spectral profile and non-overlapping segments of the spectral profile as referred to Figure 2.3(B), according to the following sequences of minimizing the objective function between the fitted SfRS profile $\mathrm{R}_{fitted}(\lambda)$ and the measured SfRS profile $\mathrm{R}_{norm}(\lambda)$ as defined by:

$$\chi = \sum_{\lambda=\lambda_{lower}}^{\lambda_{upper}} \left|R_{fitted}(\lambda) - R_{norm}(\lambda)\right|^2 \tag{II-8}$$

Step 1: The seven variables are assigned an initial set of values including $[\mathrm{Hb}]_{\mathrm{Total}}$=200μM, f_{OxyHb}=50%, f_{MetHb}=1%, f_{Lipid}=10%, A=1, b=1, and P_0=1. With this initial guess-set, the seven variables were updated simultaneously by minimizing the objective function of the model-data fit over the entire spectral range that combined the three segments, i.e., $\lambda_{lower} = 500nm$, and $\lambda_{upper} = 850nm$ in Eq. (II.8).

Step 2: The seven parameters as the output of the step 1 were implemented as the modified guess-set. The seven variables were then updated simultaneously by minimizing the objective function of the model-data fit over only the spectral segment 2, i.e. $\lambda_{lower} = 600nm$, and $\lambda_{upper} = 675nm$ in Eq. (II.9). This step resulted in stronger weight on [MetHb] when all parameters are updated.

Step 3: Using the seven parameters estimated from the step 2 as the modified guess-set, the seven variables were updated simultaneously by minimizing the objective function of the model-data fit over only the spectral segment 1, i.e. $\lambda_{lower} = 500nm$, and $\lambda_{upper} = 600nm$ in Eq. (II.9). This step resulted in stronger associated weights on [OxyHb] and [DeoxyHb] when all parameters are updated.

Step4: Using the seven parameters estimated from the step 3 as the modified guess-set, the seven variables were updated simultaneously by minimizing the objective function of the model-data fit over only the spectral segment 3, i.e. $\lambda_{lower} = 675nm$, and $\lambda_{upper} = 850nm$ in Eq. (II.9). This step modifies primarily the parameters associated with scattering, and slightly updates the water and lipid contributions to the spectral absorption.

The sequence of steps 1-4 were executed one-round for each SfRS profile obtained from the rat bladder tissue. The potential of enhancing the estimation accuracy by sequentially fitting over the three non-overlapping spectral segments is to take advantage of the characteristic hemoglobin spectral feature at around 550nm, and a MetHb absorption signature at around 635nm. As shown in Figure 3(B), the spectral segment 1 (500-600nm) is significantly sensitive to [DeoxyHb] and [OxyHb]. The spectrum segment 2 (600-675nm) is notably sensitive to MetHb which is the most likely one among the five chromophores that could produce the characteristic dip at the neighborhood of 635nm. The spectral segment 3 (675-850nm) is a region wherein weak and relatively uniform spectral absorption is observed for all five chromophores of consideration, so over this spectral segment the scattering parameters could be recovered with less interplay by the absorption of the chromophore components.

2.3 Results

2.3.1 SfRS measurements grouped according to experimental conditions and the level of MetHb-indicating pattern

The total 107 SfRS measurements after normalization can be separated to 4 groups, according to the level of the spectral pattern at around 635nm that uniquely indicates the MetHb content. The representative SfRS profiles of these four groups are given in Figure 4. The MetHb (III) group at the right-most contains 2 SfRS profiles measured from two different positions of one grossly tumorous lesion of the bladder tissues of one rat in the AY-27 instilled group. There is a remarkable absorption feature near 635nm that matches MetHb absorption signature. The MetHb (II) group contains 6 SfRS profiles measured from other grossly tumorous lesions of the bladder tissues of two rats in the AY-27 instilled group, including one site close to that from which the profile of the MetHb (III) group was generated. The common features of these 6 SfRS profiles is a weak, but nonetheless, distinguishable, absorption feature near 635nm that reveals MetHb absorption. The

MetHb (I) group contains 72 SfRS profiles measured from other grossly tumorous lesions of the bladder tissues of four rats in the AY-27 instilled group, including the sites close to the two lesions generating the profiles of the MetHb (II) and (III) groups. Of these 72 SfRS profiles, there is lack of an absorption feature near 635nm unambiguously indicating MetHb absorption. The normal-group contains the entire 27 SfRS profiles acquired from the bladder tissues of the two control rats. None of these 27 SfRS profiles has shown any remarkable MetHb spectral feature near 635nm. However, when comparing the spectral pattern at sub-600nm range, the SfRS profile representing the 27 measurements from the normal rat tissues revealed weaker OxyHb/DeoxyHb absorption feature than the one representing 72 measurements of the MetHb-I group. Interestingly, the SfRS profile representing the 6 measurements of the MetHb-II group has stronger OxyHb/DeoxyHb absorption feature than the one representing the 72 measurements of the MetHb-I group, and the SfRS profile representing the 2 measurements of the MetHb-III group has the strongest OxyHb/DeoxyHb absorption feature among the profiles displayed. The distribution of the sites whereupon the 107 SfRS measurements were taken is summarized in Table 1, according to tissue-treatment condition and the significance of [MetHb] absorption feature in referring to Figure II-4. The normal group received no AY-27 treatment. The tumors groups are further separated to three sub-groups, according to the remarkableness of the MetHb spectra feature near 635nm. The bladders of the three tumor groups received AY-27 treatment.

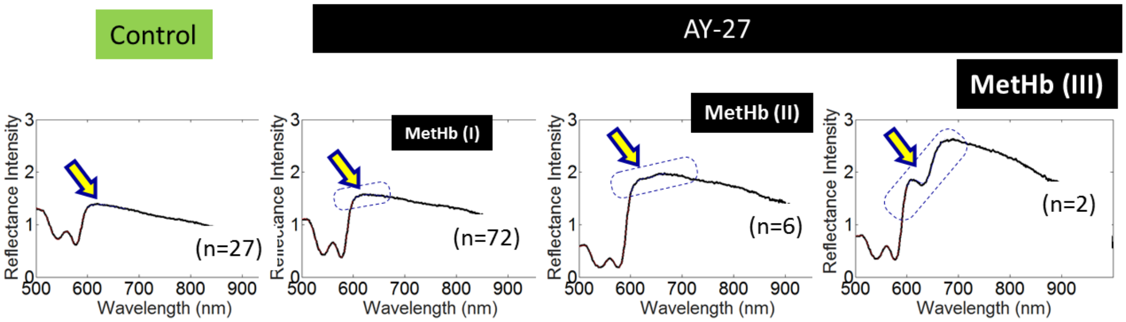

Figure II-4 The total 107 SfRS profiles are separated to normal group and three tumor groups

Table II-1 The distribution of the 107 measurements according to tissue-treatment condition and the significance of [MetHb] absorption feature in referring to Figure II-4

Group		Number of measurements	Animal ID
Control		27	Rat #1, #2
AY-27 instilled	Subgroup I	72	Rat #3, #4, #5, #6
	Subgroup II	6	Rat #4, #5
	Subgroup III	2	Rat # 5

2.3.2 Estimation of the MetHb proportion, total hemoglobin content, and the lipid fraction

The model-data fitting resulted in seven parameters to be estimated for each SfRS profile. These estimated parameters were grouped according to the 4 sub-sets of measurements, one set for the control bladders and three sets for the bladders treated with AY-27 celllines, as shown in Figure 4 that indicated different levels of MetHb spectral marker. Among the parameters resolved from the spectral analysis, three showed patterns of potential association with each other and with the tissue conditions expected for the specific group. These three parameters are total hemoglobin concentration, the proportion of MetHb in the total hemoglobin, and the lipid fraction in the water/lipid body. The estimated values of the total hemoglobin concentration, the proportion of MetHb in the total hemoglobin, and the lipid fraction in the water/lipid body are charted in Figure 5. The 2 SfRS measurements in the subset 3 of AY-27 instilled group had a MetHb proportion of (32.8±10.1) %. The 6 SfRS measurements in the subset 2 of AY-27 instilled group had a MetHb proportion of (7.3±3.6) %. The 72 SfRS measurements in the subset 1 of AY-27 instilled group had a MetHb proportion of (6.9±6.6) %. The 27 SfRS measurements in the control group had a MetHb proportion of (5.3±6.9) %. When grouped according to the MetHb proportion within the total hemoglobin, the total hemoglobin centration estimated for the 27 SfRS measurements in the control group was 285.1±214.6 µM. The total hemoglobin centration estimated for the 72 SfRS measurements in the subset 1 of AY-27 instilled group was 367.7±263.5 µM, for the 6 SfRS measurements in the subset 2 of AY-27 instilled group was 487.7±238.9 µM, and for the 2 SfRS measurements in the subset 3 of AY-27 instilled group was 541.6±364.9 µM. When grouped according to [MetH] proportion within the total hemoglobin, the fraction of lipid within the water-lipid body decreased from (2.6±2.8) % of the control group to (0.14±0.7) % of the subset 1 of AY-27 instilled group, and to negligible amount for both subset 2 and subset 3 of AY-27 instilled group.

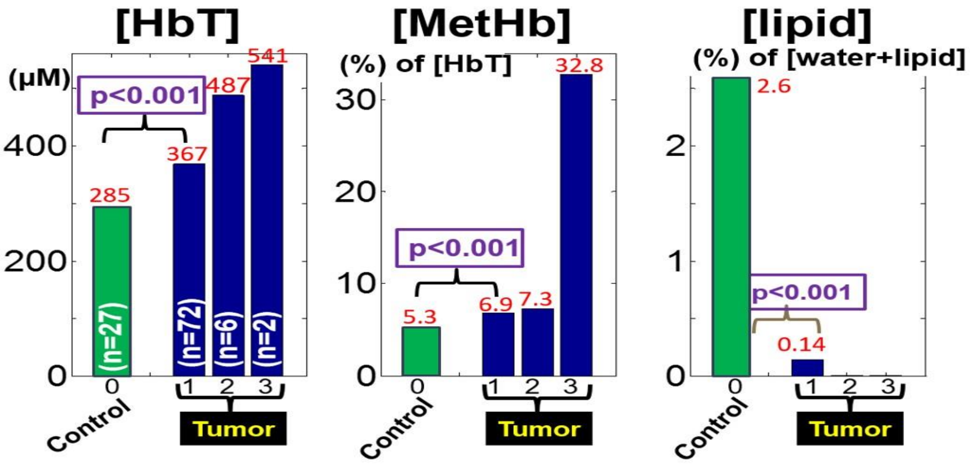

Figure II-5 The total hemoglobin content (uM), the MetHb proportion within the total hemoglobin content, and the lipid fraction within the water-lipid body.

2.4 Discussions

The 2 SfRS measurements sub-grouped as MetHb (III) carried a distinctive signature of MetHb absorption. The proportion of MetHb within hemoglobin content estimated for these two sites were significantly greater (more than 4-folds) than all other sites. The 2 sites with the highest MetHb proportion also presented the highest total hemoglobin concentration, approximately doubling that of the control site. For the MetHb (I) and MetHb (II) sub-groups, although the proportion of MetHb within the total hemoglobin were not significantly greater than that for the control group, the moderate increase of MetHb proportion was shown to associate with much stronger increase of the total hemoglobin concentration. The increased total hemoglobin and the elevation of MetHb proportion could be associated with angiogenesis and degradation in hemoglobin oxygen-transport. On the other hand, when evaluated according to the ascending order of MetHb proportion within the total hemoglobin, the fraction of lipid within the water-lipid body decreased from 2.6% of the control sits to 0.14% at the MetHb (I) sites, and negligible-to-nondetectable amounts at the MetHb (II) and MetHb (III) sites. The significant reduction of the lipid volume content in the tumor groups comparing to that in the control group, and the near-complete loss of the lipid content in the tumor sites revealing more MetHb proportion could indicate disruption of sub-epithelium tissue architecture due to neoplastic changes.

The total hemoglobin concentration, MetHb proportion within the total hemoglobin, and the lipid fraction in the water-lipid body are among the seven parameters estimated from the SfRS profiles. Other parameter including oxygen saturation and scattering power did not show a uniform ascending or descending order as the total hemoglobin, MetHb proportion, or lipid fraction are. The oxygenation saturation estimated for all 107 sites ranged from 87% to 96%. The high tissue oxygenation of the rat bladder wall measured in vivo by SfRS was in agreement with the oxygenation level of the serosal surface of human bladder wall measured in vivo by other spectroscopy methods [35].

One limitation of this study was the limited spectral range, specifically the longer wavelength bound of 850nm, with which the tissue parameters were estimated. The spectral analysis was conducted with the postulation of a fixed water-lipid body of 93% as was suggested by the previous reports [33]. However, the spectral profiles when extending beyond 850nm revealed potential changes of the water-lipid fraction in association with the different levels of MetHb spectral markers. Work is on-going to analyze the limited spectral information beyond 850nm to potentially improve the estimation of lipid and water contents. The improvement of lipid and water content estimations using the spectral information above 850nm, however, may have little effect on the estimations of the total hemoglobin and MetHb proportion as these hemoglobin compounds absorb weakly over the specific spectral range of 800nm and above when comparing to water and lipid, so the spectral analysis over that region would be less sensitive to the contents of OxyHb, DeoxyHb and MetHb.

2.5 Summary

In vivo single-fiber reflectance spectroscopy (SfRS) was performed on an orthotopic AY-27 rat bladder urothelial cell carcinoma model to explore potential spectroscopic features revealing neoplastic changes induced by intravesical instillation of AY-27 bladder tumor cells. A total of 107 SfRS measurements were taken from 27 sites on two control bladders and 80 from four AY-27 treated bladders. The spectral profiles obtained from AY-27 treated bladders revealed various levels of a methemoglobin (MetHb) characteristic spectral feature around 635nm. A multi-segment spectral analysis method estimated concentrations of five chromophore compositions including oxyhemoglobin, deoxyhemoglobin, MetHb, lipid and water. The 80 measurements from the AY-27 treated bladders could separate to three sub-sets according to the MetHb proportion. Specifically, 72 were in subset 1 with low proportion (5.3%<[MetHb]<7%), 6 in subset 2 with moderate proportion (7%<[MetHb]<30%), and 2 in subset 3 with significant proportion (>30%). When grouped according to [MetHB], the [HbT] increased from 368 μMol of subset 1 to 488 μMol of subset 2 to541 μMol of subset 3, in comparison to the 285 μMol of the control. The increased total hemoglobin and the elevation of MetHb proportion may signify angiogenesis and degradation in hemoglobin oxygen-transport. Additionally, the lipid volume content decreased from 2.58% in the control to <0.2% in the tumor groups, indicating disruption of sub-epithelium tissue architecture.

CHAPTER III

SIMPLE ANALYTICAL TOTAL DIFFUSE REFLECTANCE OVER A REDUCED-SCATTERING-PATHLENGTH SCALED DIMENSION OF [10^{-5}, 10^{-1}] FROM A MEDIUM OF HG SCATTERING ANISOTROPY

3.1 Introduction

Diffuse reflectance is useful to surface assessment of turbid medium in biomedicine [56], pharmaceutical packaging [57], agriculture [58], as well as remote sensing [59]. In applications for biomedical domains involving interstitial deployment or instrument channel of an endoscope, and for remote sensing, diffuse reflectance is assessed with a very small size or angular profile, like that of a $200\mu m$ single-fiber probe [60]. Whether it is for diagnosing cancer [61] or for monitoring physiological functions [62], diffuse reflectance probing near the point-of-incidence practically requires a forward model of the light collected over the entire circular area containing the point-of-incidence [63].

The exact analytical solution of radial diffuse light reflectance from a biological tissue does not exist [64], nor does the total diffuse reflectance over a small probing area. As a result, Monte Carlo (MC) simulation is the de facto tool for computing the radial as well as the total diffuse reflectance over sub-diffusion scale [65]. However, the statistical demand on random events and the lack of physical insights [66] make MC method under-suited for rapid forward computation. Accurate analytical total diffuse reflectance at sub-diffusion scale would involve radiative transfer (RT) that must also entertain the phase-function complexity [67]. Alternatively, approximate analytical total diffuse reflectance over an area containing the point-of-incidence is sought for a specific phase function. Steady-state probing at a single-fiber scale has benefited from a semi-empirical model [18, 19, 68, 69] of the total diffuse reflectance. That model considers the delivery area to overlap with the collection area with a limited angular aperture. Developed by fitting to MC measurements at various values of the scattering anisotropy factor g specific to the Heyney-Greenstain (HG) phase function, that model expressed the total diffuse reflectance as the product of a scattering component determined by the reduced scattering only, an attenuation component accounting for the attenuation due to absorption over an effective total pathlength, and a collection aperture component. Up to 6 parameters were fitted for each value of g. Being the primary analytical model of the total diffuse reflectance at the single-fiber scale for clinical applications [70-73], there were however indications that the model could give rise to physiologically impractical parameters [60]. Besides calibration [74], more understanding of the analytical aspect of the total diffuse reflectance over an area centered on the point-of-incidence that is amendable to single-fiber-scale modeling is imperative.

The total diffuse reflectance over an area is the integration of the radial diffuse reflectance over the area of collection. When a collection angle is pertinent, the total diffuse reflectance is the full-angle diffuse reflectance scaled by the collection aperture [68, 75]. Analytical total diffuse reflectance can thus be derived, if the analytical radial diffuse reflectance is available. However, it remains challenging to model the radial diffuse reflectance from biological tissue at the single-fiber scale, i.e. close to the point-of-incidence [76]. Methods based on diffusion analytics implemented multiple distributed or isolated isotropic sources [77, 78] to enhance modeling of the steady-state radial diffuse reflectance at dimensions less than the transport scattering path-length. Radial diffuse reflectance at source-detector-separation (SDS) close to one transport mean free path was found predictable [79] with μ_a, μ_s', and the moments of the phase function. One approach modeled the g-specific radial diffuse reflectance over a SDS down to 10^{-1} of $1/\mu_s'$, or 100μm for $\mu_s' = 1mm^{-1}$, where μ_s' is the reduced scattering coefficient [80]. Radial diffuse reflectance for a SDS of 10^{-2} of $1/\mu_s'$ was derived via an alternative solution to RT [66] with the higher-order phase-function dependency to be solved by integration. Analytical radial diffuse reflectance at a SDS of 10^{-3} of $1/\mu_s'$ was given by small-angle-scattering approximation (SAA) to RT [81]. These approximations to radial diffuse reflectance at very short SDS encourage the analytical formation of the total diffuse reflectance via integration.

We demonstrate simple analytical total diffuse reflectance over a spatial scale much smaller than the reduced scattering pathlength. This is an integration-based approach performed over an area centered at the point-of-incidence that has a reduced scattering pathlength ($1/\mu_s'$) scaled diameter of [10^{-5}, 10^{-1}] from a turbid medium of a scattering anisotropy factor g that is specific to the HG phase function [82]. This approach is based upon an analytical radial diffuse reflectance over the similar range of SDS of $[10^{-5}, 10^{-1}]$, with the lower bound of the dimension being two orders of magnitude smaller than was previously modeled [81]. The radial diffuse reflectance from an infinite medium of isotropic scattering associated with a point-beam injection is derived with RT, which is used as the basis for approximating the radial diffuse reflectance from a semi-infinite medium of $g \approx 0$ by way of P1 approximation and considering the boundary effects. Integration of it then produces the analytical total diffuse reflectance for $g \approx 0$. The radial diffuse reflectance from a medium with g≥0.5 is then formulated semi-empirically by referring to MC simulation results, while abiding to the constraint that the analytical radial diffuse reflectance for $g > 0$ must resort to the analytical radial diffuse reflectance for isotropic scattering as g⇒ 0. The integration of this radial diffuse reflectance for g≥0.5 then leads to the analytical total diffuse reflectance for g≥0.5 that must also resort to the one for isotropic scattering as g⇒ 0. The analytical radial and the integration-rendered analytical total diffuse reflectance for turbid medium with HG scattering anisotropy are evaluated over a $1/\mu_s'$ scaled dimension of $[10^{-5}\ 10^{0}]$, for g over [0.5, 0.95], and an absorption coefficient ranging 3 orders of magnitude up to the magnitude of μ_s'.

3.2 Analytical Methods

3.2.1 The geometry of concern

The analysis is limited to the full-angle total diffuse reflectance over an area with a diameter $<1/\mu_s'$ (e.g. <1mm for $\mu_s' = 1mm^{-1}$), from a semi-infinite homogeneous medium as depicted in Fig. 1. A steady-state unitary-power source is injected into the medium at the center of the area of collection, which is also the origin of the polar coordinate. A point on the tissue-air interface at a radial distance of ρ from the point-of-incidence is represented by (ρ, 0, φ). A unit vector $\hat{z}$ marks the initial direction of the light injected into the medium. The diameter of the area is denoted as d_{area}, so $\rho = (0, d_{area}/2]$.

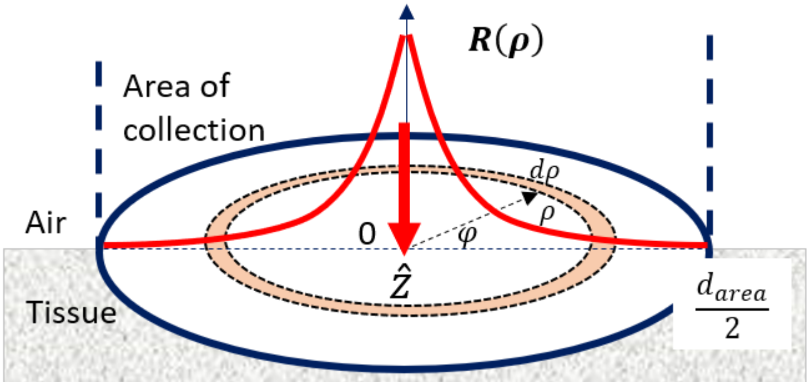

Figure III-1 Full-angle collection of diffuse reflectance within a circular area.

3.2.2. Steady-state radial and total diffuse reflectance from a semi-infinite medium of g≈0

We first consider an infinite homogeneous medium of isotropic scattering. The scattering phase function is $P(\hat{s}', \hat{s}) = P(\hat{s}' \cdot \hat{s})$, where $\hat{s}$ and $\hat{s}'$ are respectively the outgoing and incoming directions of a scattering event. The steady-state RT equation associated with this medium is:

$$\hat{s}\cdot\nabla L(\rho,z,\emptyset,\hat{s},\mu_a,\mu_s) = -\mu_t L(\rho,z,\emptyset,\hat{s},\mu_a,\mu_s) + \mu_s \iiint_{4\pi} L(\rho,z,\emptyset,\hat{s}',\mu_a,\mu_s)P(\hat{s}'\cdot\hat{s})d\Omega' + S(\rho,z,\emptyset,\hat{s}) \qquad \text{(III-1)}$$

where $L(\rho,z,\emptyset,\hat{s},\mu_a,\mu_s)$ is the radiance at position $(\rho,z,\emptyset)$ traversing along the direction $\hat{s}$, $\mu_t = \mu_a + \mu_s$ is the attenuation coefficient, and $S(\rho,z,\emptyset,\hat{s})$ is the distribution of the source along the direction $\hat{s}$. A narrow unitary-power source injected at the origin and along the $\hat{z}$ direction is represented by [10]:

$$S(\rho,z,\emptyset,\hat{s}) = \frac{1}{2\pi}\delta(\rho)\delta(z)\delta(1-\hat{s}\cdot\hat{z}) \qquad \text{(III-2)}$$

where the 2π factor is related to $\emptyset$. The radiance of Eq. (III.1) associated with isotropic scattering resulting from a collimated light injection can be decomposed to a collimated component and an isotropically diffusing component [66] as

$$L(\rho,z,\emptyset,\hat{s},\mu_a,\mu_s) = L_{coll}(\rho,z,\emptyset,\hat{s},\mu_a,\mu_s) + L_{iso}(\rho,z,\emptyset,\hat{s},\mu_a,\mu_s) \qquad \text{(III-3)}$$

The RT equation then becomes

$$\hat{s}\cdot\nabla L_{coll}(\rho,z,\emptyset,\hat{s},\mu_a,\mu_s) + \hat{s}\cdot\nabla L_{iso}(\rho,z,\emptyset,\hat{s},\mu_a,\mu_s) = -\mu_t L_{coll}(\rho,z,\emptyset,\hat{s},\mu_a,\mu_s) - \mu_t L_{iso}(\rho,z,\emptyset,\hat{s},\mu_a,\mu_s) + \mu_s \iiint_{4\pi} L_{coll}(\rho,z,\emptyset,\hat{s}',\mu_a,\mu_s)P(\hat{s}'\cdot\hat{s})d\Omega' + \mu_s \iiint_{4\pi} L_{iso}(\rho,z,\emptyset,\hat{s}',\mu_a,\mu_s,g)P(\hat{s}'\cdot\hat{s})d\Omega' + \frac{1}{2\pi}\delta(\rho)\delta(z)\delta(1-\hat{s}\cdot\hat{z}) \qquad \text{(III-4)}$$

By referring to the decomposition treatment demonstrated in [66], we seek a solution to a portion of Eq. (III.4) as the following,

$$\hat{s}\cdot\nabla L_{coll}(\rho,z,\emptyset,\hat{s},\mu_a,\mu_s) = -\mu_t L_{coll}(\rho,z,\emptyset,\hat{s},\mu_a,\mu_s) + \frac{1}{2\pi}\delta(\rho)\delta(z)\delta(1-\hat{s}\cdot\hat{z}) \qquad \text{(III-5)}$$

Integrating Eq. (III.5) over the entire spatial angle gives

$$\iiint_{4\pi} \hat{s}\cdot\nabla L_{coll}(\rho,z,\emptyset,\hat{s},\mu_a,\mu_s)d\Omega = -\mu_t \iiint_{4\pi} L_{coll}(\rho,z,\emptyset,\hat{s},\mu_a,\mu_s)\,d\Omega + \frac{1}{2\pi}\delta(\rho)\delta(z)\iiint_{4\pi}\delta(1-\hat{s}\cdot\hat{z})\,d\Omega \qquad \text{(III-6)}$$

and that leads to

$$\frac{\partial}{\partial z}L_{coll}(\rho,z,\emptyset,\hat{z},\mu_a,\mu_s)=-\mu_t L_{coll}(\rho,z,\emptyset,\hat{z},\mu_a,\mu_s)+\frac{1}{2\pi}\delta(\rho)\delta(z) \qquad \text{(III-7)}$$

It is noted with Eq. (III.1) that $L(\rho,z,\emptyset,\hat{s},\mu_a,\mu_s)$ must have the dimension of $S(\rho,z,\emptyset,\hat{s})/\mu_t$. The solution to Eq. (III.7) is then given, via Laplace transformation and satisfying the initial condition at $(z=0)$, as the following:

$$L_{coll}(\rho,z,\emptyset,\hat{z},\mu_a,\mu_s)=\frac{1}{2\pi\mu_t}\delta(\rho)\delta(z)+\frac{1}{2\pi\mu_t}\delta(\rho)[1-\delta(z)]exp(-\mu_t z) \qquad \text{(III-8)}$$

Evaluating Eq. (III.4) on $(z=0)$ by plugging Eqs. (III.6) and (III.8) gives

$$\hat{s}\cdot\nabla L_{iso}(\rho,0,\emptyset,\hat{s},\mu_a,\mu_s)=-\mu_t L_{iso}(\rho,0,\emptyset,\hat{s},\mu_a,\mu_s)$$

$$+\mu_s\iiint_{4\pi}L_{iso}(\rho,0,\emptyset,\hat{s}',\mu_a,\mu_s)P(\hat{s}'\cdot\hat{s})d\Omega'+\frac{1}{2\pi\mu_t}\mu_s\delta(\rho) \qquad \text{(III-9)}$$

Using the spherical harmonic expansion and considering that there is only the 0-th order term for isotropic scattering, we have the fluence rate solution of Eq (III.9) at $(z=0)$ as the following:

$$\Phi_{iso}(\rho,0,\mu_a,\mu_s)=\frac{1}{8\pi^2 D\mu_t}\frac{\mu_s}{\rho}exp(-\mu_{eff}\rho)=\frac{1}{4\pi}\frac{3}{2\pi}\frac{(\mu_s)^2}{\mu_s\rho}exp(-\mu_{eff}\rho) \qquad \text{(III-10)}$$

Where $\mu_{eff}=\sqrt{\mu_a/D}$ is the effective attenuation coefficient and $D=(3\mu_t)^{-1}$ is the diffusion coefficient with $\mu_t=\mu_a+\mu_s$. We then consider a medium with a negligible anisotropy i.e., $g\approx 0$. Repeating the spherical harmonic expansion will now lead to the 0-th order term of photon fluence rate on the plane of $(z=0)$ to be identical to Eq. (III.10), and the 1-st order term by the slightly anisotropic scattering forming a flux term that is much smaller than the 0-th order term. The total photon counts are then:

$$R(\rho,0,\mu_a,\mu_s,g\approx 0)=\Phi_{iso}(\rho,0,\mu_a,\mu_s')-3\mathrm{D}\cdot\nabla\Phi_{iso}(\rho,0,\mu_a,\mu_s')$$

$$=\frac{1}{4\pi}\frac{\zeta}{\pi}\frac{(\mu_s)^2}{\mu_s\rho}exp(-\mu_{eff}\rho) \qquad \text{(III-11)}$$

Where ζ is the result of scaling the smaller flux term with respect to the fluence rate term. When the plane $(z = 0)$ is the air-medium interface, the extrapolated zero-boundary condition is implemented with an image source [83]. The image of the source defined by Eq. (III.2) becomes $-\frac{1}{2\pi}\delta(\rho)\delta(z+2z_b)\delta(1+\hat{s}\cdot\hat{z})$, which corresponds to a source of negative unitary-power collimated along $-\hat{z}$ and at $2z_b$ away from the plane $(z = 0)$, where $2z_b = 4\,\mathrm{AD}$, $\mathrm{A} = (1+\xi)/(1-\xi)$, and $\xi = -1.44{n_{tiss}}^{-2} + 0.710{n_{tiss}}^{-1} + 0.668 + 0.0636n_{tiss}$ for the tissue-air boundary [84]. The resulted diffuse reflectance on the tissue-air interface at the now half-plane $(z = 0)$ is

$$R(\rho, 0, \mu_a, \mu_s, g \approx 0) = \frac{1}{4\pi}\frac{\zeta}{\pi}\frac{(\mu_s)^2}{\mu_s\rho}exp\left(-\mu_{eff}\rho\right) - \frac{1}{4\pi}\frac{\zeta'}{\pi}\frac{(\mu_s)^2}{\mu_s\sqrt{\rho^2+(2z_b)^2}}exp\left(-\mu_{eff}\sqrt{\rho^2+(2z_b)^2}\right) \tag{III-12}$$

The second term in Eq. (III.12) is evaluated (see Appendix 1) to be <1.8% of the first term over $(\mu_s'\rho)$=[10^{-5}, 10^{-1}], the region of interest of this work, so is dropped. The ζ in Eq. (III.12) is set to be 2 by comparing with MC simulation to result in a simple form of:

$$R(\rho, 0, \mu_a, \mu_s, g \approx 0) = \frac{1}{2\pi^2}\frac{(\mu_s)^2}{\mu_s\rho}exp\left(-\mu_{eff}\rho\right) \tag{III-13}$$

Integrating Eq. (III.13) over the area of collection leads to the analytical total diffuse reflectance as

$$\begin{aligned} \mathrm{I}(\rho, 0, \mu_a, \mu_s, g \approx 0) &= \int_0^{2\pi}\int_0^{\rho} \mathrm{R}(\rho, \mu_a, \mu_s')\cdot\rho\cdot d\rho\, d\varphi \\ &= \frac{1}{\pi}\cdot\left(\frac{\mu_s}{\mu_{eff}}\right)\cdot\left[1 - exp\left(-\mu_{eff}\rho\right)\right] \end{aligned} \tag{III-14}$$

3.2.3. Steady-state radial and total diffuse reflectance from a semi-infinite medium with an anisotropy factor g

We then consider a homogeneous turbid medium with a scattering anisotropy factor g that gives $\mu_s' = \mu_s(1-g)$. The radial diffuse reflectance for $g > 0$ must analytically become that corresponds to isotropic scattering as $g \Rightarrow 0$. By abiding to this physical constraint and fitting to MC simulation results to be detailed in the subsequent sections, we approximate the radial diffuse reflectance from a semi-infinite medium of an anisotropy factor g as:

$$R(\rho, 0, \mu_a, \mu_s, g) = \frac{1}{2\pi^2} \cdot \exp\left(-1.5\left(\sqrt{g}\right)^{\gamma_1}\right) \cdot \frac{{\mu_s}^{(2-g)}[\mu_s(1-g)]^g}{(\mu_s\rho)^{(1+\epsilon)}} \exp(-\mu_{eff}\rho) \tag{III-15}$$

Which contains the following newly appearing parameters:

$$\gamma_1 = 4\mu_a \frac{1}{\mu_t} \tag{III-16}$$

$$\epsilon = 0.2\{1 - [1 - (\gamma_2)^g]^g\} \tag{III-17}$$

$$\gamma_2 = 0.1\mu_a \frac{1}{\mu_t} \tag{III-18}$$

The “γ" of Eq. (III.16) or (III.18) that vanishes at no absorption acts as the scaled probability of absorption over the transport pathlength. The “ϵ” is a g-dependent factor that vanishes as the scattering anisotropy disappears. Eq. (III.15) apparently becomes Eq. (III.13) at g=0. Integrating Eq. (III.15) over the area of collection as with Eq. (III.14) leads to the total diffuse reflectance. The result contains an Error function and approximates to:

$$I(\rho, 0, \mu_a, \mu_s, g) = \frac{1}{\pi} \cdot \exp\left(-1.5\left(\sqrt{g}\right)^{\gamma_1}\right) \cdot \frac{(1-g)^g}{1-\epsilon} \cdot (\mu_s\rho)^{1-\epsilon} \cdot [1 - \exp(-\mu_{eff}\rho)] \cdot \frac{1}{(\mu_{eff}\rho)^{1+\epsilon}} \tag{III-19}$$

It is straightforward to see Eq. (3.19) reaching Eq.(3.14) at g $\Rightarrow 0$.

3.3 Numerical assessments

The MC simulations were performed using the Monte Carlo Command Line (MCCL, v4.7.0Beta) application of Virtual Photonics [80, 85] implemented on a 24-core Linux server operated by the High Performance Computing Center at Oklahoma State University. This MC solver outputs the radial diffuse reflectance from an air-bounding turbid medium of only the HG phase function by specifying the g. All photons arriving at a surface evaluation point were counted. The MC results are the discrete values of the radial diffuse reflectance, as illustrated in Figure III-2, for examining the analytical radial diffuse reflectance computed with Eq. (III.13) or (III.15). The MC radial diffuse reflectance was then numerically assembled to produce the total diffuse reflectance against which the analytical total diffuse reflectance of Eq. (III.14) or (III.19) was compared.

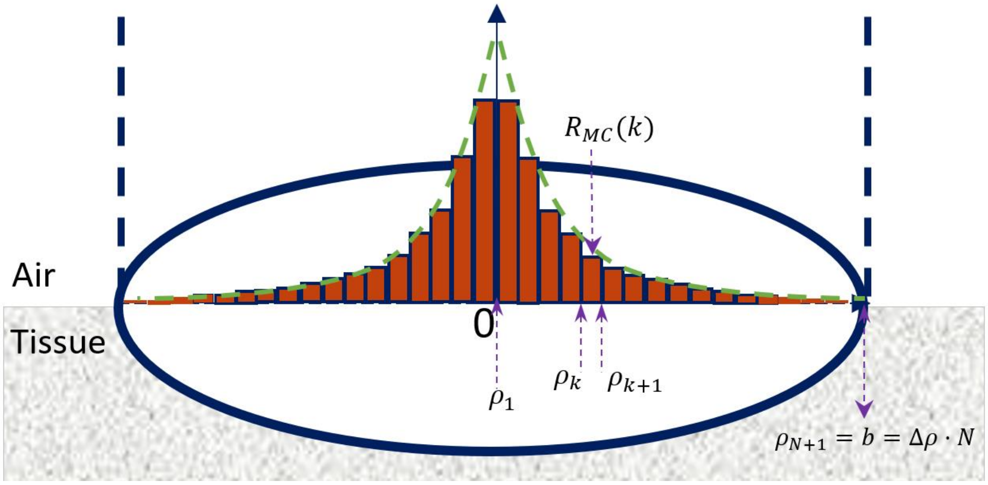

Figure III-2 MC simulated spatially resolved diffuse reflectance

A user-editable Input File was modified to customize the thickness of the medium, medium optical properties, and the positions of evenly spaced evaluation points on the medium surface. The tissue thickness was set to 1000m or 1 kilometer to ensure the semi-infinite condition at a scattering property as weak as $\mu_s' = 0.001 mm^{-1}$ or $1/\mu_s'$=1m. The tissue refractive index was fixed at 1.40, giving an A value of 3.2507 for Eq. (3.12). Other tissue optical properties for user definition included the set of (μ_a, μ_s, g) or equivalently(μ_a, μ_s', g). The radial diffuse reflectance was evaluated over the reduced scattering scaled SDS of $(\mu_s'\rho)$=[10^{-5}, 100] for assessing the analytical forms. The interval of the points was $10^{-5}(1/\mu_s')$, corresponding to total 100,000 points on the tissue surface. A total 10,000,000 photons were launched for each set of tissue parameters. Approximately 5 hours of computational time were needed to obtain a data set corresponding to each subfigure of (A)-(D) of the results shown in Figure III-4 of the next section.

As shown in Figure III-2, the interval between the neighboring points is $\Delta\rho$, the total number of steps is N, so the radius of the discrete area of collection is $b = N \cdot \Delta\rho$. The order of the radial position counted from the one next to the point-of-incidence is k=[1, N]. The k-th discrete strip has an inner radius of $\rho_k = k \cdot \Delta\rho$. The MC radial diffuse reflectance is denoted as $R_{MC}(k \cdot \Delta\rho, \mu_a, \mu_s', g)$. The MC total diffuse reflectance over the radius of $b = N \cdot \Delta\rho$ is denoted as $I_{MC}(b, \mathrm{\mu_a}, \mathrm{\mu_s'}, \mathrm{g})$, which is calculated by:

$$I_{MC}(b, \mathrm{\mu_a}, \mathrm{\mu_s'}, \mathrm{g}) = \sum_{\mathrm{k=0}}^{\mathrm{N-1}} \mathrm{R_{MC}}(\mathrm{k} \cdot \Delta\mathrm{\rho}, \mathrm{\mu_a}, \mathrm{\mu_s'}, \mathrm{g}) \cdot \left[\pi\rho_{k+1}^2 - \pi\rho_k^2\right]$$

$$= \sum_{\mathrm{k=0}}^{\mathrm{N-1}} \mathrm{R_{MC}}(\mathrm{k} \cdot \Delta\mathrm{\rho}, \mathrm{\mu_a}, \mathrm{\mu_s'}, \mathrm{g}) \cdot \pi(\Delta\mathrm{\rho})^2[2k+1] \qquad \text{(III-20)}$$

The tissue optical and dimensional properties used for the MC simulations were implemented in Eqs. (III.13) and (III.14) to calculate respectively the radial and total diffuse reflectance from a medium of isotropic scattering, and to Eqs. (III.15) and (III.19) for those corresponding to a medium with g=[0.5, 0.6. 0.7, 0.8, 0.9, 0.95]. The total diffuse reflectance versus $\mathrm{\mu_s'} d_{area}$ is also evaluated for two cases with the same $\mathrm{\mu_s'} d_{area}$. One is to have $\mathrm{\mu_s'} = 1mm^{-1}$ so d_{area} may change, and the other is to have $d_{area} = 1mm$ so $\mathrm{\mu_s'}$ may change. The aforementioned spatially resolution of 100,000points on the tissue surface corresponds to the former case. The latter case is assessed by setting $\mathrm{\mu_s'}$ as [1, 3, 5, 7, 9]× [10^{-5}, 10^{-4}, 10^{-3}, 10^{-2}, 10^{-1}]mm^{-1}. The implementation of Eqs. (III.13) & (III.14) (g=0) and Eq. (III.15) & (III.19) (g>0) for the latter case wherein $\mathrm{\mu_s'}$ is varied for $d_{area} = 1mm$ is done by converting the value of $\mathrm{\mu_s'}$ for $d_{area} = 1mm$ to a value of $d_{area}$for $\mathrm{\mu_s'}$=1mm^{-1} while keeping $\mathrm{\mu_s'} d_{area}$ unchanged.

3.4 Results

It is worth noting the spatial scale, with respect to $1/\mathrm{\mu_s'}$, over which the forgoing analytical radial and total diffuse reflectance are evaluated against the MC measurements. Figure 3.3 displays the MC radial and total diffuse reflectance over the $1/\mathrm{\mu_s'}$ scaled dimension of $[10^{-5}, 10^{3}]$ at three conditions of the scattering anisotropy: isotropic (g=0), moderately anisotropic (g=0.5), and highly forward scattering (g=0.95). The MC results over the abscissa range of 8 orders of magnitude over $[10^{-5}, 10^{3}]$ were obtained by concatenating one set corresponding to 4 orders of magnitude over $[10^{-5}, 10^{-1}]$ and another set corresponding to 4 orders of magnitude over $[10^{-1}, 10^{3}]$. The concatenation was necessary due to the difficulty of computing the entire data set over the full spatial scale of 8 orders of magnitude while maintaining the same radial resolution. The concatenation of the two date sets having two different radial resolutions and numerical precisions caused the discontinuity of the markers at the abscissa value of 10^{-1}, the boundary between the radial scales of the two data sets.

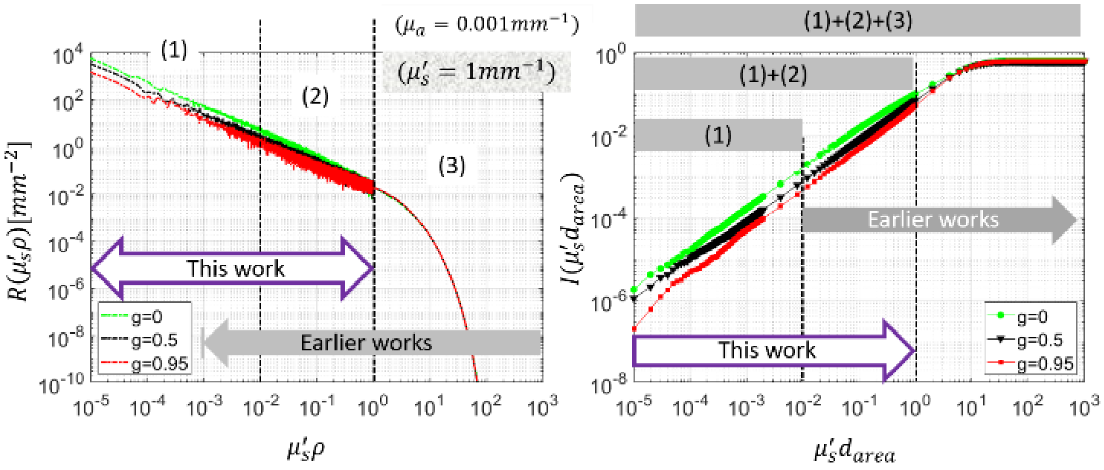

Figure III-3 Radially resolved diffuse reflectance (left-hand part) and total diffuse reflectance (right-hand part) evaluated in this work

Three $1/\mu_s'$ scaled spatial regions for the radial diffuse reflectance can be identified in (A). (1) The leftmost segment of $[10^{-5}, 10^{-2}]$, over which the three profiles corresponding to the g values of respectively 0, 0.5, and 0.95 run nearly parallel to each other, indicating the intensity dependency on g. (2) The middle segment of $[10^{-2}, 10^{0}]$, over which the three profiles corresponding to three g values including 0, 0.5, and 0.95 appear to merge as the spatial dimension increases, indicating the rate-of-change dependency on g. (3) The rightmost segment of $[10^{0}, 10^{2}]$, over which the insensitivity on g is unremarkable. By assembling the radial diffuse reflectance of (A) to produce the total diffuse reflectance as shown in (B), three regions can also be identified. The assembly of the radial diffuse reflectance of (A) up to the $1/\mu_s'$ scaled spatial dimension of 10^{-2} leads to the segment marked as (1) in (B). The assembly of the radial diffuse reflectance of (A) up to the $1/\mu_s'$ scaled spatial dimension of 10^0 leads to the segment marked as (1)+(2) in (B). The assembly of the radial diffuse reflectance of (A) up to the $1/\mu_s'$ scaled spatial dimension of 10^3 leads to the segment marked as (1)+(2)+(3) in (B). It is over $[10^{-5}, 10^0]$ that the forgoing analytical radial and total diffuse reflectance are evaluated while the model-working range is suggested as $[10^{-5}, 10^{-1}]$. The lower bound of this scale for assessing the radial diffuse reflectance is 2~3 orders of magnitude closer to the point-of-incidence than was previously approached [66, 81]. The lower bound of this scale for assessing the total diffuse reflectance is 3 orders of magnitude smaller than the scale previously analyzed [86].

The analytical radial and total diffuse reflectance in comparison to MC simulation results are presented according to the following orders. The results for radial diffuse reflectance precede those for the total diffuse reflectance. The results for g=0 precede those for g=[0.5, 0.9]. In assessing the radial or total diffuse reflectance, the case of isotropic scattering with differing μ_a is presented firstly, then the case of g=0.9 with differing μ_a, followed by the case of fixed μ_a with 4 values of g. In each case involving non-zero g, the MC profile corresponding to isotropic scattering (g=0) is added as the reference (marked as green). The radial diffuse reflectance is evaluated versus $(\mu_s'\rho)$ range of $[10^{-5}, 10^0]$, while the total diffuse reflectance is evaluated versus $(\mu_s' d_{area})$ over $[10^{-5}, 10^0]$.

The results in sub-sections 4.1 to 4.9 corresponding to $(\mu_s'\rho)$ or $(\mu_s' d_{area})$ of $[10^{-5}, 10^0]$ are presented with 5 sub-figures. (A) to (D) are the diffuse reflectance as a function of $(\mu_s'\rho)$ or $(\mu_s' d_{area})$ over 4 values of one tissue property as marked. (E) plots the errors of the analytical values of (A)-(D) with respect to the MC simulations. A straight line of slope 1 would indicate an exact match of the model predictions with the MC results. The percentage errors of the analytical values with respect to MC results are presented as (average ± standard deviation)% evaluated over the size scale specified for each case.

3.4.1 Absorption coefficient dependency of the radial diffuse reflectance in isotropic scattering medium

Figure III-4 assesses the radial diffuse reflectance $R(\mu_s\rho)$ over $(\mu_s\rho)$=[10^{-5}, 10^{0}] for a medium of isotropic scattering (g=0) with μ_s=1mm^{-1}, and μ_a=[0.001, 0.01, 0.1, 1.0]mm^{-1}. The range of μ_a corresponds to an absorption to scattering ratio of [0.001, 1]. Over $(\mu_s\rho)$=$[10^{-5}, 10^{-1}]$, the analytical radial diffuse reflectance $R(\mu_s\rho)$ agrees with MC result with an error of (29.1±8.8)%. The absorption dependence of $R(\mu_s\rho)$ over $(\mu_s\rho)$ of [10^{-5}, 10^{-1}] is unremarkable. The shaded area in (D) and (E) marks the value of $(\mu_s\rho) > 10^{-1}$. The effect of absorption on $R(\mu_s\rho)$ becomes increasingly noticeable over the shaded area as $\mu_s\rho$ increases.

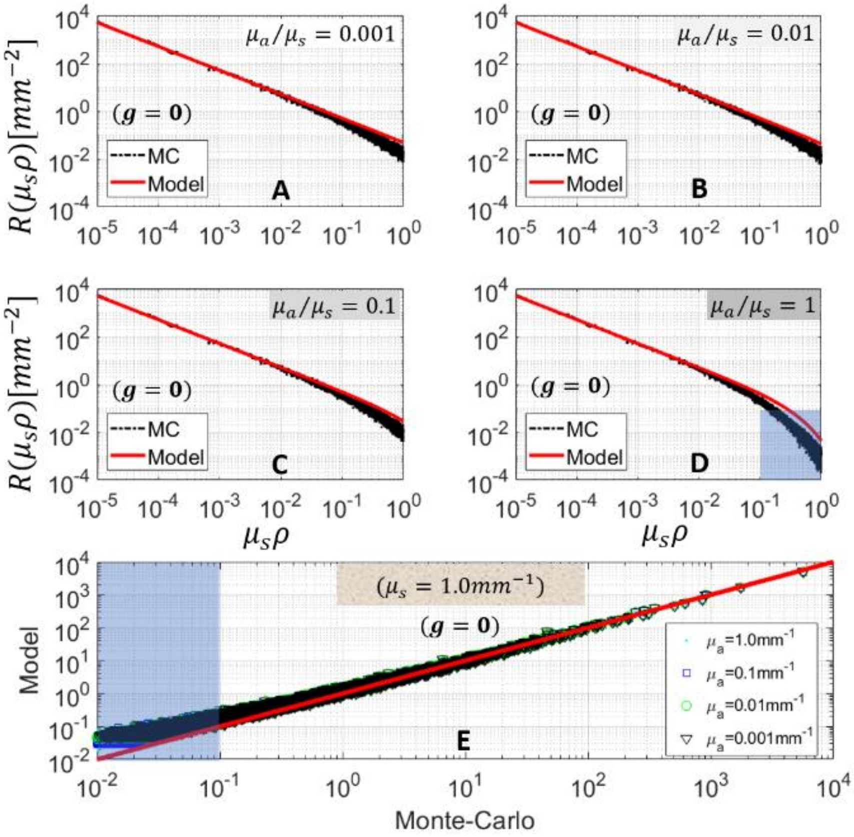

Figure III-4 Radial diffuse reflectance at μ_s= 1mm^{-1} and g=0 for four different absorption cases

3.4.2 Absorption coefficient dependency of the radial diffuse reflectance in anisotropy medium with g=0.9

Figure III-5 assesses the radial diffuse reflectance $\boldsymbol{R}(\boldsymbol{\mu}'_{\mathbf{s}}\boldsymbol{\rho})$ over ($\boldsymbol{\mu}'_{\mathbf{s}}\boldsymbol{\rho}$) of [$10^{-5}$, 10^{0}] for a medium of $\boldsymbol{\mu}'_{\mathbf{s}}$=1mm^{-1} with an anisotropy factor g=0.9, and $\boldsymbol{\mu_a}$=[0.001, 0.01, 0.1, 1.0]mm^{-1}. The $\boldsymbol{\mu_a}$ varying over 3 orders of magnitude corresponds to an absorption to reduced scattering ratio of [0.001, 1]. Over ($\boldsymbol{\mu}'_{\mathbf{s}}\boldsymbol{\rho}$)$=[\mathbf{10^{-5}}, \mathbf{10^{-1}}]$, the analytical radial diffuse reflectance $\boldsymbol{R}(\boldsymbol{\mu}'_{\mathbf{s}}\boldsymbol{\rho})$ agrees with MC result with an error of (5.0±9.2)%. The absorption dependence of $\boldsymbol{R}(\boldsymbol{\mu}'_{\mathbf{s}}\boldsymbol{\rho})$ appears unremarkable over ($\boldsymbol{\mu}'_{\mathbf{s}}\boldsymbol{\rho}$) of [$10^{-5}$, 10^{-1}]. When compared to the MC result at g=0 as the reference (green markers), the radial diffuse reflectance is smaller for g=0.9 at the same value of $\boldsymbol{\mu}'_{\mathbf{s}}\boldsymbol{\rho}$. The difference of the radial diffuse reflectance between g=0.9 and g=0 diminishes as $\boldsymbol{\mu}'_{\mathbf{s}}\boldsymbol{\rho}$ reaches 10^{0}, or equivalently at SDS equaling the reduced scattering pathlength.

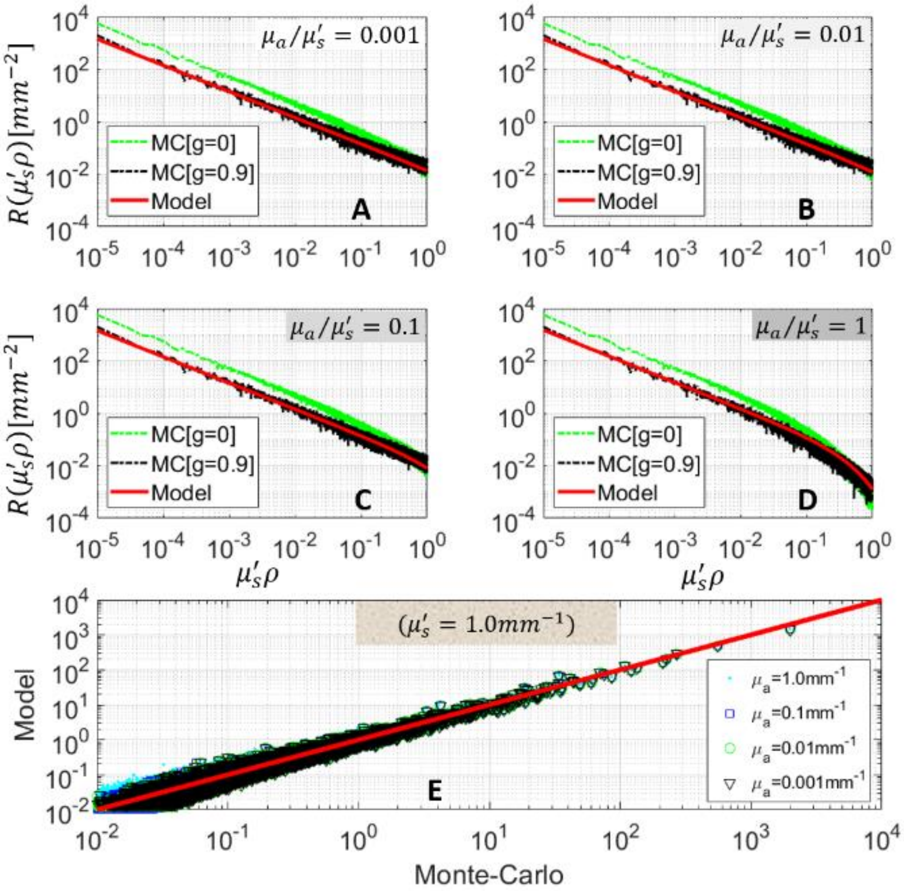

Figure III-5 Radial diffuse reflectance at $\mu_s^{'}$=1mm^{-1} and g=0.9 and four different absorptions

3.4.3 Anisotropy factor dependency of the radial diffuse reflectance in medium with reduced scattering coefficient of 1mm^{-1} and absorption coefficient of 0.01mm^{-1}

Figure III-6 presents the radial diffuse reflectance $\boldsymbol{R}(\boldsymbol{\mu_s'\rho})$over $(\boldsymbol{\mu_s'\rho})$ of [10^{-5}, 10^{0}] for a medium of$\boldsymbol{\mu_a = 0.01mm^{-1}}$ and $\boldsymbol{\mu_s'}$=1mm^{-1} with the anisotropy factor g=[0.5 0.7, 0.8, 0.9], or equivalently $\boldsymbol{\mu_s}$=[2, 3.33, 5, 10]mm^{-1}. Over $(\boldsymbol{\mu_s'\rho}) = [\boldsymbol{10^{-5}}, \boldsymbol{10^{-1}}]$, the analytical radial diffuse reflectance $\boldsymbol{R}(\boldsymbol{\mu_s'\rho})$ agrees with MC result with an error of (11.6±9.4)%. When compared to the MC result at g=0 as the reference (green markers), the radial diffuse reflectance decreases as g increases from

0.5 to 0.9 at the same value of $\boldsymbol{\mu'_s\rho}$. The difference of the radial diffuse reflectance between g=[0.5, 0.9] and g=0 diminishes as $\boldsymbol{\mu'_s\rho}$ is as high as 10^0.

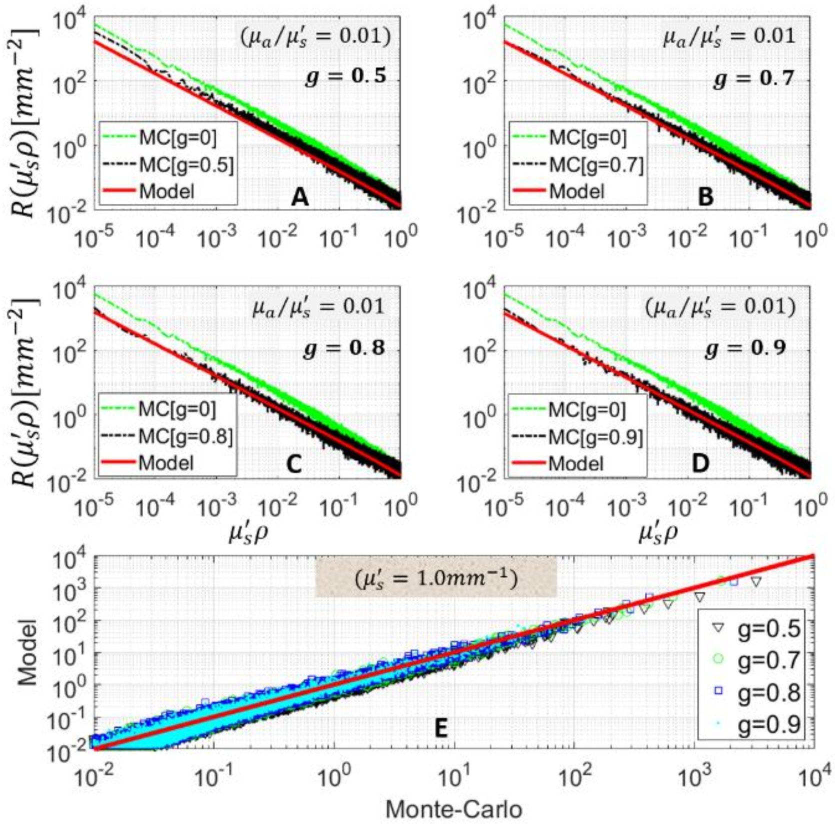

Figure III-6 Radial diffuse reflectance at μ_s'=1mm^{-1} and μ_a =0.01mm^{-1} and different g values

3.4.4 Absorption coefficient dependency of the total diffuse reflectance in isotropic scattering medium

Figure III-7 assesses the total diffuse reflectance $I(\mu_s d_{area})$ over $(\mu_s d_{area})$ of [10^{-5}, 10^0] for a medium of isotropic scattering (g=0) with μ_s=1mm^{-1}, and μ_a=[0.001, 0.01, 0.1, 1.0]mm^{-1}. The range of μ_a corresponds to an absorption to scattering ratio of [0.001, 1]. Over $(\mu_s d_{area}) = [10^{-5}, 10^{-1}]$, the analytical total diffuse reflectance $I(\mu_s d_{area})$ agrees with MC result with an average error (1.3±1.4)%. The absorption dependence of $I(\mu_s d_{area})$ over $(\mu_s d_{area})$ of [10^{-5}, 10^{-1}] is unremarkable. The shaded area in (D) and (E) marks the value of $(\mu_s d_{area}) > 10^{-1}$. The absorption dependence of $I(\mu_s d_{area})$ becomes increasingly noticeable over the shaded area as $\mu_s d_{area}$ increases.

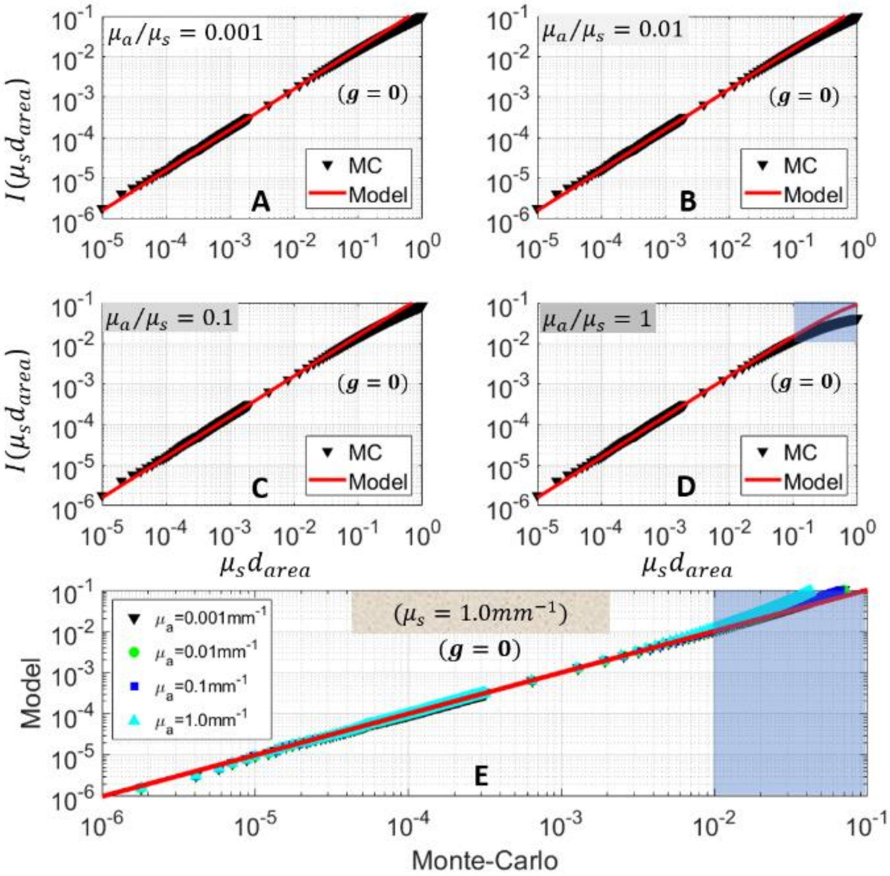

Figure III-7 Total diffuse reflectance at μ_s =1.0mm^{-1} and g=0 at different absorption

3.4.5 Absorption coefficient dependency of the total diffuse reflectance in anisotropy medium with g=0.9

Figure III-8 assesses the total diffuse reflectance $\boldsymbol{I}(\boldsymbol{\mu_s' d_{area}})$ over $(\boldsymbol{\mu_s' d_{area}})$ of [10^{-5}, 10^{0}] for a medium of $\boldsymbol{\mu_s'}$=1mm^{-1} with an anisotropy factor of g=0.9, and $\boldsymbol{\mu_a}$=[0.001, 0.01, 0.1, 1.0]mm^{-1}. The $\boldsymbol{\mu_a}$ varying over 3 orders of magnitude from 0.001 to 1mm^{-1} corresponds to an absorption to reduced scattering ratio of [0.001, 1]. Over $(\boldsymbol{\mu_s' d_{area}}) = [\boldsymbol{10^{-5}}, \boldsymbol{10^{-1}}]$, the analytical total diffuse reflectance $\boldsymbol{R}(\boldsymbol{\mu_s' \rho})$ agrees with MC result with an average error (1.6±2.0)%. The absorption dependence of $\boldsymbol{I}(\boldsymbol{\mu}_s'\boldsymbol{d}_{area})$ appears unremarkable over $(\boldsymbol{\mu}_s'\boldsymbol{d}_{area})$ of [10^{-5}, 10^{-1}]. When compared to the MC result at g=0 as the reference (green markers), the total diffuse reflectance is smaller for g=0.9 at the same $\boldsymbol{\mu}_s'\boldsymbol{d}_{area}$. The difference of the total diffuse reflectance between g=0.9 and g=0 decreases as $\boldsymbol{\mu}_s'\boldsymbol{d}_{area}$ increases to 10^0.

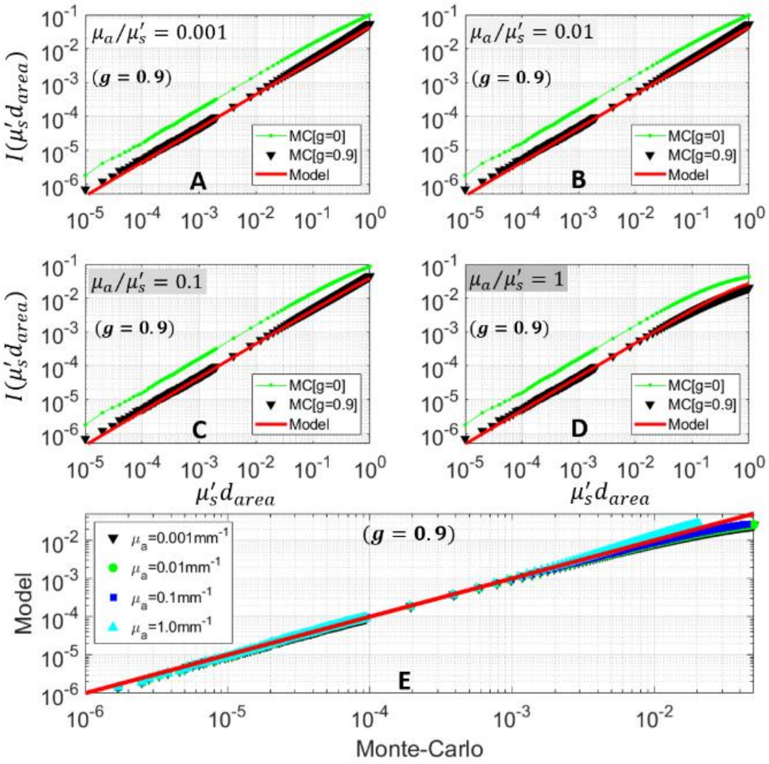

Figure III-8 Total diffuse reflectance at μ_s'=1mm^{-1} and g=0.9 and different absorption

3.4.6 Anisotropy factor dependency of the total diffuse reflectance from medium with reduced scattering coefficient of 1mm^{-1} and absorption coefficient of 0.01mm^{-1}

Figure III-9 assesses the total diffuse reflectance $\boldsymbol{I}(\boldsymbol{\mu}_s'\boldsymbol{d}_{area})$ over $(\boldsymbol{\mu}_s'\boldsymbol{d}_{area})$ of [10^{-5}, 10^0] for a medium of $\boldsymbol{\mu_a = 0.01mm^{-1}}$ and $\boldsymbol{\mu}_s'$=1mm^{-1} with the anisotropy factor g=[0.5 0.7, 0.8, 0.9], or equivalently $\boldsymbol{\mu_s}$=[2, 3.33, 5, 10]mm^{-1}. Over $(\boldsymbol{\mu}_s'\boldsymbol{d}_{area}) = [\boldsymbol{10^{-5}}, \boldsymbol{10^{-1}}]$, the analytical total diffuse reflectance $\boldsymbol{I}(\boldsymbol{\mu}_s'\boldsymbol{d}_{area})$ agrees with MC result with an average error (16.1±5.0)%. When compared to the MC result at g=0 as the reference, the total diffuse reflectance decreases slightly as g increases from 0.5 to 0.9 for the same value of $\boldsymbol{\mu_s' d_{area}}$. As $\boldsymbol{\mu_s' d_{area}}$ reaches $\mathbf{10^0}$, the difference of the total diffuse reflectance between g=[0.5, 0.9] and g=0 decreases slowly.

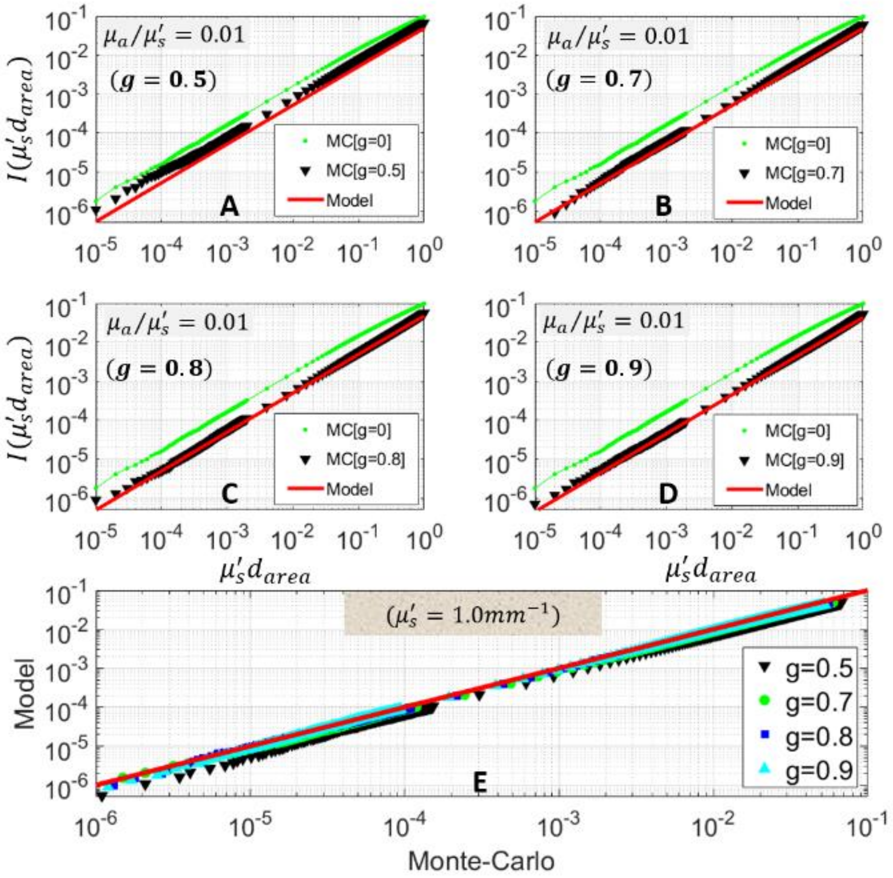

Figure III-9 Total diffuse reflectance at μ_s' =1mm^{-1} and μ_a =0.01mm^{-1} and different g

3.4.7 Absorption coefficient dependency of the total diffuse reflectance collected via d_{area}=1mm from isotropic scattering medium

Figure III-10 presents the total diffuse reflectance over ($\boldsymbol{\mu_s d_{area}}$) of [$10^{-5}$, 10^{0}] for an isotropic medium and a fixed collection area of $\boldsymbol{d_{area}}$=1mm, at $\boldsymbol{\mu_a}$ of respectively 0.001, 0.01, 0.1, and 1mm^{-1}. At $\boldsymbol{d_{area}}$=1mm, the range of ($\boldsymbol{\mu_s d_{area}}$)=[$10^{-5}$, 10^{0}] corresponds to an absorption to scattering ratio of respectively [0.001, 100] for $\boldsymbol{\mu_a}$ =0.001mm^{-1}, [0.01, 1000] for $\boldsymbol{\mu_a}$ =0.01mm^{-1}, [0.1, 10000] for $\boldsymbol{\mu_a} = 0.1\text{mm}^{-1}$, and [1, 100000] for $\boldsymbol{\mu_a} = 1\text{mm}^{-1}$. The analytical evaluation is implemented with the aforementioned conversion.

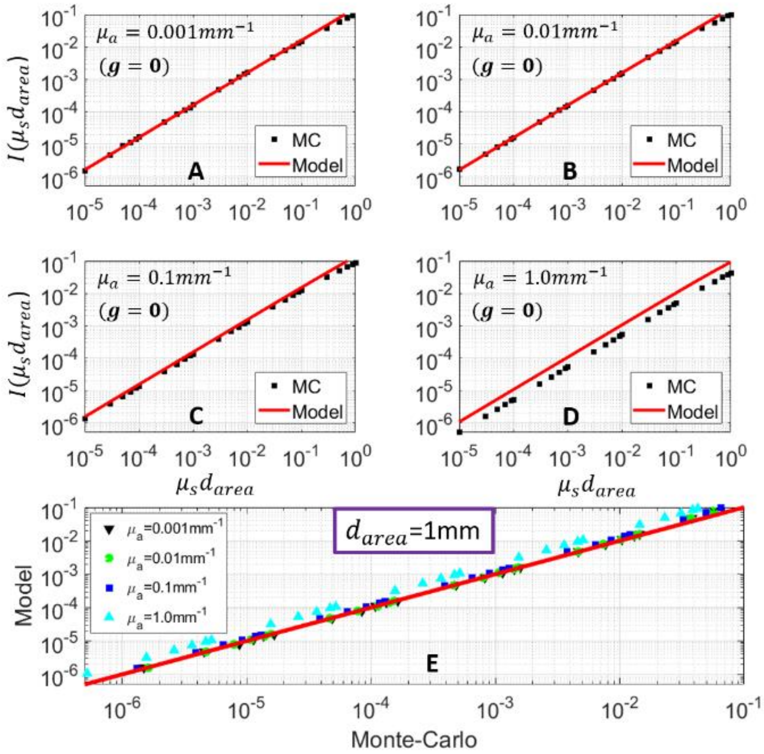

Figure III-10 Total diffuse reflectance for d_{area}=1mm and g=0 and different absorptions

For example, the total diffuse reflectance associated with $\boldsymbol{\mu_s = 0.001mm^{-1}}$ and $\boldsymbol{d_{area}}$=1mm producing $\boldsymbol{\mu_s d_{area}}$ of 0.001 is calculated with Eq. (3.14) by setting $\boldsymbol{\mu_s = 1mm^{-1}}$ and $\boldsymbol{d_{area}}$=0.001mm to keep the same $\boldsymbol{\mu_s d_{area}}$ of 0.001, with $\boldsymbol{\mu_a}$ unaltered. Over $(\boldsymbol{\mu_s d_{area}}) = [\boldsymbol{10^{-5}}, \boldsymbol{10^{-1}}]$, the analytical total diffuse reflectance $\boldsymbol{I}(\boldsymbol{\mu_s d_{area}})$ agrees with MC result with an average error (31.5±1.4)% if counting the 4 values of $\boldsymbol{\mu_a}$ up to 1mm^{-1}. The error of the analytical total diffuse reflectance $\boldsymbol{I}(\boldsymbol{\mu_s d_{area}})$ with respect to MC result improves to (7.2±1.5)% if counting the $\boldsymbol{\mu_a}$ up to 0.1mm^{-1}.

3.4.8 Absorption coefficient dependency of the total diffuse reflectance collected via d_{area}=1mm from anisotropic scattering medium with g = 0.9

Figure III-11 presents the total diffuse reflectance over ($\mu_s' d_{area}$) of [10^{-5}, 10^{0}] for a medium of g=0.9 and a fixed collection area of d_{area}=1mm, at μ_a of respectively 0.001, 0.01, 0.1, and 1mm^{-1}.

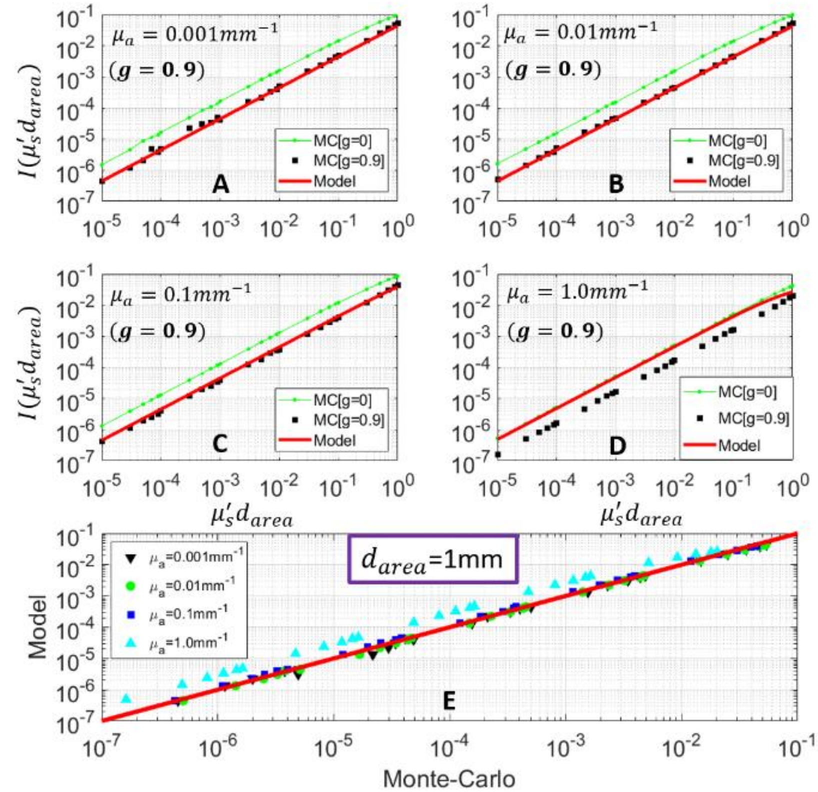

Figure III-11 Total diffuse reflectance for d_{area}=1mm and g=0.9 and different absorptions

At $\boldsymbol{d_{area}}$=1mm, the range of ($\boldsymbol{\mu_s' d_{area}}$)=[$10^{-5}$, 10^{0}] corresponds to an absorption to reduced-scattering ratio of respectively [0.001, 100] for $\boldsymbol{\mu_a}$ =0.001mm^{-1}, [0.01, 1000] for $\boldsymbol{\mu_a}$ =0.01mm^{-1}, [0.1, 10000] for $\boldsymbol{\mu_a}$ =0.1mm^{-1}, and [1, 100000] for $\boldsymbol{\mu_a}$ =1mm^{-1}. The analytical evaluation is implemented with the aforementioned conversion. For example, the total diffuse reflectance associated with $\boldsymbol{\mu_s' = 0.001mm^{-1}}$ and $\boldsymbol{d_{area}}$=1mm producing $\boldsymbol{\mu_s' d_{area}}$ of 0.001 is calculated with Eq. (19) by setting $\boldsymbol{\mu_s' = 1mm^{-1}}$ and $\boldsymbol{d_{area}}$=0.001mm to keep the same $\boldsymbol{\mu_s' d_{area}}$ of 0.001, with $\boldsymbol{\mu_a}$ unaltered. Over $(\boldsymbol{\mu_s' d_{area}}) = [\boldsymbol{10^{-5}}, \boldsymbol{10^{-1}}]$, the analytical total diffuse reflectance $\boldsymbol{I(\mu_s d_{area})}$ agrees with MC result with an average error (47.4±7.0)% if counting the 4 values of $\boldsymbol{\mu_a}$ up to 1mm^{-1}. The error of the analytical total diffuse reflectance $\boldsymbol{I(\mu_s' d_{area})}$ with respect to MC result improves to (0.4±5.7)% if counting the $\boldsymbol{\mu_a}$ up to 0.1mm^{-1}.

3.5 Discussions

The relative scale between the size of the collection area and the scattering pathlength in tissue is particularly relevant to tissue probing over a small size such as using ultra-fine fiber or over an ultra small angle like that using common-path optical-projection inside an instrument channel. For $\boldsymbol{\mu_s' = 1mm^{-1}}$ that is common to soft-tissue, the reduced scattering pathlength scaled dimension $(\boldsymbol{\mu_s' d_{area}}) = 10^0$ corresponds to a collection diameter of 1mm. Over a sub-diffusive scale of $(\boldsymbol{\mu_s' d_{area}})$=[$10^{-5}$ 10^{-1}] from a turbid medium with the HG scattering anisotropy, MC assessment of this work has identified a consistent pattern of the total diffuse reflectance: it increases nearly linearly with respect to $(\boldsymbol{\mu_s' d_{area}})$ or equivalently $(\boldsymbol{\mu_s d_{area}})$. The total diffuse reflectance increasing nearly linearly with respect to $\boldsymbol{\mu_s' d_{area}}$ over the scale shown corresponds uniquely to a radial diffuse reflectance that must show near-linear dependency on $(\boldsymbol{\mu_s'/\rho})$ over the same scale. The near-linear dependency of the radial diffuse reflectance on $(\boldsymbol{\mu_s'/\rho})$ when near the point-of-incidence is readily appreciable from [81] by examining the plot of $\boldsymbol{R(\rho)/[\mu_s']^2}$ versus $(\boldsymbol{\mu_s' \cdot \rho})$ =[10^{-3} 10^{-1}]. This pattern of the radial profile of the diffuse reflectance near the point-of-incidence, namely the dependency on SDS being $\boldsymbol{\rho^{-1}}$, differs significantly from the well-known pattern of the diffuse reflectance at the diffusion regime wherein the dependency on SDS is $\boldsymbol{\rho^{-2}}$. The transition of the diffuse reflectance from the SDS-dependency of $\boldsymbol{\rho^{-2}}$ over the diffusion regime to the SDS-dependency of $\boldsymbol{\rho^{-1}}$ over the sub-diffusive domain as the spatial dimension reduces is associated with lesser-and-lesser possibility of photons experiencing multiple-scattering between the point-of-incidence and the point-of-collection [87, 88]. At single-scattering case, the dependence of the diffuse reflectance on SDS as $\boldsymbol{\rho^{-1}}$ has been derived with single-scattering solution to RT in infinite medium [89]. Further reduction of the scattering-scaled dimension may lead to the radial diffuse reflectance to be weighted more by the ballistic peak. The total diffuse reflectance, however, may be insensitive to the ballistic peak due to the weighting of the radial profile by the area associate with the radial dimension.

The same range of the dimensionless scattering or dimensionless size of light collection ($\boldsymbol{\mu_s' d_{area}}$) for evaluating the total diffuse reflectance can be reached in two ways. One is like those implemented for Figs. 7-9 that has the scattering properties fixed so the range of ($\boldsymbol{\mu_s' d_{area}}$) represents the spatial range of the total diffuse collection. The other case is like those implemented for Figs. 10-12 that has the spatial range of the total diffuse collection fixed so the range of ($\boldsymbol{\mu_s' d_{area}}$) represents the range of the scattering properties. At the same range of ($\boldsymbol{\mu_s' d_{area}}$), one can expect that the two cases of producing the same range of ($\boldsymbol{\mu_s' d_{area}}$) will be "felt" much differently by the absorption properties of the tissue. For the first case wherein the scattering properties are fixed, the tissue scattering albedo is fixed over the range of ($\boldsymbol{\mu_s' d_{area}}$) over the spatial range of the total diffuse collection. Therefore the analytical total diffuse reflectance modeled over the spatial range of the total diffuse collection is associated with a fixed condition of tissue attenuation and consequently would perform consistently for different levels of absorption. However, for the second case wherein the spatial size of the light collection is fixed, the change of ($\boldsymbol{\mu_s' d_{area}}$) is associated with a change of the scattering albedo. For example, ($\boldsymbol{\mu_s' d_{area}}$) $=$ $[\mathbf{10^{-5}, 10^{-1}}]$ at $\boldsymbol{d_{area} = 1mm}$ and $\boldsymbol{\mu_a}$=1mm^{-1} corresponds to $\boldsymbol{\mu_s' =}$ $[\mathbf{10^{-5}, 10^{-1}}]$ mm^{-1} and thus an absorption to reduced scattering ratio varying between 0.1 where the scattering dominates and 100,000 where the absorption overwhelms. Over these large range of the tissue diffusivity, the attenuation collected over the same spatial range from a tissue of the same absorption will be unfitted by a model approach based on diffusion approximation as is implemented for the total diffuse reflectance. That explains why the model prediction for the cases of Figs. 10-12 degrades at $\mathbf{\mu_a}$=1mm^{-1}.

It must be noted that the analytical total reflectance as represented by Eq. (III.19) for a medium of HG scattering anisotropy is specific to the geometry shown in Fig. 1 that has idealized the light-introduction into the medium as a point-injection and the light collection from the medium as over a small circular-area centered on the point-of-incidence. This geometry has facilitated analytical total diffuse reflectance to be developed by integrating the radial diffuse reflectance over the area of collection. This geometry may be similar to non-contact diffuse reflectance probing using optical projections inside a small instrument channel of an endoscope or remote sensing over a large distance. This geometry, however, differs from the actual geometry of single-fiber probing which has the light-illumination area overlapping completely with the light-collection area. A more accurate analytical total diffuse reflectance for tissue probing using a single-fiber probe will require double-integration involving the light injection distributed over the probe area and the spatially-resolved diffuse reflectance associated with each element of the light

injection distribution over the probe area. Therefore, the model approach of this work may not be directly translated to single-fiber probing. However, the characteristics of the total diffuse reflectance identified by this work over the reduced scattering pathlength scaled diameter <10^{-1} will be informative to understanding some qualitative patterns salient to single-fiber probing. For example, why the rate of change of the total diffuse reflectance seems to be linear with respect to the dimensionless scattering when small, and why the total diffuse reflectance is greater for smaller anisotropy for the same value of the dimensionless reduced scattering. The total diffuse reflectance in this work is evaluated in association with the HG phase function only due to MC resource. Analytical total diffuse reflectance from medium with non-HG scattering anisotropy can be expected to have the g-dependency different from that of Eq. (III.19). Since the integration of the radial diffuse reflectance over the area of collection essentially low-pass filters the local higher-order variation [28] of the scattering distribution, the total diffuse reflectance will respond to the global slower change of the scattering distribution which is accounted for at the first-order by the anisotropy factor g. Therefore, for a collection dimension that is sub-diffusive as is assessed herein, the total diffuse reflectance can be expected to be not much sensitive to the higher-order phase function and may still be modeled with Eq. (III.15-19) by adjusting the empirical parameters. Regardless of the higher-order details of the scattering anisotropy, the analytical total diffuse reflectance corresponding to an anisotropy must analytically approach the total diffuse reflectance for isotropic scattering as indicated by Eq. (III.14) when the anisotropy disappears.

With many limitations to address in future studies, this work may provide insights for analytical understanding of ultra-small-scale probing of steady-state tissue properties. These applications have been characterized with empirical models, but further understanding of some salient features, such as the saturation pattern, the condition of saturation, etc., cannot be adequately understood without analytically-originated analysis. Analytical, thus better understanding of the tissue measurement will also be important for optimizing instrument for interrogation of specific tissue properties. The approach to analytical total diffuse reflectance over sub-diffusive scale as demonstrated may also be extendable to time-resolved configuration and fluorescence detection.

3.6 Summary

We demonstrated analytical steady-state total diffuse reflectance over a $1/\boldsymbol{\mu_s'}$scaled dimension of [10^{-5}, 10^{-1}] centered at the point-of-incidence from a semi-infinite medium with an HG anisotropy. Two constraints are abided to: (1) The total diffuse reflectance is the integration of the radial diffuse reflectance; (2) The radial and total diffuse reflectance at g>0 must resort to their respective values corresponding to isotropic-scattering as g becomes zero. Steady-state radial diffuse reflectance near the point-of-incidence from a semi-infinite medium of $\boldsymbol{g} \approx \mathbf{0}$ is developed, and the radial diffuse reflectance for $\boldsymbol{g} \geq \mathbf{0.5}$ is semi-empirically formulated by referring to the former one. The integration of each leads to the corresponding total diffuse reflectance. When compared to MC results over ($\boldsymbol{\mu_s' d_{area}}$)=[$10^{-5}$, 10^{-1}], g = [0.5, 0.95] and $\boldsymbol{\mu_a}$ = [0.001, 1]mm^{-1}, the analytical total diffuse reflectance has an error < 16.1%.

CHAPTER IV

TOTAL DIFFUSE REFLECTANCE ASSOCIATED WITH A CENTER-ILLUMINATION AND AREA-COLLECTION ROUND GEOMETRY FOR PROBING MEDIUM WITH HEYNEY-GREENSTEIN SCATTERING PHASE FUNCTION: AN INTEGRATION-BASED ANALYTICAL MODEL OF STEADY-STATE MEASUREMENT

4.1 Introduction

Diffuse reflectance is a simple method for assessing turbid medium by surface or interstitial measurement for biological[14], pharmaceutical[90], and agricultural [91, 92] needs. Diffuse reflectance assessment of the sub-surface medium properties, whether for steady-state evaluation of abnormalities[12] or for temporal monitoring of functions[17], often is implemented in a total-diffuse reflectance mode that collects the photon remission over the area of the collecting aperture, that may or may not be overlapping with the area of light illumination on the interface with tissue. Device level variations of the total-diffuse reflectance are many: (1) the illumination area completely overlaps with the collection area which can be realized by setting up common-path via a beam-splitter[10] or by coupling two smaller fibers with a larger fiber for interfacing with tissue[12]; (2) the illumination position is asymmetrically offset from the collection area ; (3) the illumination area centers the collection aperture or the collection area centers the illumination aperture [93, 94]. All these configurations of total diffuse reflectance can be instrumented with small profile for point-of-care assessment, but a geometry-specific light-tissue interaction model is always needed for practical applications.

The spatially resolved diffuse reflectance, even at a single wavelength could accurately inform tissue effective attenuation. In comparison, the total diffuse reflectance relies upon the spectral variation acquired over a fixed probing geometry to estimate tissue properties. An accurate forward model is crucial to recovering physiologically meaningful range of parameters such as oxygenation saturation[10] by diffuse reflectance. The exact analytical solution of light propagation in biological tissue does not exist [31], nor does the total diffuse reflectance. As a result, Monte Carlo (MC) simulation is the primary tool for modeling total diffuse reflectance, especially when the tissue probing is over a sub-diffusion scale. However, the statistical demand of assembling large amount of random events makes MC ill-suited for point-of-care rapid forward computation. Algebraic (approximate) form of the total diffuse reflectance is thus sought[31, 93] to complement Monte Carlo simulations. An analytical form of the total diffuse reflectance is not only more rapid to use than MC, it may also help identify characteristic patterns of total diffuse reflectance, such as the tissue-probe conditions at which the signal will be sensitive and insensitive to the tissue property change. With an accurate algebraic solution, it may thus be possible to identify the causes of any characteristic patterns of measurements, and knowing those patterns and their causes may translate to better understanding of the applicability or limitation of the device for biological tissue sampling.

The total diffuse reflectance is the diffuse reflectance over the entire area of collection. Analytically it is thus the integration of the spatially resolved diffuse reflectance over the entire area of collection, regardless of overlapping or non-overlapping between the light illumination and collection area. An analytical form of the total diffuse reflectance can thus be expected, if there exists an accurate analytical form of the spatially resolved diffuse reflectance specific to the light illumination and collection geometry of concern. The realistic use of total diffuse reflectance in tissue-probing always involves area illumination with certain intensity profile such as gaussian, top hat, donut or even more complex [thorlab], and besides, the illumination area may not be completely overlapping with the collection area or may be asymmetric to collection area. Thus pencil beam illumination, as the simplest light illumination geometry, is of fundamental significance due to superposition principle: by breaking down the illumination area to a collection of pencil beams with weighted intensity, the spatially resolved diffuse reflectance of any arbitrary area illumination and area collection type is a sum of all individual pencil beam induced spatially resolved diffuse reflectance, since biological tissue is linear system. However, calculating the spatially resolved diffuse reflectance of area-illumination type from the fundamental pencil beam type is quite difficult, and so far no literature has reported any solution even to a simple case of top hat circular area illumination completely overlapping with collection area. Even though the above problem is analytically solved and a spatially resolved diffuse reflectance of area-illumination type is available, the further 2-dimension integration over the collection area may result in a bulky form of total diffuse reflectance that is not practical to use.

Considering pencil beam as one extreme case of Gaussian type area-illumination and placed at the center of a round collection area, the total diffuse reflectance associated with this center-illumination and area-collection round (CIACR) geometry as shown in Fig 1, is worth to explore. First, it offers the mathematic feasibility to analytically derive a close form of total diffuse reflectance specific to this CIACR geometry. Second, the aforementioned total diffuse reflectance, shall provide some common features with the general case of area-illumination and area-collection round geometry (AIACR), such as anisotropy-sensitive zone, scattering-sensitive zone and scattering-insensitive zone, thus shines some insights into the analytical understanding of those observed features. Third, the derived total diffuse reflectance of CIACR geometry may potentially work as an approximated analytical solution in practice to retrieve meaningful physiological parameters from data acquired from AIACR geometry.

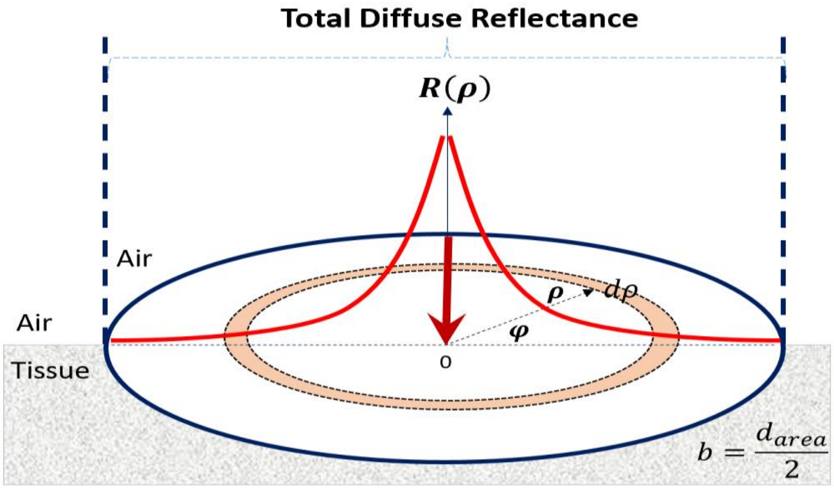

Figure IV-1 The total diffuse reflectance specific to the center-illumination and area-collection round geometry

This work aims to model the total diffuse reflectance specific to the center-illumination and area-collection round geometry as illustrated in Figure IV-1 and detailed as below: A semi-infinite homogeneous tissue is bounded with air. On the interface, a steady-state directional point light source is placed right at the center of a circular collection area with diameter d_{area}, injecting photons into tissue normal to interface. The total diffuse reflectance is counted by including all photons remitting within the collection area, regardless of their various incident angles.

It is still difficult to model the spatially resolved diffuse reflectance in CIACR geometry with diffusion theory, due to the need to cross the sub-ballistic to sub-diffusion scale (10s microns to a few millimeters). The conventional diffusion approach fails to model the aggressive peaking of the diffuse reflectance towards the point-of-entry [7-9, 10] when compared to accurate measurements [3, 4]. Several analytical methods for modified diffusion approach have enhanced modeling of the diffuse reflectance at spatial dimensions close to the point-of-entry [11, 12, 13, 14], among which there are methods incorporating multiple isotropic sources [12, 13, 14]. A simple master-slave dual-source configuration [14] produces the rapid peaking of the diffuse reflectance toward the point-of-entry by using a slave source whose position and intensity are controlled by a master source that dominates the diffuse reflectance at the diffusion regime. This model of spatially resolved diffuse reflectance has shown to be valid for a semi-infinite medium over a source-detector-separation (SDS) as small as 1/10 of $1/\mu_s'$, for instance SDS larger than 100µm for $\mu_s' = 1mm^{-1}$. To arrive at an accurate integral solution of the total diffuse reflectance, the spatially resolved diffuse reflectance at SDS much small than 1/10 of $1/\mu_s'$ is needed. The spatially resolved reflectance at SDS close to one transport mean free path has also been shown to be predictable with μ_a, μ_s', and the moments of the Heyney-Greenstain (HG) phase function. As far as the authors knows, there is no single model that can accurately quantify the spatially resolved diffuse reflectance from a sub-ballistic domain (i.e., near the point-of-entry) to a sub-diffusive regime (i.e. near millimeter).

This work introduces a concatenation strategy to construct a model of spatially resolved diffuse reflectance that works for long range of SDS covering sub-ballistic, sub-diffusive and diffusive region. One semi-empirical model that was developed for sub-ballistic to sub-diffusive SDS range [1/10,000, 1] of $1/\mu_s'$ using μ_a, μ_s', and g (the anisotropy of HG phase function), is concatenated with the aforementioned master-slave model that was validated at SDS range beyond 1/10 of $1/\mu_s'$, to make a final form of spatially resolved diffuse reflectance model working at SDS ranging from [1/10,000, 1000] of $1/\mu_s'$. The integration of the above spatially resolved diffuse reflectance gives rise to an analytical form of the total diffuse reflectance with infinite numerical aperture. After being slightly adapted for practical use in a broad range of tissue optical parameters and different sizes of collection area , the model was then compared against Monte-Carlo simulated results of same CIACR geometry in a total amount of 4368 sceneries covering $\mu_a = [0.001 - 1.0]mm^{-1}, \mu_s' = [0.01 - 1000]mm^{-1}, g = [0.5 - 0.95]$, and diameter of collection area $d_{area} = [50 - 1000]\mu m$ for forward model evaluation. A pilot phantom experiment was also conducted to test the model's effectiveness in reserve problem solving in context of AIACR geometry, during which the effect of limited numerical aperture of a realistic fiber was added into consideration.

4.2 Theory and methodology

4.2.1 Spatially resolved diffuse reflectance

We consider two regions of the circular area for spatially resolved diffuse reflectance associated with pencil beam illumination. The two areas as illustrated in Figure IV-2 contain an inner-field centered at and adjacent to the center illumination point, and an outer-field that is co-centric and encloses the inner-field. The radius that borders the inner-field from outer-field is defined as a dimensionless number δ when scaled versus $z_a = 1/\mu_s'$ [unit: mm], namely $\rho = \delta/\mu_s'$, where the dimensionless δ can vary from 0.1 and 1.0 and is set as 0.5 in this work to reach the best model performance. The outer radius of the outer area $b = \mathrm{d_{area}}/2$ [unit: mm] is defined as a dimensionless number ξ when scaled versus $z_a = 1/\mu_s'$.

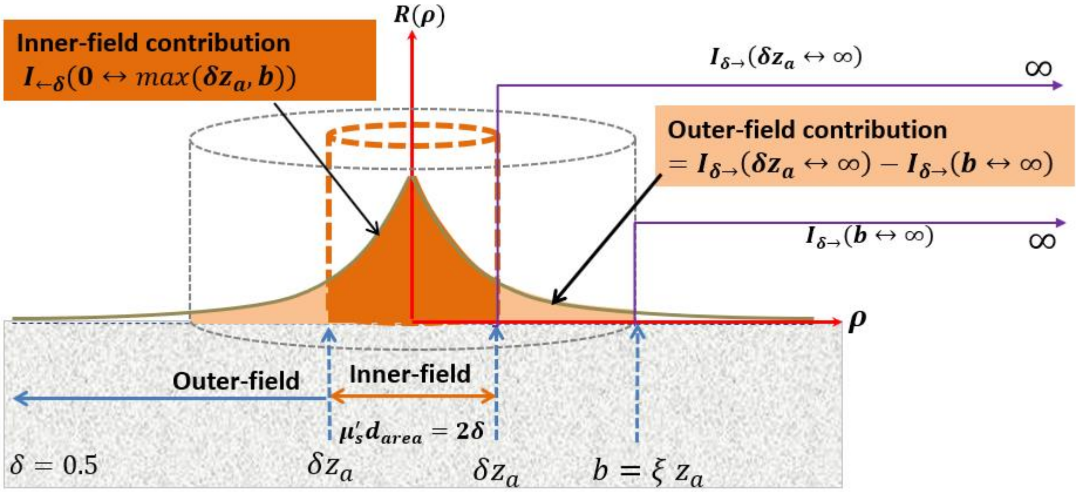

Figure IV-2 The area of collection contains an inner-field of a diameter of $2\delta \mathrm{z_a}$ and an out-field covering the space elsewhere.

The tissue properties concerning diffuse reflectance include refractive index n_{tiss}, absorption coefficient μ_a [unit: mm^{-1}], scattering coefficient μ_s [unit: mm^{-1}], anisotropy factor g following the Henyey-Greenstein (HG) phase function that gives $\mu_s' = \mu_s(1-g)$ [unit: mm^{-1}], diffusion coefficient $D = 1/[3(\mu_a + \mu_s')]$ [unit: mm], and effective attenuation coefficient $\mu_{eff} = \sqrt{\mu_a/D}$ [mm^{-1}]. The light illumination of unit intensity occurs at the center of the round geometry. The model of the spatially resolved diffuse reflectance for the inner-field is derived semi-empirically by fitting to MC simulations and consulting a form representing the upper limit of the diffuse reflectance associated with a tissue of isotropic scattering (see **APPENDIX**). The modeling of the spatially resolved diffuse reflectance in the outer-field involves a master-slave dual-source approach as shown in Figure IV-3. For the point illumination, a master-source [14] of intensity S=1 [unit: W·mm^{-3}] is set at a depth of $z_a = 1/\mu_s'$. A slave-source index is defined [14] as $\eta(g) = [g \cdot exp(1-g)]^{1/10}$. Then the slave-source is set at a depth of $z_a^* = (1-g)^2(1-\eta)z_a = \alpha z_a$ [unit: mm], and the intensity of the slave source is $S^* = \eta \cdot S \cdot exp\left[-\mu_{eff}\, z_a(1+\alpha)/2\right]$ [unit: W·mm^{-3}]. The medium-air boundary is accounted for by the extrapolated zero-boundary [15] that is set at a distance of $z_b = 2AD = \beta z_a$ [unit: mm] away from medium surface, where $A = (1+\xi)/(1-\xi)$, and $\xi = -1.44 {n_{tiss}}^{-2} + 0.710 {n_{tiss}}^{-1} + 0.668 + 0.0636 n_{tiss}$. For a position on the tissue-air interface of a distance of ρ [unit: mm] from the source, the following lengths [unit: mm] are defined:

$$\mathrm{l_{real}} = \sqrt{\rho^2 + z_a^2} \tag{IV-1}$$

$$\mathrm{l_{imag}} = \sqrt{\rho^2 + z_a^2(1+2\beta)^2} \tag{IV-2}$$

$$\mathrm{l_{real}^*} = \sqrt{\rho^2 + z_a^2\alpha^2} \tag{IV-3}$$

$$\mathrm{l_{imag}^*} = \sqrt{\rho^2 + z_a^2(\alpha+2\beta)^2} \tag{IV-4}$$

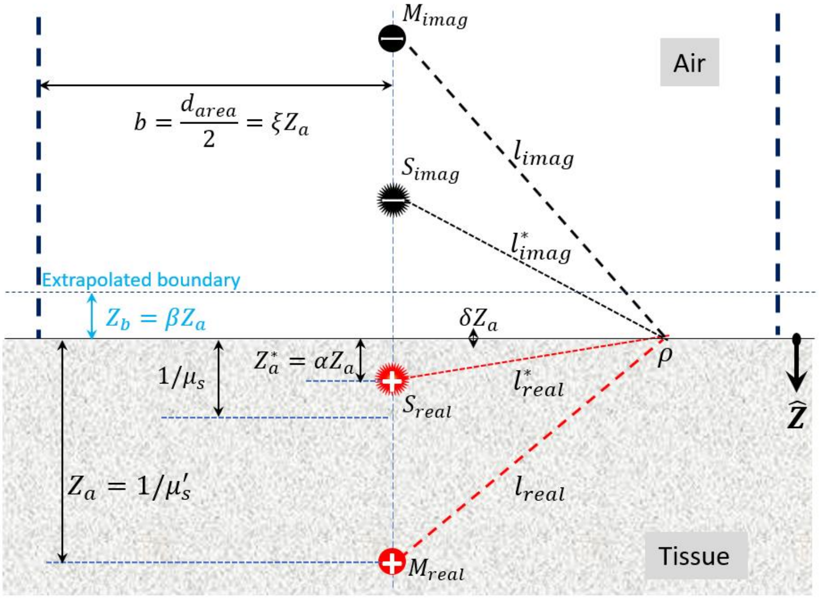

Figure IV-3 The master and slave sources dual sources configuration [14]

The spatially resolved diffuse reflectance for the inner field is denoted as $\mathrm{R}_{\leftarrow\delta}(\rho, \mu_a, \mu'_s, g)$. Appendix A gives the semi-empirical $\mathrm{R}_{\leftarrow\delta}(\rho)$ as the following

$$\mathrm{R}_{\leftarrow\delta}(\rho) = \frac{0.75^g}{2\pi} 10^{-(1+p_1\gamma)} \frac{{\mu_s}^2(1-g)^g}{(\mu_s\rho)^{1+p_2\gamma}} \exp(-\gamma) \qquad \text{(IV-5)}$$

Where $p_1 = 1.25, p_2 = 1$ and $\gamma = 2(\mu_a/\mu_s)$. This semi-empirical inner-field model was validated by comparing against monte-carlo simulated spatially resolved diffuse reflectance over the range of $\rho\mu'_s = [0.0001,1]$ under following tissue optical properties: $\mu_a = [0.001,0.01,0.1,1.0]mm^{-1}$, g=[0.5, 0.6, 0.7, 0.8, 0.9, 0.95] and a fixed $\mu'_s = 1mm^{-1}$. In section 2.2, Eq. (5) is used to analytically derive the initial form of total diffuse reflectance through integration. In section 2.3, we will introduce an adaption approach in which p_1 and p_2 are slightly modified, to expand the use of the integral model for a broad range of tissue optical properties and sizes of collection area.

The spatially resolved diffuse reflectance for the "outer-field" is denoted as $\mathrm{R}_{\delta\rightarrow}(\rho,\mu_a,\mu_s',g)$ which takes the following form [14]:

$$\mathrm{R}_{\delta\rightarrow}(\rho,\mu_a,\mu_s',g)=\mathrm{R}_{\Psi}(\rho,\mu_a,\mu_s',g)+\mathrm{R}_{\Psi^*}(\rho,\mu_a,\mu_s',g)+\mathrm{R}_{\mathrm{Jz}}(\rho,\mu_a,\mu_s',g)+\mathrm{R}_{\mathrm{JZ}^*}(\rho,\mu_a,\mu_s',g) \tag{IV-6}$$

Where the four terms represent respectively the contribution to the diffuse reflectance by the fluence rate due to the master source, the fluence rate due to the slave source, the normal flux component due to the master source, and the normal flux component due to the slave source. The four terms of Eq. (6) are defined respectively as the following [14]:

$$\mathrm{R}_{\Psi}(\rho,\mu_a,\mu_s',g)=\frac{1}{8\sqrt{2}\pi}\,\frac{1}{2\pi}\frac{1}{\mathrm{D}}\left[\frac{\exp(-\mu_{\mathrm{eff}}l_{\mathrm{real}})}{l_{\mathrm{real}}}-\frac{\exp(-\mu_{\mathrm{eff}}l_{\mathrm{imag}})}{l_{\mathrm{imag}}}\right] \tag{IV-7}$$

$$\mathrm{R}_{\Psi^*}(\rho,\mu_a,\mu_s',g)=\frac{1}{8\sqrt{2}\pi}\frac{1}{2\pi}\frac{\mathrm{S}^*}{\mathrm{D}}\left[\frac{\exp(-\mu_{\mathrm{eff}}l_{\mathrm{real}}^*)}{l_{\mathrm{real}}^*}-\frac{\exp\left(-\mu_{\mathrm{eff}}l_{\mathrm{imag}}^*\right)}{l_{\mathrm{imag}}^*}\right] \tag{IV-8}$$

$$\mathrm{R}_{\mathrm{Jz}}(\rho,\mu_a,\mu_s',g)=\frac{3}{8\sqrt{2}\pi}\,\frac{1}{2\pi}\Big[\frac{z_{\mathrm{a}}(\mu_{\mathrm{eff}}l_{\mathrm{real}}+1)\exp(-\mu_{\mathrm{eff}}l_{\mathrm{real}})}{(l_{\mathrm{real}})^3}$$

$$+\frac{(z_{\mathrm{a}}+2z_{\mathrm{b}})\left(\mu_{\mathrm{eff}}l_{\mathrm{imag}}+1\right)\exp\left(-\mu_{\mathrm{eff}}l_{\mathrm{imag}}\right)}{\left(l_{\mathrm{imag}}\right)^3}\Big] \tag{IV-9}$$

$$\mathrm{R}_{\mathrm{JZ}^*}(\rho,\mu_a,\mu_s',g)=\frac{3}{8\sqrt{2}\pi}\,\frac{1}{2\pi}\,\mathrm{S}^*\Big[\frac{z_{\mathrm{a}}^*\left(\mu_{\mathrm{eff}}l_{\mathrm{real}}^*+1\right)\exp\left(-\mu_{\mathrm{eff}}l_{\mathrm{real}}^*\right)}{\left(l_{\mathrm{real}}^*\right)^3}$$

$$+\frac{(z_{\mathrm{a}}^*+2z_{\mathrm{b}})\left(\mu_{\mathrm{eff}}l_{\mathrm{imag}}^*+1\right)\exp\left(-\mu_{\mathrm{eff}}l_{\mathrm{imag}}^*\right)}{\left(l_{\mathrm{imag}}^*\right)^3}\Big] \tag{IV-10}$$

The concatenation of the inner-field model $\mathrm{R}_{\leftarrow\delta}(\rho)$ and the outer-field $\mathrm{R}_{\delta\rightarrow}(\rho)$ model produces the spatially resolved diffuse reflectance $\mathrm{R}(\rho)$ [unit: W·mm^{-2}·sr^{-2}] in a level-set form as:

$$\mathrm{R}(\rho,\mu_a,\mu_s',g)=\mathrm{R}_{\leftarrow\delta}(\rho,\mu_a,\mu_s',g)[\mathrm{u}(\rho)-\mathrm{u}(\rho-\delta z_{\mathrm{a}})]+\mathrm{R}_{\delta\rightarrow}(\rho,\mu_a,\mu_s',g)\mathrm{u}(\rho-\delta z_{\mathrm{a}}) \tag{IV-11}$$

Where $\mathrm{u}(\rho)$ is the Heaviside step function. When $\rho\leq\delta z_{\mathrm{a}}$, only the first term stays in Equation (IV.11)

4.2.2 Total diffuse reflectance as the integration of the spatially resolved diffuse reflectance over the area of collection

The total diffuse reflectance over an area of radius of $\mathrm{b} = \mathrm{d_{area}}/2$ with the illumination of unity-intensity injected at the center of the area is:

$$I_{0\leftrightarrow\mathrm{b}}(\mu_a, \mu_s', g) = \int_0^{2\pi}\int_0^{\mathrm{b}} \mathrm{R}(\rho, \mu_a, \mu_s', g)\cdot\rho\cdot \mathrm{d}\rho\, \mathrm{d}\varphi$$

$$= 2\pi\cdot\left[\int_0^{\infty} \mathrm{R}(\rho, \mu_a, \mu_s', g)\cdot\rho\cdot \mathrm{d}\rho - \int_{\mathrm{b}}^{\infty} \mathrm{R}(\rho, \mu_a, \mu_s', g)\cdot\rho\cdot \mathrm{d}\rho\right] \tag{IV-12}$$

If $b = \xi \mathrm{z_a} \leq \delta z_a$, or $\xi \leq \delta$, Eq. (12) becomes

$$I_{0\leftrightarrow\xi\mathrm{z_a}}(\mu_a, \mu_s', g) = 2\pi\cdot\int_0^{\xi\mathrm{z_a}} \mathrm{R}_{\leftarrow\delta}(\rho, \mu_a, \mu_s', g)\cdot\rho\cdot \mathrm{d}\rho$$

$$= 0.75^{g}10^{-(1+p_1\gamma)}(1-g)^{g}\exp(-\gamma)\frac{1}{1-p_2\gamma}\left(\frac{\xi}{1-g}\right)^{1-p_2\gamma} \tag{IV-13}$$

We define a function $I_{\mathrm{x}\leftrightarrow\infty}(\mu_a, \mu_s', g)$ as the following for $\mathrm{x} \geq 0$:

$$I_{\mathrm{x}\leftrightarrow\infty}(\mu_a, \mu_s', g) = 2\pi\cdot\int_{\mathrm{x}}^{\infty} \mathrm{R}(\rho, \mu_a, \mu_s', g)\cdot\rho\cdot \mathrm{d}\rho \tag{IV-14}$$

So if $b = \xi \mathrm{z_a} > \delta z_a$, or $\xi > \delta$,

$$I_{0\leftrightarrow\xi\mathrm{z_a}}(\mu_a, \mu_s', g) = 2\pi\cdot\left[\int_0^{\delta\mathrm{z_a}} \mathrm{R}_{\leftarrow\delta}(\rho, \mu_a, \mu_s', g)\cdot\rho\cdot \mathrm{d}\rho + \int_{\delta z_a}^{\xi\mathrm{z_a}} \mathrm{R}(\rho, \mu_a, \mu_s', g)\cdot\rho\cdot \mathrm{d}\rho\right]$$

$$= 2\pi\cdot\left[\int_0^{\delta\mathrm{z_a}} \mathrm{R}_{\leftarrow\delta}(\rho, \mu_a, \mu_s', g)\cdot\rho\cdot \mathrm{d}\rho + \int_{\delta z_a}^{\infty} \mathrm{R}(\rho, \mu_a, \mu_s', g)\cdot\rho\cdot \mathrm{d}\rho - \int_{\xi\mathrm{z_a}}^{\infty} \mathrm{R}(\rho, \mu_a, \mu_s', g)\cdot\rho\cdot \mathrm{d}\rho\right]$$

$$= I_{0\leftrightarrow\delta\mathrm{z_a}}(\mu_a, \mu_s', g) + \left[I_{\delta z_a\leftrightarrow\infty}(\mu_a, \mu_s', g) - I_{\xi z_a\leftrightarrow\infty}(\mu_a, \mu_s', g)\right] \tag{IV-15}$$

Where $I_{0\leftrightarrow\delta\mathrm{z_a}}(\mu_a, \mu_s', g)$ is the Eq. (IV.13) evaluated at $\xi = \delta$, or

$$I_{0\leftrightarrow\delta\mathrm{z_a}}(\mu_a, \mu_s', g) = 0.75^{g}10^{-(1+p_1\gamma)}(1-g)^{g}\exp(-\gamma)\frac{1}{1-p_2\gamma}\left(\frac{\delta}{1-g}\right)^{1-p_2\gamma} \tag{IV-16}$$

The other two terms in Eq. (IV.15) can be decomposed to 4 items according to Eq. (IV.6 - IV.10):

$$I_{\delta z_a\leftrightarrow\infty}(\mu_a,\mu_s',g) = I^{\Psi}_{\delta z_a\leftrightarrow\infty}(\mu_a,\mu_s',g) + I^{\Psi^*}_{\delta z_a\leftrightarrow\infty}(\mu_a,\mu_s',g) + I^{\mathrm{JZ}}_{\delta z_a\leftrightarrow\infty}(\mu_a,\mu_s',g) + I^{\mathrm{JZ}^*}_{\delta z_a\leftrightarrow\infty}(\mu_a,\mu_s',g) \qquad \text{(IV-17)}$$

$$I_{\xi z_a\leftrightarrow\infty}(\mu_a,\mu_s',g) = I^{\Psi}_{\xi z_a\leftrightarrow\infty}(\mu_a,\mu_s',g) + I^{\Psi^*}_{\xi z_a\leftrightarrow\infty}(\mu_a,\mu_s',g) + I^{\mathrm{JZ}}_{\xi z_a\leftrightarrow\infty}(\mu_a,\mu_s',g) + I^{\mathrm{JZ}^*}_{\xi z_a\leftrightarrow\infty}(\mu_a,\mu_s',g) \qquad \text{(IV-18)}$$

The first terms in respectively Eq. (IV.17) and (IV.18) are

$$I^{\Psi}_{\delta z_a\leftrightarrow\infty}(\mu_a,\mu_s',g) = 2\pi\int_{\delta z_a}^{\infty} \mathrm{R}_{\Psi}(\rho,\mu_a,\mu_s',g)\,\rho d\rho = \frac{1}{8\sqrt{2}\pi D\mu_{\mathrm{eff}}}\left[\exp\left(-\mu_{\mathrm{eff}}z_a\sqrt{\delta^2+1}\right) - \exp\left(-\mu_{\mathrm{eff}}z_a\sqrt{\delta^2+(1+2\beta)^2}\right)\right] \qquad \text{(IV-19)}$$

$$I^{\Psi}_{\xi z_a\leftrightarrow\infty}(\mu_a,\mu_s',g) = 2\pi\int_{\xi z_a}^{\infty} \mathrm{R}_{\Psi}(\rho,\mu_a,\mu_s',g)\,\rho d\rho = \frac{1}{8\sqrt{2}\pi D\mu_{\mathrm{eff}}}\left[\exp\left(-\mu_{\mathrm{eff}}z_a\sqrt{\xi^2+1}\right) - \exp\left(-\mu_{\mathrm{eff}}z_a\sqrt{\xi^2+(1+2\beta)^2}\right)\right] \qquad \text{(IV-20)}$$

The second terms in respectively Eq. (IV.17) and (IV.18) are

$$I^{\Psi^*}_{\delta z_a\leftrightarrow\infty}(\mu_a,\mu_s',g) = 2\pi\int_{\delta z_a}^{\infty} \mathrm{R}_{\Psi^*}(\rho,\mu_a,\mu_s',g)\,\rho d\rho = \frac{S^*}{8\sqrt{2}\pi D\mu_{\mathrm{eff}}}\left[\exp\left(-\mu_{\mathrm{eff}}z_a\sqrt{\delta^2+\alpha^2}\right) - \exp\left(-\mu_{\mathrm{eff}}z_a\sqrt{\delta^2+(\alpha+2\beta)^2}\right)\right] \qquad \text{(IV-21)}$$

$$I^{\Psi^*}_{\xi z_a\leftrightarrow\infty}(\mu_a,\mu_s',g) = 2\pi\int_{\xi z_a}^{\infty} \mathrm{R}_{\Psi^*}(\rho,\mu_a,\mu_s',g)\,\rho d\rho = \frac{S^*}{8\sqrt{2}\pi D\mu_{\mathrm{eff}}}\left[\exp\left(-\mu_{\mathrm{eff}}z_a\sqrt{\xi^2+\alpha^2}\right) - \exp\left(-\mu_{\mathrm{eff}}z_a\sqrt{\xi^2+(\alpha+2\beta)^2}\right)\right] \qquad \text{(IV-22)}$$

The third terms in respectively Eq. (IV.17) and (IV.18) are

$$I^{\mathrm{JZ}}_{\delta z_a\leftrightarrow\infty}(\mu_a,\mu_s',g) = 2\pi\int_{\delta z_a}^{\infty} \mathrm{R}_{\mathrm{JZ}}(\rho,\mu_a,\mu_s',g)\,\rho d\rho = \frac{3}{8\sqrt{2}\pi}\left[\frac{1}{\sqrt{\delta^2+1}}\exp\left(-\mu_{\mathrm{eff}}z_a\sqrt{\delta^2+1}\right) + \frac{(1+2\beta)}{\sqrt{\delta^2+(1+2\beta)^2}}\exp\left(-\mu_{\mathrm{eff}}z_a\sqrt{\delta^2+(1+2\beta)^2}\right)\right] \qquad \text{(IV-23)}$$

$$I^{\mathrm{JZ}}_{\xi z_a \leftrightarrow \infty}(\mu_a, \mu_s', g) = 2\pi \int_{\xi \mathrm{z_a}}^{\infty} \mathrm{R_{JZ}}(\rho, \mu_a, \mu_s', g)\, \rho \mathrm{d}\rho =$$

$$\frac{3}{8\sqrt{2}\pi}\left[\frac{1}{\sqrt{\xi^2+1}}\exp\left(-\mu_{\mathrm{eff}}\mathrm{z_a}\sqrt{\xi^2+1}\right)+\frac{(1+2\beta)}{\sqrt{\xi^2+(1+2\beta)^2}}\exp\left(-\mu_{\mathrm{eff}}\mathrm{z_a}\sqrt{\xi^2+(1+2\beta)^2}\right)\right] \quad \text{(IV-24)}$$

The fourth terms in respectively Eq. (IV.17) and (IV.18) are

$$I^{\mathrm{JZ}^*}_{\delta z_a \leftrightarrow \infty}(\mu_a, \mu_s', g) = 2\pi \int_{\delta \mathrm{z_a}}^{\infty} \mathrm{R_{JZ^*}}(\rho, \mu_a, \mu_s', g)\, \rho \mathrm{d}\rho =$$

$$\frac{3S^*}{8\sqrt{2}\pi}\left[\frac{\alpha}{\sqrt{\delta^2+\alpha^2}}\exp\left(-\mu_{\mathrm{eff}}\mathrm{z_a}\sqrt{\delta^2+\alpha^2}\right)+\frac{(\alpha+2\beta)}{\sqrt{\delta^2+(\alpha+2\beta)^2}}\exp\left(-\mu_{\mathrm{eff}}\mathrm{z_a}\sqrt{\delta^2+(\alpha+2\beta)^2}\right)\right] \quad \text{(IV-25)}$$

$$I^{\mathrm{JZ}^*}_{\xi z_a \leftrightarrow \infty}(\mu_a, \mu_s', g) = 2\pi \int_{\xi \mathrm{z_a}}^{\infty} \mathrm{R_{JZ^*}}(\rho, \mu_a, \mu_s', g)\, \rho \mathrm{d}\rho =$$

$$\frac{3S^*}{8\sqrt{2}\pi}\left[\frac{\alpha}{\sqrt{\xi^2+\alpha^2}}\exp\left(-\mu_{\mathrm{eff}}\mathrm{z_a}\sqrt{\xi^2+\alpha^2}\right)+\frac{(\alpha+2\beta)}{\sqrt{\xi^2+(\alpha+2\beta)^2}}\exp\left(-\mu_{\mathrm{eff}}\mathrm{z_a}\sqrt{\xi^2+(\alpha+2\beta)^2}\right)\right] \quad \text{(IV-26)}$$

So if $b = \xi \mathrm{z_a} \leq \delta z_a$, the terminal algebraic forms of Eq. (IV.13) is used to model the total diffuse reflectance. Otherwise if $b = \xi \mathrm{z_a} > \delta z_a$, or $\xi > \delta$, the terminal algebraic forms of Eq. (IV.19–IV.26) are used to model the total diffuse reflectance according to the following combined equation:

$$I_{0\leftrightarrow \xi \mathrm{z_a}}(\mu_a, \mu_s', g) = I_{0\leftrightarrow \delta \mathrm{z_a}}(\mu_a, \mu_s', g) +$$

$$\left[I^{\Psi}_{\delta z_a \leftrightarrow \infty}(\mu_a, \mu_s', g) - I^{\Psi}_{\xi z_a \leftrightarrow \infty}(\mu_a, \mu_s', g)\right] + \left[I^{\Psi^*}_{\delta z_a \leftrightarrow \infty}(\mu_a, \mu_s', g) - I^{\Psi^*}_{\xi z_a \leftrightarrow \infty}(\mu_a, \mu_s', g)\right]$$

$$+\left[I^{\mathrm{JZ}}_{\delta z_a \leftrightarrow \infty}(\mu_a, \mu_s', g) - I^{\mathrm{JZ}}_{\xi z_a \leftrightarrow \infty}(\mu_a, \mu_s', g)\right] + \left[I^{\mathrm{JZ}^*}_{\delta z_a \leftrightarrow \infty}(\mu_a, \mu_s', g) - I^{\mathrm{JZ}^*}_{\xi z_a \leftrightarrow \infty}(\mu_a, \mu_s', g)\right] \quad \text{(IV-27)}$$

4.2.3 Adapted model of total diffuse reflectance for practical application

In practical use, total diffuse reflectance is collected via a fixed collection area that is mainly limited by optical fiber probe, to investigate the change of tissue optical properties such as reduced scattering coefficient and absorption coefficient. For biomedical application, the single solid optical fiber probe has a core diameter ranging from $100\mu m$ to $1000\mu m$, while an optical fiber bundle probe consisting of many small fibers, with part for illumination and the other for collection, could have a profile factor larger than 1 mm. The optical properties of soft biological tissue fall into following range: $\mathrm{\mu_s'} = [0.12 - 4.0]\mathrm{mm}^{-1}, \mathrm{g} = \sim 0.9, \mathrm{\mu_a} = [0.003 - 0.16]\mathrm{mm}^{-1}$, [1, 95]. This work intends to model the total diffuse reflectance collected via the first type of optical fiber probe with core diameter d_{area} in the range of [50-1000]μm, and collected from tissue with optical properties in following range: $\mu_s' = [0.01 - 1000]mm^{-1}, g = [0.5 - 0.95],\ \mu_a = [0.001 - 1.0]mm^{-1}$ to meet the need of practical use.

As mentioned in section 4.2.1, the inner-field spatially resolved model $\mathrm{R}_{\leftarrow\delta}(\rho, \mu_a, \mu_s', g)$ was validated under tissue condition with fixed $\mu_s' = 1mm^{-1}$, therefore for tissue with $\mu_s' \neq 1mm^{-1}$, it is not guaranteed that the initial form of integral model derived above will work as well as it is in $\mu_s' = 1mm^{-1}$ case. As we know, for scattering-alone medium, the total diffuse reflectance is dependent on a dimensionless term $\mu_s' d_{area}$ or d_{area} scaled by mean free scattering path $1/\mu_s'$ for clear physics understanding, regardless of different combinations of μ_s' and d_{area} within the product[xx]. This scaling effect tells that the total diffuse reflectance collected via $d_{area} = 400\mu m$ from absorption-free medium with $\mu_s' = 0.5mm^{-1}$, equals the one collected via $d_{area} = 200\mu m$ from absorption-free medium with $\mu_s' = 1.0mm^{-1}$, since the scale $\mu_s' d_{area} = 0.2$ stands same for both.

Inspired by above, we came up with following adaptation approach that could expand the usage of the initial integral model to arbitrary μ_s' case for medium with absorption. 1) Conversion: when using Eq. (IV.13) and (IV.16) to calculate the inner-field contributed total diffuse reflectance for an arbitrary case [$\forall \mu_s', d_{area}$], always equate it to calculating total diffuse reflectance for the case of $\mu_s' = 1mm^{-1}$ with new $d_{area}^{new} =$

$\mu_s' d_{area}/1mm^{-1}$ [unit: mm], while μ_a and g are kept the same. 2) Correction: modify p_1 and p_2 as $p_1 = 2d_{area} + 0.2$ and $p_2 = 0.1$ to simultaneously correct any mis-estimation of total diffuse reflectance brought by conversion with the existence of absorption. The above adaption approach could be implemented either by directly coding it into the model, or by rewriting the Eq. (IV.13) and (IV.16) as below:

$$I_{0\leftrightarrow \xi \mathrm{z_a}}(\mu_a, \mu_s', g) = 0.75^g 10^{-(1+p_1\gamma)}(1-g)^g \exp(-\gamma)\frac{1}{1-p_2\gamma}\left(\frac{\xi^{\mathrm{new}}}{1-g}\right)^{1-p_2\gamma} \tag{IV-28}$$

Where $\xi^{\mathrm{new}} = \mu_s' d_{area}/2$.

$$I_{0\leftrightarrow \delta \mathrm{z_a}}(\mu_a, g, d_{area}) = 0.75^g 10^{-(1+p_1\gamma)}(1-g)^g \exp(-\gamma)\frac{1}{1-p_2\gamma}\left(\frac{\delta}{1-g}\right)^{1-p_2\gamma} \tag{IV-29}$$

Where $p_1 = 2d_{area} + 0.2, p_2 = 0.1, \gamma = 2\mu_a(1-g)/1mm^{-1}$.

Note that after adaptation, $I_{0\leftrightarrow \xi \mathrm{z_a}}(\mu_a, \mu_s', g)$ still has dependency on μ_s' since ξ^{new} is updated based on original μ_s' value, while $I_{0\leftrightarrow \delta \mathrm{z_a}}$becomes a function of (μ_a, g, d_{area}) and does not depend on μ_s' any more since δ remains same and γ mian depends on μ_a. Numerical calculation shows that $I_{0\leftrightarrow \delta \mathrm{z_a}}$ mainly depends on μ_a and insensitive to g and d_{area} within the range evaluated in this work. As the decrease of absorption, $I_{0\leftrightarrow \delta \mathrm{z_a}}$ increases and reach the upper limit of ~0.0486 when μ_a drops to zero, which in absorption-free medium or very strong scattering medium, $I_{0\leftrightarrow \delta \mathrm{z_a}}$ contributes a constant value of ~0.0486.

For calculating outer-field contributed total diffuse reflectance, no adaptation is needed.

4.3 Materials and Methods

4.3.1 Monte-Carlo simulation

Monte-Carlo simulation has been performed on a 24-core Linux server by using the open source Monte Carlo Command Line (MCCL, v4.6.0Beta) application developed by Virtual Photonics. The same CIACR geometry as illustrated in Fig. 1 is used, where a directional point source sitting at the origin point (0,0,0) is injecting photons into semi-infinite tissue medium in steady-state mode along the positive z direction (0,0,1) and diffusely reflected photons are collected within a circular area with a radii $b = d_{area}/2$ measured from the origin point. A total of N+1 points are linearly spaced between $\rho = [0, b]$, cutting the whole collection into N concentric element areas termed as bins in monte-carlo. The area of k^{th} bin is calculated as $Bin(k) = [\pi\rho_{k+1}^2 - \pi\rho_k^2]$, where k is the integer index ranging from 1 to N, $\rho_1 = 0$ and $\rho_{N+1} = b$. As illustrated in Figure IV-4, the MC simulation produces the spatially resolved diffuse reflectance $R_{MC}(k)$ [unit:mm^{-2}] specific to each bin, defined as the number of photons collected at the k^{th} bin normalized by total amount of photons lunched into tissue then divided by the bin area $Bin(k)$. The total diffuse reflectance $I_{MC}(0 \leftrightarrow \text{b})$ is calculated by summing up the product of $R_{MC}(k)$ and $Bin(k)$ across entire collection area, using the following equation:

$$I_{MC}(0 \leftrightarrow \text{b}) = \sum_{k=1}^{N} R_{MC}(k) \cdot [\pi\rho_{k+1}^2 - \pi\rho_k^2] \tag{IV-30}$$

Our monte-carlo simulation plan finally generates the total diffuse reflectance in a total amount of 4368 sceneries, which consists of 7 values of d_{area} form [50, 100, 200, 400, 600, 800, 1000]μm by 26 values of μ_s' from [0.01, 0.03, 0.05, 0.07, 0.09, 0.1, 0.3, 0.5, 0.7, 0.9, 1.0, 3.0, 5.0, 7.0, 9.0, 10. 30, 50, 70, 90, 100, 300, 500, 700, 900, 1000]mm^{-1} by 6 values of g from [0.5, 0.6, 0.7, 0.8, 0.9, 0.95] by 4 values of μ_a from [0.001, 0.01, 0.1, 1.0]mm^{-1}. Other parameters are kept the same across all simulations, including refraction index of tissue n_{tiss}=1.4, thickness of tissue layer d = 100mm, and stepsize $\Delta\rho = 1\mu m$. Per each simulation, one million photons are launched in order to yield statistically robust spatially resolved results with standard deviation controlled within 5%.

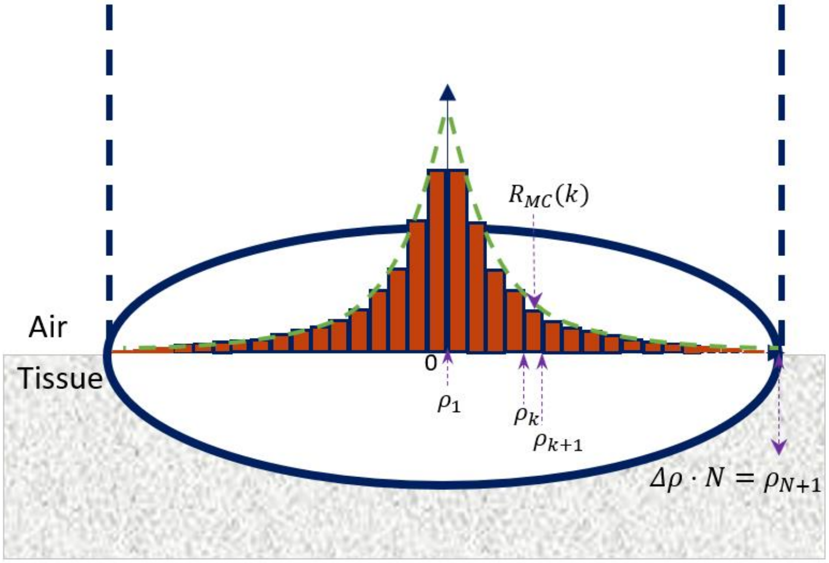

Figure IV-4 The total diffuse reflectance is calculated using MC simulation of the spatially resolved diffuse reflectance over the entire area of the tissue-air interface.

4.3.2 Phantom experiment

To test the model's effectiveness in solving reverse problem in the context of realistic AIACR geometry, a pilot phantom experiment was set up as shown in Figure IV-5, where accurately measuring temporal change of oxygen saturation level is the task of concern. The experiment was conducted by our collaborator Linhui Yu in University of Calgary, Canada, and the data were shared and processed by both.

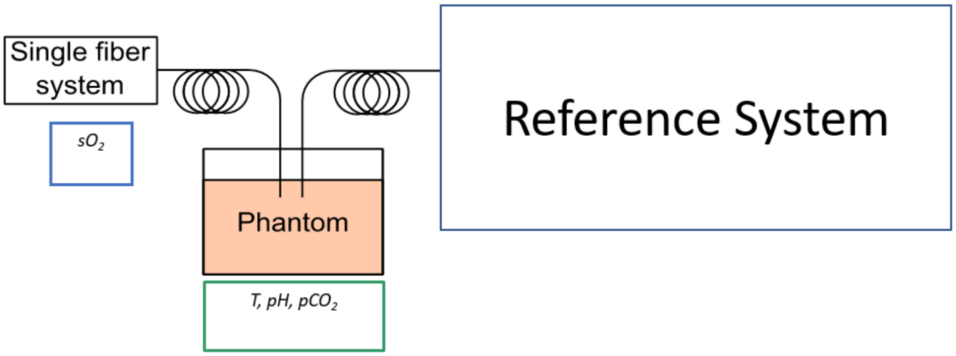

Figure IV-5 Set up of phantom experiment for model evaluation in inverse problem solving

The phantom, made from 57 mL of 1x phosphate-buffered saline (PBS), 3 mL of 20% intralipid, and 1.2 mL of rat whole blood finally have ~1% intralipid concentration, ~2% blood volume fraction, and total hemoglobin concentration of 13.8 g/dL. The phantom was kept in an airtight box with the controlled gas environment. A stirring hotplate kept the phantom homogenous. At the beginning, the airtight box was gassed with 100% oxygen until the blood was fully oxygenated, then the measurements began, and pure nitrogen was gassed into the box to deoxygenate the phantom. Two devices were used at the same time to measure the temporal change of oxygen saturation level: one is the single-fiber reflectance spectroscopy that was detailed in [4, 10], and the other, used as reference system here, is also a broadband near-infrared spectroscopy but using "the second differential method" to quantify deoxyhemoglobin then obtain oxygen-saturation[96].

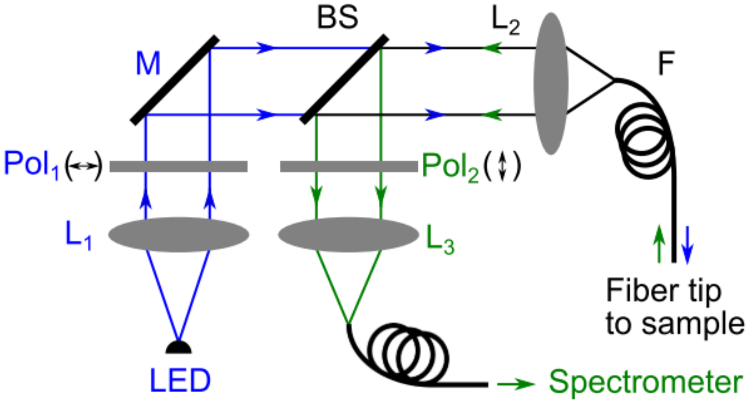

Figure IV-6 Schematic of SfRS system used in phantom experiment [10] consisting of light emitting diode (LED), collimating lens(L_1), beam splitter (BS), focusing lenses(L_2, L_3), fiber (F), polarizers (Pol_1, Pol_2) and spectrometer (S)

The schematic of SfRS is illustrated in Figure IV-6. It measured the spectrally resolved total diffuse reflectance via a $200\mu m$ single solid optical fiber with NA of 0.39 from a completely over-lapping AIACR geometry, and then the data was fitted to both our model developed in this work and another existing empirical model developed by Kanick [2, 18-20, 32, 34, 35, 39] in the procedure detailed in [10]. The existing empirical model is reproduced as below:

$$
\begin{aligned}
R_{SfRS}(\mu_a, \mu_s') &= R_{scat}(\mu_s') \exp(-\mu_a \langle L(\mu_a, \mu_s') \rangle) \\
&= \eta_{lim}\left[1 + p_1 \cdot exp(-p_2 \mu_s' \, d_{fib})\right] \left[\frac{(\mu_s' \, d_{fib})^{p_3}}{p_2 + (\mu_s' \, d_{fib})^{p_3}}\right] \\
& exp\left(-\mu_a \frac{1.54 C_{PF} \, d_{fib}}{(\mu_s' \, d_{fib})^{0.18}[\, p_6 + (\mu_a \, d_{fib})^{0.64}]}\right) \qquad \text{(IV-31)}
\end{aligned}
$$

While $[p_1, \, p_2, \, p_3, \, C_{PF}]$ as γ-specific parameter set $[0.63\gamma^2, 2.31\gamma^2, 0.57\gamma, 0.68\gamma^{0.6}]$ and γ is a phase-function dependent parameter.

For reference system, NIR attenuation spectra (716.53–983.86nm) were measured using a custom built bNIRS system, including a broadband light source (model 77501, Oriel Instruments Inc., USA), a chargecoupled device (CCD) camera (DU420-BR-DD, Andor Technology Inc., Northern Ireland), an imaging spectrograph (Shamrock 303i, Andor Technology Inc., Northern Ireland), two 30 ft long multiple single core silica optic fibers (Techen, USA) and a data processor (Optix280, Dell, USA). Data were read from the CCD chip with 56 vertically binned pixels. Data collection and analysis were performed with custom software that integrated the hardware components and determined the absolute concentration of HHb using the second differential spectrum method. ASavitzky-Golay smoothing and differentiation program (SAVGOL) was used to calculate the second derivative spectrum from the filtered spectral data. Water content was assumed to be 80% for the adult rat brain. The data acquired by the reference system was process by using the second differential method detailed in [96].

4.4 Results

The results of forward model evaluation with monte-carlo simulated data are presented in section 4.4.1 to section 4.4.3, and results of reverse problem solving with phantom experimental data are presented in section 4.4.4. During forward model evaluation, 7 sets of total diffuse reflectance corresponding to 7 different sizes of d_{area} were calculated, with each set containing 624 combinations of tissue optical properties within the 3-d parameter space $[26\mu_s' \times 4\mu_a \times 6g]$. In section 4.4.1, we evaluate the model on the cross-section with typical anisotropy value of biological tissue $[26\mu_s' \times 4\mu_a \times (g = 0.9)]$, and in section 4.4.2, we evaluate the model on the cross-section with typical absorption value $[26\mu_s' \times (\mu_a = 0.01mm^{-1}) \times 6g]$. In section 4.4.3, we present an overall model evaluation on entire 3-d parameter space $26\mu_s' \times 4\mu_a \times 6g$ for 7 different sizes of collection area. As mentioned before, with the existence of absorption in medium, though at the same value of $\mu_s' d_{area}$, total diffuse reflectance is different for different combinations of μ_s' and d_{area} within the product, therefore we choose to plot total diffuse reflectance collected via different $\mathrm{d}_{\mathrm{area}}$ against μ_s' instead of $\mu_s' d_{area}$ in forward model evaluation, to provide better sense in practice to judge under which range of tissue optical parameters and using which size of collection fiber our model will perform well.

It is necessary to point out that the total diffuse reflectance predicted by monte-carlo simulation and our model both manifests three visible patterns that are anticipated from intuitive physics understanding, as presented in Figure IV-7 with $\mathrm{d}_{\mathrm{area}} = 400\mu m$ as an example. These three patterns are: 1). Total diffuse reflectance increases as the scattering goes high, and tends to saturate when scattering becomes strong enough. 2). Stronger absorption results in smaller total diffuse reflectance and also slower speed of saturation. 3) A g-sensitive pattern, smaller g leading to bigger total diffuse reflectance, appears at lower scattering region. In Part II, we will provide analytical understanding to above three observed patterns based on the model developed in this work.

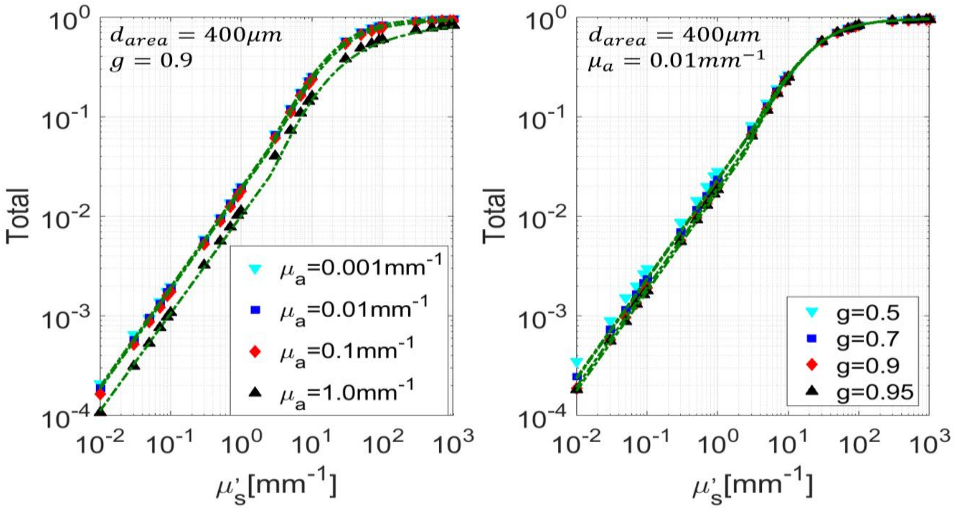

Figure IV-7 Patterns manifested both by our model and monte-carlo simulate data

4.4.1 Forward model evaluation with MC simulated data on: d_{area}=[50-1000]μm, μ_a =[0.01-1.0]mm^{-1}, μ_s'=[0.01-1000]mm^{-1}, g=0.9

To clearly display the results, we select 4 cases of collection area d_{area} =[50, 200, 600, 1000]μm to give a visual comparison between model-predicted total diffuse reflectance and monte-carlo simulated results, as shown in part A-D in Fig.7. In part E, average error percent and standard deviation are calculated for all 7 cases of collection area d_{area} =[50, 100, 200, 400, 600, 800, 1000]μm to give a quantitative report on forward model evaluation at the cross-section with typical anisotropy value g=0.9. Average error and standard deviation for 7 cases of d_{area}= [50, 100, 200, 400, 600, 800, 1000] μm: -3.8%±7.6%, -4.0%±6.6%, -2.6%±5.4%, -1.6%±4.6%, -1.7%±4.9%, -2.2%±5.9%, -3.0%±7.2%, respectively. Over the range of μ_s' that spans 5 decades from 0.01mm^{-1} until 1000 mm^{-1}, it is observed that our model closely matches monte-carlo results even when absorption reaches as high as 1mm^{-1}. The average error of all 7 cases of d_{area} ranges from the minimum -1.6% in $d_{area} = 400\mu m$ to the maximum -4.0% in $d_{area} = 100\mu m$ case, while standard deviation ranges from the minimum 4.6% in $d_{area} = 400\mu m$ case to the maximum 7.5% in $d_{area} = 50\mu m$ case. Generally, the model's deviation from monte-carlo results are less than ±10% as bounded by two red-dashed lines in part E.

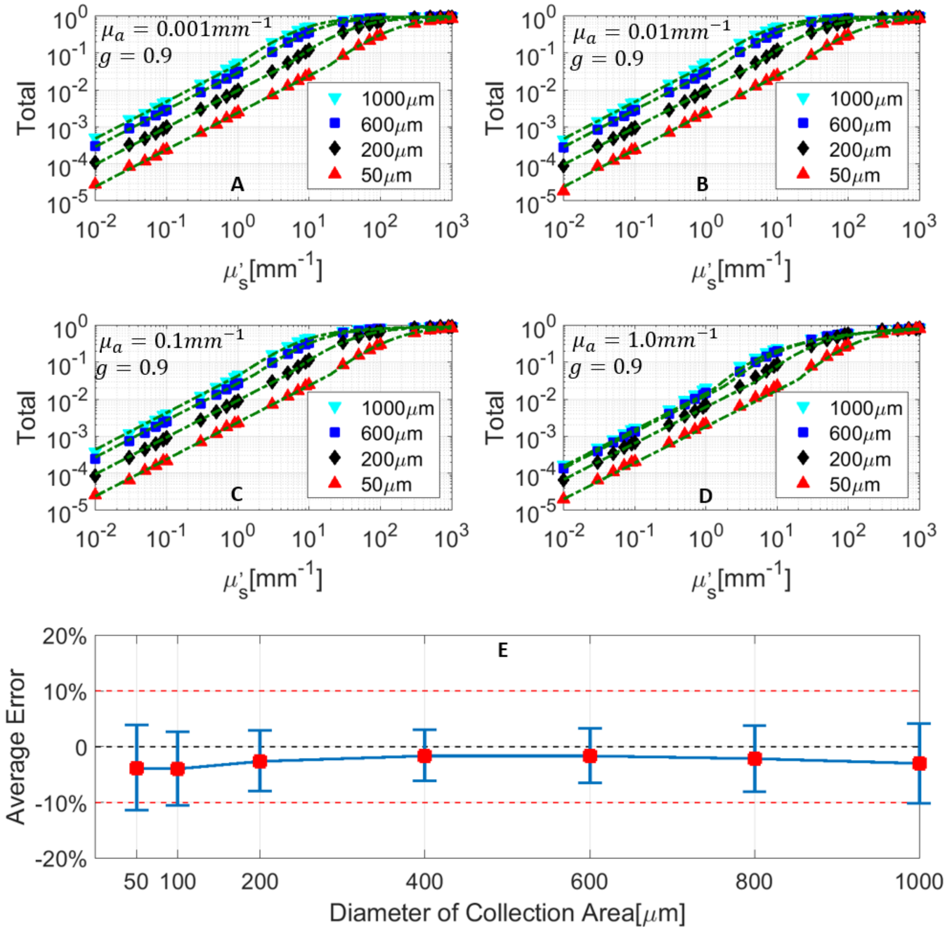

Figure IV-8 (A-D) the green dashed line represents model-predicted total diffuse reflectance and the solid discrete markers represent MC results. (E) average error and standard deviation.

4.4.2 Forward model evaluation with monte-carlo simulated data: d_{area} =[50-1000]μm, g = [0.5-0.95], μ_s' =[0.01-1000] mm^{-1}, μ_a =0.01 mm^{-1}

Similar to above, part A-D in present a visual comparison between model-predicted total diffuse reflectance and monte-carlo simulated results against μ_s' in the range of $[0.01 - 1000]\mathrm{mm}^{-1}$. With the typical absorption level $\mu_a = 0.01mm^{-1}$, each part among the four picks an anisotropy value from [0.5, 0.7, 0.9, 0.95] respectively. The data with g=0.6 and g=0.8 show the same pattern and are not presented in this section for the conciseness of entire figure. Part E presents the average error percent and standard deviation for all 7 cases of collection area $\mathrm{d}_{\mathrm{area}}$ simulated. average error and standard deviation for 7 cases of d_{area}= [50, 100, 200, 400, 600, 800, 1000] μm: -4.0%$\pm$9.6%, -4.0%$\pm$7.9%, -3.4%$\pm$6.8%, -2.6%$\pm$5.9%, -2.5%$\pm$5.7%, -2.5%$\pm$5.6%, -2.7%$\pm$5.6%. As observed from part A-D, the modeled total diffuse reflectance matches with monte-carlo results well, with a slight deviation appearing at g=0.5, $\mathrm{d_{area}} = 50\mu\mathrm{m}$, and μ_s' as low as $0.01\,\mathrm{mm}^{-1}$. The average error for each $\mathrm{d_{area}}$ is calculated from 156 sceneries on the cross-section $[26\mu_s' \times 6g \times (\mu_a = 0.01mm^{-1})]$, and falls into the range of [-4.0%, -2.5%] among 7 different d_{area}, while the standard deviation varies from 5.6% to 9.6%. From the error plot E, it is found that the case of smaller size of d_{area}, such as $50\mu m$ and $100\mu m$, brings relatively bigger average error and standard deviation, which is mainly attributed to the deviation observed at g=0.5 and low scattering region. But it is still an excellent match between our model and monte-carlo.

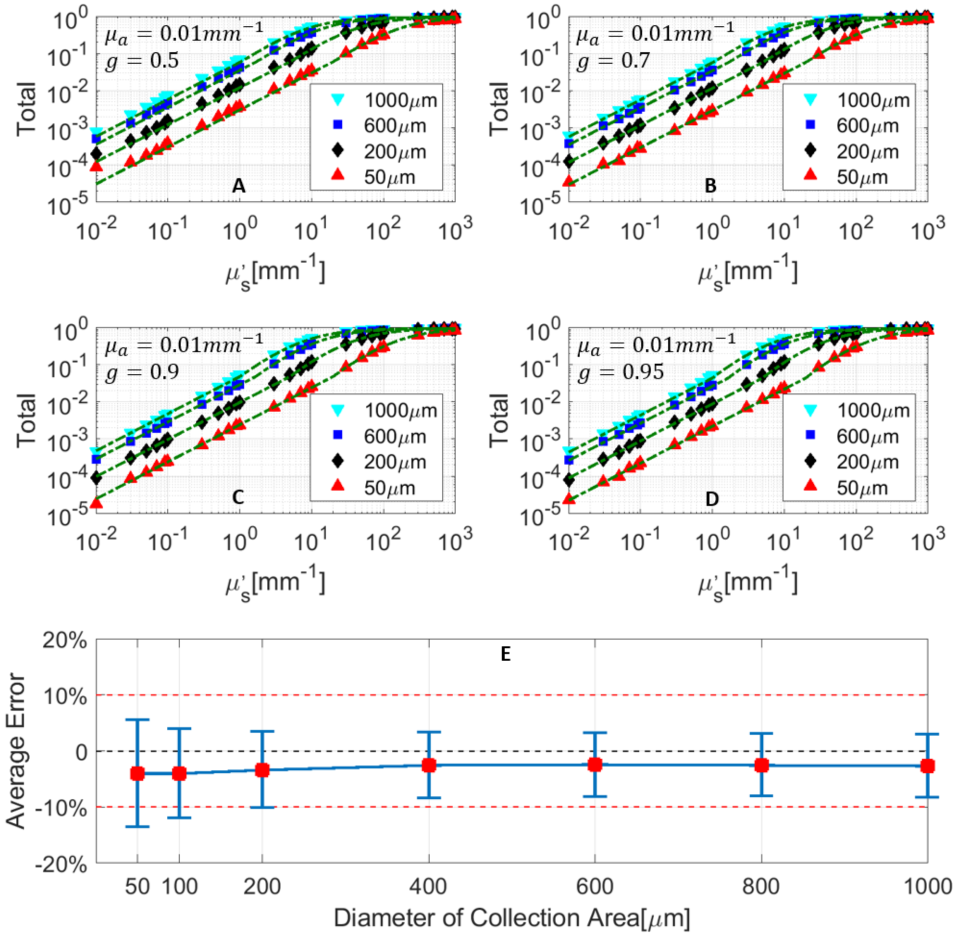

Figure IV-9 (A-D) the green dashed line represents model-predicted total diffuse reflectance and the solid discrete markers represent MC results. (E) average error and standard deviation

4.4.3 Forward model evaluation with MC simulated data of entire 3-D tissue parameter space

As shown in Figure IV-10, the model predicted total diffuse reflectance is compared against MC results of entire 3-dimension tissue parameter space, which consists of a total of 4368 sceneries from following ranges: $\mu_a = [0.001 - 1.0]mm^{-1}$, g = [0.5-0.95], $\mu_s' = [0.01 - 1000]mm^{-1}$ and $d_{area} = [50\mu m - 1000\mu m]$. Considering the typical anisotropy g is ~0.9 for biological tissue [1], we further divide the 3-D tissue parameter space $[6g \times 4\mu_a \times 26\mu_s']$ into two halves: Part A with three lower g = [0.5, 0.6, 0.7], and Part B with three higher g = [0.8, 0.9, 0.95] which covers the biological range of g well. From Part A, it is observed that less deviation appears when total diffuse reflectance is higher than 3×10^{-2} or lower than 3×10^{-4}, and more deviation appears when total diffuse reflectance is in the middle range between [$3 \times 10^{-4}, 3\times 10^{-2}$]. The deviation shown in middle range, mainly comes from the cases of using larger size of collection area d_{area} such as $800\mu m$ and $1000\mu m$. The higher range of total diffuse reflectance corresponds to stronger scattering and weaker absorption, and lower range corresponds to weaker scattering and stronger absorption. From Part B where the biologically relevant g range is concerned, an excellent match between our model and MC data shows up for whole ranges of total diffuse reflectance from the lowest 1×10^{-5} to the highest 10^{0}. Since this work intends to be applied in biomedical context, we present the statistics report of how well the model matches with MC data for g = [0.8 – 0.95]. As shown in Part C, the mean error and standard deviation for 7 sizes of collection area is -4.2%± 10.2%, -4.4%± 9.3%, -3.5%± 9.2%, -2.5%± 10.9%, -2.4%± 13.3%, -2.8%± 15.5%, -3.4%± 17.4%, respectively. The mean errors are distributed within [-4.4%, 2.4%] for all 7 cases, while the standard deviation ranges from 9.2% from $d_{area} = 200\mu m$ to 17.4% from $d_{area} = 1000\mu m$, which indicates that in the range of g = [0.8 – 0.95] lager d_{area} brings more deviations than smaller d_{area}. But with the mean error percent less than 5% and the maximum standard deviation less than 18%, our model matches MC data reasonably well in the tissue parameters space ranging in g = [0.8-0.95], $\mu_a = [0.001 - 1.0]mm^{-1}$ and $\mu_s' = [0.01 - 1000]mm^{-1}$, especially for smaller size of d_{area}.

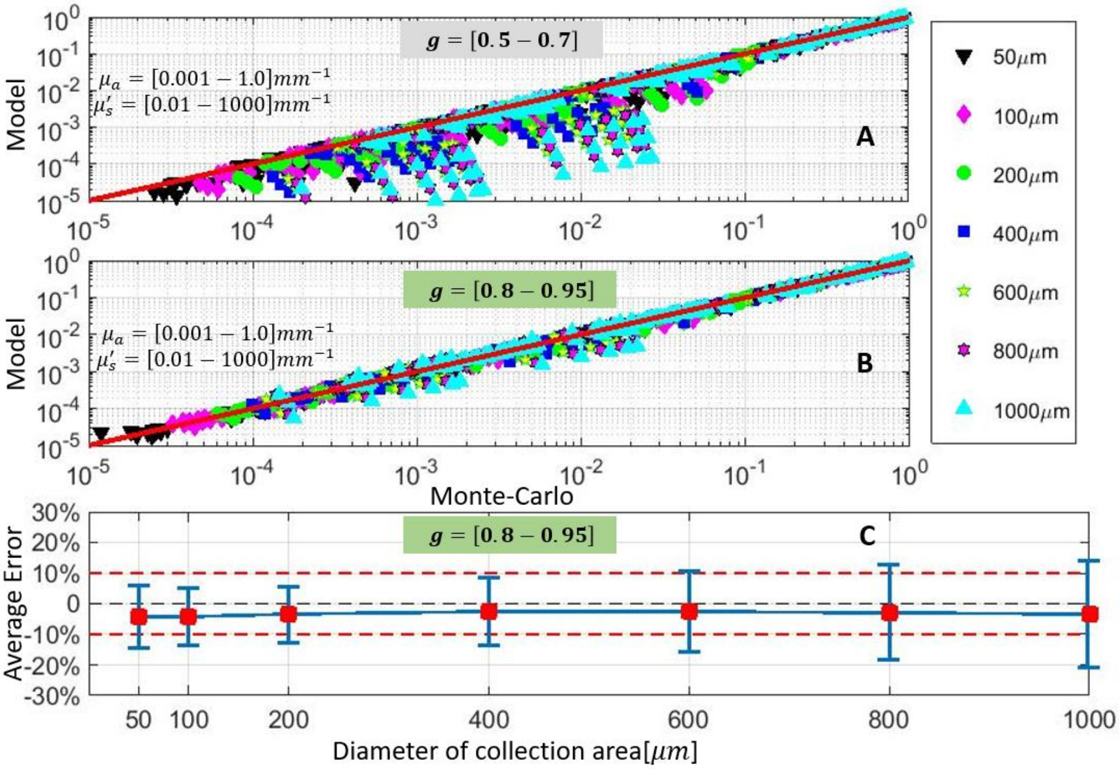

Figure IV-10 Overall forward model evaluation with MC data on three-dimension tissue parameter space

4.4.4 Inverse problem solving for oxygen-saturation level retrieval in phantom experiment with AIAC geometry

As shown in Figure IV-11 part A, total diffuse reflectance collected by the 200μm optical fiber with NA of 0.39 is modeled by both by our model developed by integration approach based on center-illuminated geometry and existing model empirically developed from an area-illuminated geometry. We could see that as scattering increases, both models predict increased total diffuse reflectance and the same saturation stage as scattering in tissue grows strong, but when scattering is not stronger than 10 mm^{-1}, the two models show different level of total diffuse reflectance since the two model are based on different geometries.

The part B presents the oxygen-saturation level measured by reference system, extracted by using our model and existing empirical model. Among them, the original reference data shown by red circles, was smoothed by sliding window method in Matlab in order to suppress the noise. The SO_2 extracted from data fitting with both model shows the correct changing trend as measured by reference system, but also presents the following differences: 1) SO_2 fitted by using existing empirical model shows an under-estimation at higher range and tends to match better when SO_2 decreases, but produces a negative value when SO_2 drops to close to zero. 2) SO_2 fitted by using our model tends to match better at higher range and over-estimates when SO_2 drops down, but returns a positive number larger than zero when it drops to close to zero.

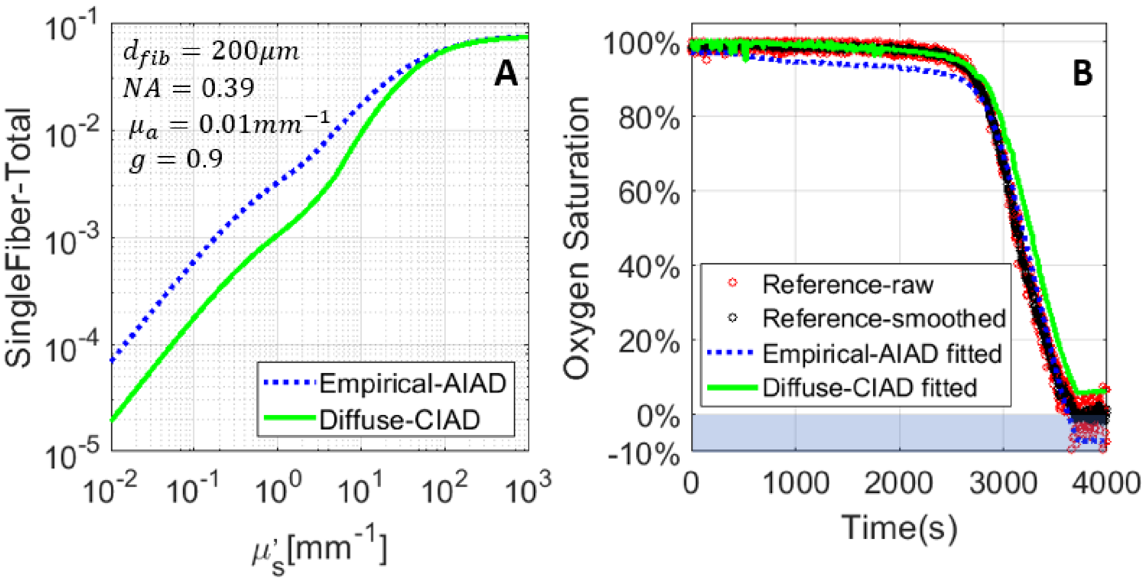

Figure IV-11 (A) Comparison of total diffuse reflectance modeled with two different approaches. (B) Temporal change of oxygen-saturation level measured by reference system and SfRS system by data fitting with two different models.

4.5 Discussions

4.5.1 Forward model evaluation

The statistics report of forward model evaluation in 4368 sceneries detailed in previous section demonstrates that our model accurately predicts the total diffuse reflectance collected via 7 different sizes of d_{area} and from a broad range of tissue optical properties intended for the context of biomedical applications. This validates our modeling methodology introduced in this work, including the construction of spatially resolved diffuse reflectance model by concatenating an inner-field model and an outer-field model as detailed in section 4.2.1, the integration approach to obtain the total diffuse reflectance as detailed in section 4.2.2, and the adaptation technique to broaden model's effective range to any arbitrary μ_s' values as detailed in section 4.2.3.

The concatenation strategy used in constructing spatial diffuse reflectance model, evades the difficulty of building a single analytical model that works from diffuse range down to sub-diffuse range close to point of entry which is particularly crucial for modeling single fiber collected total diffuse reflectance. In addition, a scattering-dependent border point $\rho_{border} = \delta/\mu_s'$ that sepeartes inner field and outer field, coordinates two models to complement each other closely to address various tissue scattering conditions. The number δ is set as 0.5 in this work, but in fact we intentionally make an overlapping between the working ranges of inner-field model and outer field model. This allows a spare adjustment range for δ value, and it could even include the effect of μ_a when needed, which provides our model with additional flexibility to resolve even complex tissue conditions.

However, the concatenation design of our spatial model also brings an expected side effect: the discontinuity at border point $\rho_{border} = \delta/\mu_s'$. After integration, this discontinuity will propagate into the integral model of total diffuse reflectance. Taking $d_{area} = 200\mu m$ for instance, when reduced scattering μ_s' is less than $5mm^{-1}$, the border point $\rho_{border} \geq 100\mu m$ and the collected total diffuse reflectance will be solely dominated by inner-field model; when reduced scattering μ_s' is larger than $5mm^{-1}$, the border point $\rho_{border} \leq 100\mu m$, then the collected total diffuse reflectance is determined by both inner-field model and outer-field model. Thus, each size of d_{area} corresponds to one threshold reduced scattering $[\mu_s']_{thres}$, where total diffuse reflectance when plotted against μ_s' will possess inevitable discontinuity. A lot of efforts were invested on minimizing this discontinuity as much as possible while taking full advantages of the convenience brought by our concatenation design, since the extent of its existence will affect the forward modeling accuracy in comparison with MC results. Finally it is only slightly visible if observing part A-D in Figure IV-8 and Figure IV-9 carefully, but the deviation appearing in the middle range of total diffuse reflectance as shown in part A of Figure IV-10 may indicate that this inevitable discontinuity may become worse under certain conditions such as probing tissue of lower anisotropy g with larger size of d_{area}. The absolute value of average error percent is less than 5% compared to MC data, and all show negative, which means that our model slightly under-estimate total diffuse reflectance generally. This may result from different reasons, including the discontinuity mentioned above, the inaccuracy of our models as well as the error introduced by adaptation technique, et.al.

The adaptation technique, inspired by scattering-only case where the total diffuse reflectance is only dependent on the dimensionless term $\mu_s' d_{area}$ regardless of the combinations within, is designed to broaden our integral model's effective working range to any arbitrary μ_s' values from the case $\mu_s' = 1mm^{-1}$ where the initial inner-field model was developed. It turns out to work well in absorption-present cases with arbitrary μ_s' values even when μ_a reaches as high as $1\ mm^{-1}$, as shown in Figure IV-10. This novel technique successfully addresses the conflict between the practical need of applying the model to probe tissue with various optical properties including μ_s', and the realistic difficulty of empirically developing a spatial inner-field model through calibration with equal amount of MC simulated data. Conversion method; inner-field, not outer-field does not need. The spatial inner-field model, though empirically calibrated with MC data, were inspired and guided by the solid angler approaches illustrated in Appendix 2. Compared with analytical model we developed in Chap IV, the structure of semi-empirically developed spatial inner-field model in this work, provides more simplicity and flexibility, and more importantly the inherent ability of being integrated to reach total diffuse reflectance, thus was finally adopted as inner-field model in this work.

4.5.2 Inverse problem solving in experiment setup with AIAC geometry

The model in this work was developed specific to a center-illumination and area-collection (CIAC) geometry, yet it reveals similar pattern as the total diffuse reflectance collected with area-illumination and area collection geometry, including the saturation plateau, scattering-sensitive region, and anisotropy-sensitive region, as shown in Figure IV-7 and Figure IV-11. As stated before, the experiment setup of single-fiber reflectance spectroscopy involves a complete overlapping area-illumination and area-collection geometry, however the data fitting with our model correctly predicts the temporal change of SO_2 over a large span from 100% down to 0%. Particularly when SO_2 level is larger than 90%, which is the biological range in medical application, results from our model displays an excellent match with the reference, while the exiting empirical model displays a noticeable under-estimation. This indicates that considering the difficulty of analytically deriving a model from AIAC geometry, our model developed from CIAC geometry could be used as a good approximation in practice for inverse problem solving. Nevertheless, the geometry difference does exist and reflects itself displays a slight over-estimation when SO_2 drops below 90% compared to the reference. Interesting things happened when SO_2 finally dropped to 0%, our model returns a positive SO_2 value about 5%, while the existing empirical model returns a negative SO_2 value about -8%, with data-fitting performed by using the same Matlab function lsqcurvefit (), same boundary parameter setting. Beyond the physiological range, the negative SO_2 value extracted from data-fitting with existing empirical model, was also reported in an earlier publications [10] published by Linhui Yu in 2016, and that is what motived the author to collaborate with us in the seeking for a more robust model for tissue optical parameter retrieval.

4.6 Summary

In conclusion, this work developed a model of total diffuse reflectance collected from a center-illumination and area-collection geometry by integrating a spatial diffuse reflectance model constructed by concatenating two models for diffusive and sub-diffusive region. The comparison with a large amount of MC tissue probing sceneries displays excellent forward modeling accuracy over a broad range of $\mu_a = [0.001 - 1.0]mm^{-1}$, g = [0.8-0.95], $\mu_s' = [0.01 - 1000]mm^{-1}$ with average error less than 5% for 7 d_{area} in the range of and $[50\mu m - 1000\mu m$, which validates our modeling methodology of concatenation strategy, integration approach and adaptation technique. The phantom experiment set up for inverse problem solving in a different geometry of overlapping area-illumination and area-collection, indicates the potential of applying our model to single-fiber reflectance spectroscopy for more robust retrieving tissue optical parameters.

CHAPTER V

MODEL-BASED PROFILING OF CHARACTERISTICS OF STEADY-STATE SFRS

5.1 Introduction

In the field of steady-state single-fiber diffuse reflectance spectroscopy, Kanick's model [2, 18-20, 32, 34, 35, 39] that was developed by empirically fitting with MC simulated results and phantom experiment data associated with an area-illumination and area-collection (AIAC) geometry, has powered many clinical applications of tissue probing. Kanick's model also manifested the following characteristics of steady-state SfRS measurements as shown in Figure V-1 and illustrated below: (1) A saturation zone wherein the diffuse reflectance reaches a plateau as the dimensionless reduced scattering coefficient scaled to the fiber-diameter $\mu_s' d_{fib}$escalates to ~100. The total diffuse reflectance is close to 100% before scaled down $\eta_{lim} = 2.47\%$ which is the light collection efficiency at high-scattering end due to numerical aperture of a realistic fiber. In this saturation zone, total diffuse reflectance is insensitive to scattering change. The existence of absorption does not affect the saturation level. (2) A diffusion zone wherein the diffuse reflectance increases as the reduced scattering coefficient increases but remains insensitive to the anisotropy factor. The transition between the scattering-sensitive diffusion zone and scattering-insensitive saturation zone is observed to appear approximately at $\mu_s' d_{fib} = \sim 10$ when tissue absorption is zero or very small. The increase of absorption tends to postpone the transition to happen at larger $\mu_s' d_{fib}$ values, as shown in Part C. (3) A g-sensitive zone when scattering is weak, the total diffuse reflectance not only increases as the reduced scattering coefficient increase, but also sensitive to anisotropy factor g. At same μ_s', the smaller g that corresponding to stronger backward scattering, yields out larger diffuse reflectance.

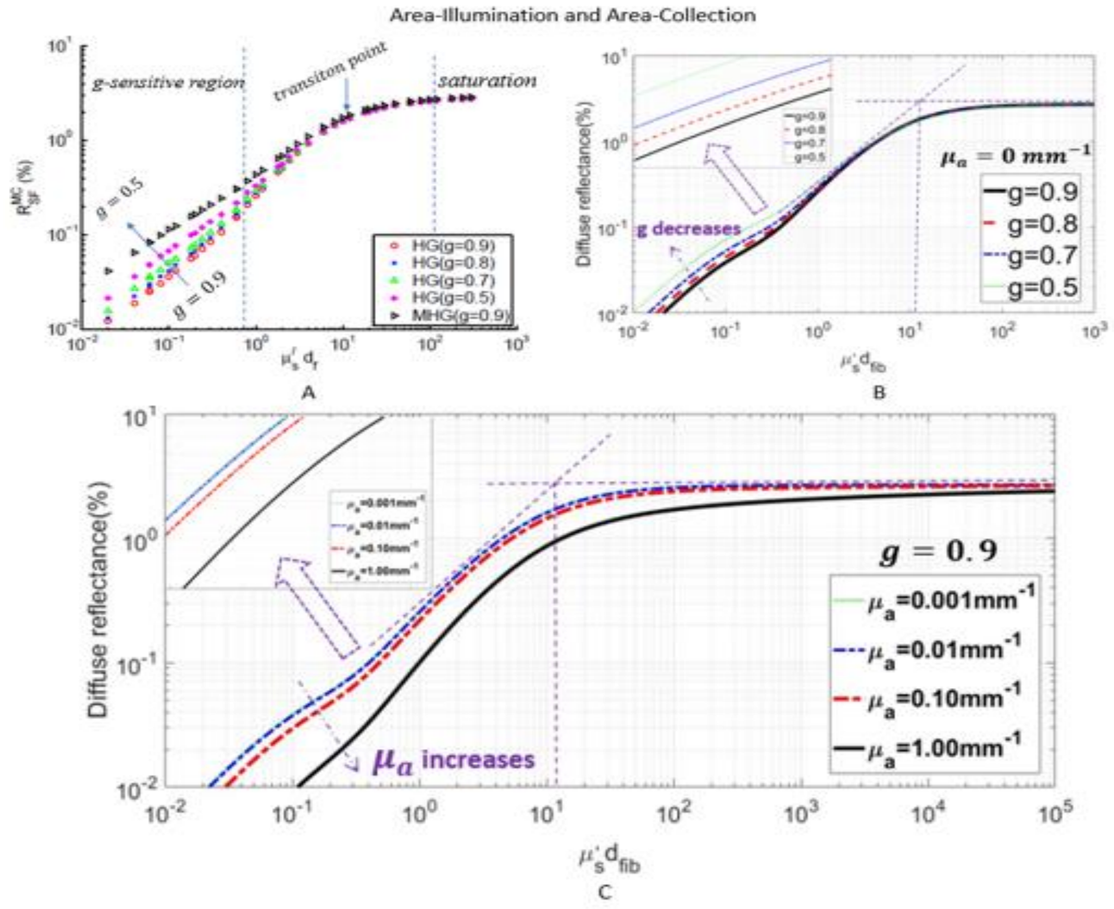

Figure V-1 Characteristics of SfRS manifested by Kanick's model. A). Kanick's MC simulated total diffuse reflectance collected form absorption-free medium [18, 19]. B) Kanick's model-predicted total diffuse reflectance from absorption-free medium corresponding to part A. C) Kanick's model-predicted total diffuse reflectance from medium with absorption.

The chapter IV in this work has demonstrated a model of total diffuse reflectance associated with a center-illumination and area-collection (CIAC) round geometry that was validated by large amount of MC simulated results generated from same CIAC geometry and further tested in reverse problem solving with

SfRS configuration. Interestingly, despite the geometry difference, our MC data and our model without considering numerical aperture, also presents the same characteristics as summarized before, as shown in following figure.

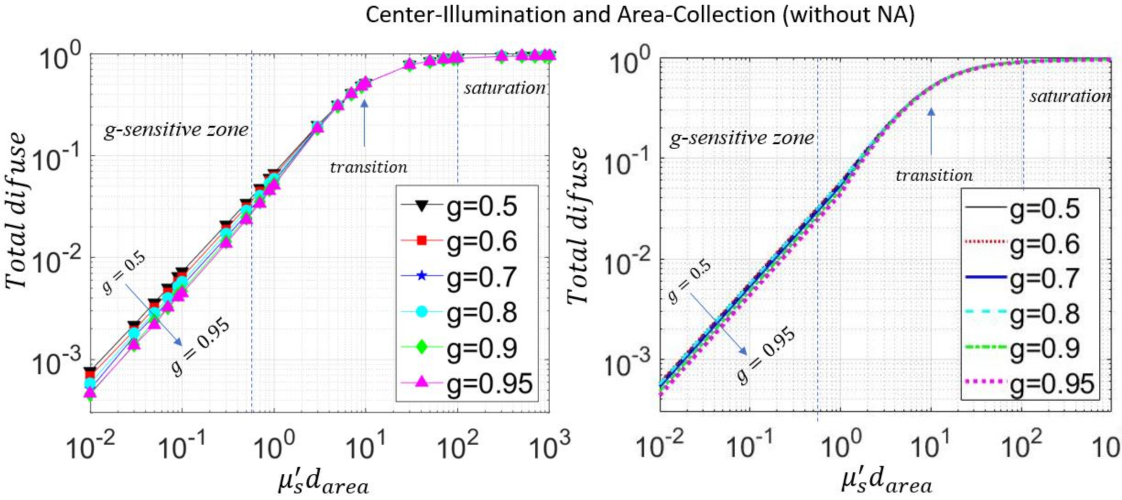

Figure V-2 Characteristics presented by our MC data and model associated with center-illumination and area-collection geometry, without including scaling effect of numerical aperture.

The effect of numerical aperture of a realistic fiber, when approximated in the first order, could be considered as an overall scaling ratio of $\eta_{lim} = \left(\frac{NA}{n_{tiss}}\right)^2$, or empirically formularized as $\eta_c = \eta_{lim}[1 + 1.55\exp(-6.82\mu_s' d_{fiber})]$ according to Kanick's monte-carlo simulation study[2]. In this work, we adopt the later η_c formula to account for effect of numerical aperture, the same formula used by Kanick's model. The Figure below presents how light collection efficiency changes with reduced scattering coefficient, based on an optical fiber with NA = 0.22 and core diameter d_f=1mm, tissue refraction index n_{tiss}=1.4. We see that at high-scattering end, η_c reduces to $\eta_{lim} = 2.47\%$, but at low scattering region, it can reach 2-3 folds of η_{lim}.

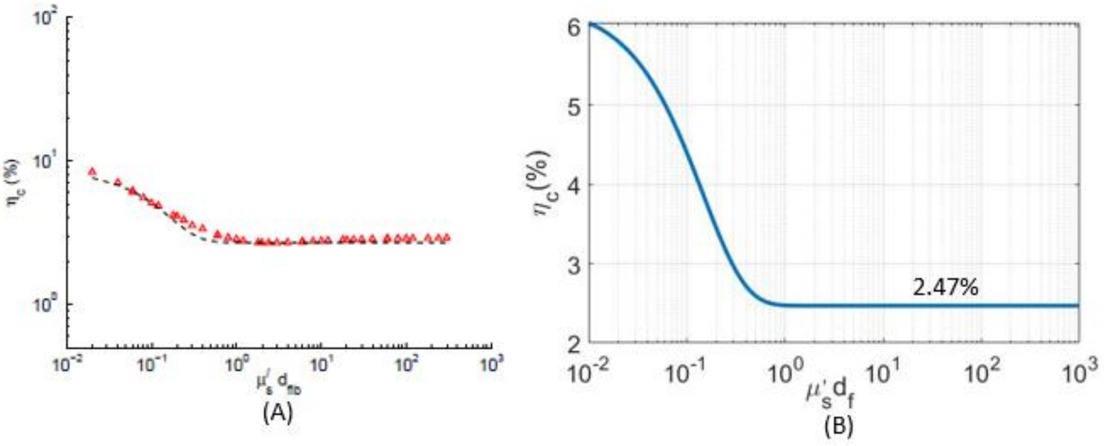

Figure V-3 The empirical formula of light collection efficiency A) the red marker is Kanick's MC simulated result [2]and black dashed line is the empirical formula developed by fitting with MC data. B) A reproduced result of collection efficiency formula in left part but displayed in linear scale to better visualization of its change with scattering.

Then scaling the data presented in Figure V-2 by η_c will yield out the total diffuse reflectance of SfRS measurement as shown in Figure V-4. As observed from this figure, the three characteristics including saturation zone, diffusion zone, and g-sensitive zone, remain after adding the effect of numerical aperture in our model. The only difference is that in low-scattering range, the total diffuse reflectance is lifted up a little bit by a relatively higher value of η_c than high-scattering region, which is consistent with Kanick's study shown in Figure V-1.

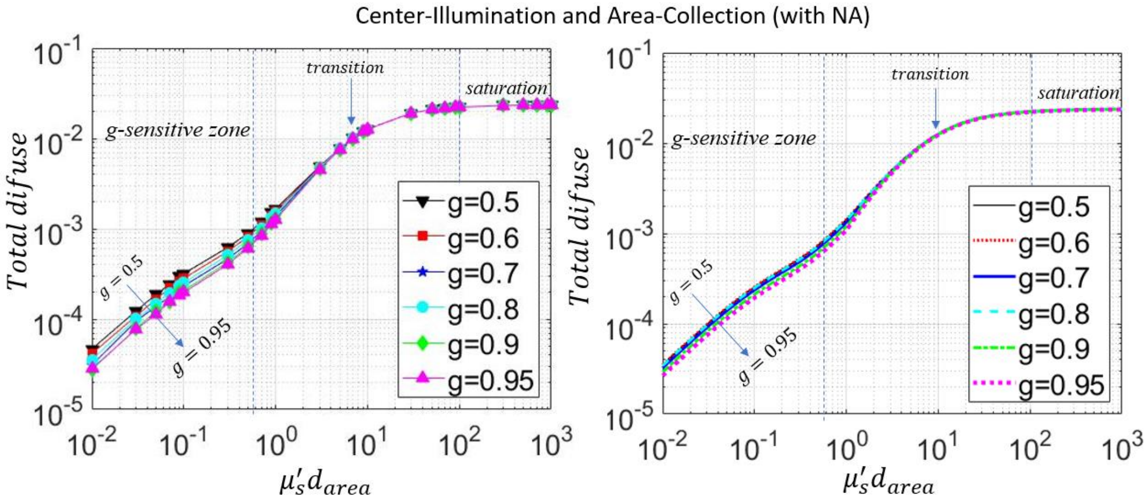

Figure V-4 Characteristics presented by our MC data and model associated with center-illumination and area-collection geometry, after including scaling effect of numerical aperture.

However, those three characteristics observed in steady-state SfRS measurements is still insufficiently understood, due to lack of analytical model with physics insight. Analytically driven understanding of the global characteristic patterns of the SfRS measurement will be fundamentally important in designing the clinical applications with SfRS, such as providing guidance to the choice of optical fiber to better quantify the scattering change in tissue, and offering the potential to assess the anisotropy change in tissue by employing the g-sensitive zone in SfRS measurement. In this work, we will use the model developed in Chapter IV to provide a model-based profiling to above three steady-state SfRS patterns.

5.2 Theory

5.2.1 A summary of our total diffuse reflectance model

We use same notions in this chapter as used in Chapter IV, such as b = $d_{area}/2$, $z_a = 1/\mu_s'$, et. al.

If $b = \xi z_a \leq \delta z_a$, total diffuse reflectance is solely determined by inner-field model as represented in Eq. (V-1)

$$I_{0\leftrightarrow\xi \mathrm{z_a}} = 0.75^{g} 10^{-(1+p_1\gamma)}(1-g)^{g}\exp(-\gamma)\frac{1}{1-p_2\gamma}\left(\frac{\xi}{1-g}\right)^{1-p_2\gamma} \quad \text{(V-1)}$$

If $b = \xi \mathrm{z_a} > \delta z_a$, total diffuse reflectance is determined by both inner-field model an outer-field model as represented in Eq. (V-2):

$$I_{0\leftrightarrow\xi \mathrm{z_a}}(\mathrm{d_{area}}, \mu_s', \mu_a, \mathrm{g}) = I_{0\leftrightarrow\delta \mathrm{z_a}} + \left[I^{\Psi}_{\delta z_a\leftrightarrow\infty} - I^{\Psi}_{\xi z_a\leftrightarrow\infty}\right] + \left[I^{\Psi^*}_{\delta z_a\leftrightarrow\infty} - I^{\Psi^*}_{\xi z_a\leftrightarrow\infty}\right]$$

$$+\left[I^{\mathrm{JZ}}_{\delta z_a\leftrightarrow\infty} - I^{\mathrm{JZ}}_{\xi z_a\leftrightarrow\infty}\right] + \left[I^{\mathrm{JZ}^*}_{\delta z_a\leftrightarrow\infty} - I^{\mathrm{JZ}^*}_{\xi z_a\leftrightarrow\infty}\right] \quad \text{(V-2)}$$

$$I_{0\leftrightarrow\delta \mathrm{z_a}} = 0.75^{g} 10^{-(1+p_1\gamma)}(1-g)^{g}\exp(-\gamma)\frac{1}{1-p_2\gamma}\left(\frac{\delta}{1-g}\right)^{1-p_2\gamma} \quad \text{(V-3)}$$

$$I^{\Psi}_{\delta z_a\leftrightarrow\infty} = \frac{1}{8\sqrt{2}\pi \mathrm{D}\mu_{\mathrm{eff}}}\left[\exp\left(-\mu_{\mathrm{eff}}\mathrm{z_a}\sqrt{\delta^2+1}\right) - \exp\left(-\mu_{\mathrm{eff}}\mathrm{z_a}\sqrt{\delta^2+(1+2\beta)^2}\right)\right] \quad \text{(V-4)}$$

$$I^{\Psi}_{\xi z_a\leftrightarrow\infty} = \frac{1}{8\sqrt{2}\pi \mathrm{D}\mu_{\mathrm{eff}}}\left[\exp\left(-\mu_{\mathrm{eff}}\mathrm{z_a}\sqrt{\xi^2+1}\right) - \exp\left(-\mu_{\mathrm{eff}}\mathrm{z_a}\sqrt{\xi^2+(1+2\beta)^2}\right)\right] \quad \text{(V-5)}$$

$$I^{\Psi^*}_{\delta z_a\leftrightarrow\infty} = \frac{S^*}{8\sqrt{2}\pi \mathrm{D}\mu_{\mathrm{eff}}}\left[\exp\left(-\mu_{\mathrm{eff}}\mathrm{z_a}\sqrt{\delta^2+\alpha^2}\right) - \exp\left(-\mu_{\mathrm{eff}}\mathrm{z_a}\sqrt{\delta^2+(\alpha+2\beta)^2}\right)\right] \quad \text{(V-6)}$$

$$I^{\Psi^*}_{\xi z_a\leftrightarrow\infty} = \frac{S^*}{8\sqrt{2}\pi \mathrm{D}\mu_{\mathrm{eff}}}\left[\exp\left(-\mu_{\mathrm{eff}}\mathrm{z_a}\sqrt{\xi^2+\alpha^2}\right) - \exp\left(-\mu_{\mathrm{eff}}\mathrm{z_a}\sqrt{\xi^2+(\alpha+2\beta)^2}\right)\right] \quad \text{(V-7)}$$

$$I^{\mathrm{JZ}}_{\delta z_a\leftrightarrow\infty} = \frac{3}{8\sqrt{2}\pi}\left[\frac{1}{\sqrt{\delta^2+1}}\exp\left(-\mu_{\mathrm{eff}}\mathrm{z_a}\sqrt{\delta^2+1}\right) + \frac{(1+2\beta)}{\sqrt{\delta^2+(1+2\beta)^2}}\exp\left(-\mu_{\mathrm{eff}}\mathrm{z_a}\sqrt{\delta^2+(1+2\beta)^2}\right)\right] \text{(V-8)}$$

$$I^{\mathrm{JZ}}_{\xi z_a\leftrightarrow\infty} = \frac{3}{8\sqrt{2}\pi}\left[\frac{1}{\sqrt{\xi^2+1}}\exp\left(-\mu_{\mathrm{eff}}\mathrm{z_a}\sqrt{\xi^2+1}\right) + \frac{(1+2\beta)}{\sqrt{\xi^2+(1+2\beta)^2}}\exp\left(-\mu_{\mathrm{eff}}\mathrm{z_a}\sqrt{\xi^2+(1+2\beta)^2}\right)\right] \text{(V-9)}$$

$$I^{\mathrm{JZ}^*}_{\delta z_a\leftrightarrow\infty} =$$

$$\frac{3S^*}{8\sqrt{2}\pi}\left[\frac{\alpha}{\sqrt{\delta^2+\alpha^2}}\exp\left(-\mu_{\mathrm{eff}}\mathrm{z_a}\sqrt{\delta^2+\alpha^2}\right) + \frac{(\alpha+2\beta)}{\sqrt{\delta^2+(\alpha+2\beta)^2}}\exp\left(-\mu_{\mathrm{eff}}\mathrm{z_a}\sqrt{\delta^2+(\alpha+2\beta)^2}\right)\right] \text{(V-10)}$$

$$I^{\mathrm{JZ}^*}_{\xi z_a\leftrightarrow\infty} =$$

$$\frac{3S^*}{8\sqrt{2}\pi}\left[\frac{\alpha}{\sqrt{\xi^2+\alpha^2}}\exp\left(-\mu_{\mathrm{eff}}\mathrm{z_a}\sqrt{\xi^2+\alpha^2}\right) + \frac{(\alpha+2\beta)}{\sqrt{\xi^2+(\alpha+2\beta)^2}}\exp\left(-\mu_{\mathrm{eff}}\mathrm{z_a}\sqrt{\xi^2+(\alpha+2\beta)^2}\right)\right] \text{(V-11)}$$

5.2.2 The saturation level when scattering approaches to infinite

With above algebraic form of total diffuse reflectance model $I_{0\leftrightarrow\xi\mathrm{z_a}}(\mathrm{d_{area}}, \mu_s', \mu_a, g)$, the saturation level could be analytically calculated as the limit of total diffuse reflectance when reduced scattering μ_s' approaches infinite. Since the border point $\rho_{border} = \delta\mathrm{z_a}$ will approaches zero and thus $\rho_{border} = \delta\mathrm{z_a} < b$ stands anyway, we only need consider Eq. (V-2) for limit calculation. The saturation level denoted as $\mathrm{I_{satu}}$, is contributed by five components including inner-field $I_{0\leftrightarrow\delta\mathrm{z_a}}$, master fluence rate $I^{\Psi}_{\delta\mathrm{z_a}\leftrightarrow\mathrm{b}}$, slave fluence rate $I^{\Psi^*}_{\delta\mathrm{z_a}\leftrightarrow\mathrm{b}}$, master flux z-direction part $I^{\mathrm{JZ}}_{\delta\mathrm{z_a}\leftrightarrow\mathrm{b}}$, and slave flux z-direction part $I^{\mathrm{JZ}^*}_{\delta\mathrm{z_a}\leftrightarrow\mathrm{b}}$.

$$\mathrm{I_{satu}} = \lim_{\mu_s'\to\infty} I_{0\leftrightarrow\delta\mathrm{z_a}} + \lim_{\mu_s'\to\infty} I^{\Psi}_{\delta\mathrm{z_a}\leftrightarrow\mathrm{b}} + \lim_{\mu_s'\to\infty} I^{\Psi^*}_{\delta\mathrm{z_a}\leftrightarrow\mathrm{b}} + \lim_{\mu_s'\to\infty} I^{\mathrm{JZ}}_{\delta\mathrm{z_a}\leftrightarrow\mathrm{b}} + \lim_{\mu_s'\to\infty} I^{\mathrm{JZ}^*}_{\delta\mathrm{z_a}\leftrightarrow\mathrm{b}} \qquad \text{(V-12)}$$

For inner-filed component, when $\mu_s' \to \infty$, the parameter $\gamma = 2\mu_a/\mu_s \to 0$,

$$\lim_{\mu_s'\to\infty} I_{0\leftrightarrow\delta\mathrm{z_a}} = \lim_{\gamma\to 0} 0.75^g 10^{-(1+p_1\gamma)}(1-g)^g \exp(-\gamma)\frac{1}{1-p_2\gamma}\left(\frac{\delta}{1-g}\right)^{1-p_2\gamma}$$

$$= 0.75^g 10^{-1}(1-g)^g \frac{\delta}{1-g} \qquad \text{(V-13)}$$

For a typical value g=0.9 as the following derivation is based on, the inner-field component is

$$\lim_{\mu_s'\to\infty} I_{0\leftrightarrow\delta\mathrm{z_a}} = \sim 4.86\% \qquad \text{(V-14)}$$

a) Master fluence rate component

$$\lim_{\mu_s'\to\infty} I^{\Psi}_{\delta\mathrm{z_a}\leftrightarrow\mathrm{b}} = \lim_{\mu_s'\to\infty} I^{\Psi}_{\delta\mathrm{z_a}\leftrightarrow\infty} - \lim_{\mu_s'\to\infty} I^{\Psi}_{b\leftrightarrow\infty} \qquad \text{(V-15)}$$

Calculate the first term,

$$\lim_{\mu_s'\to\infty} I^{\Psi}_{\delta\mathrm{z_a}\leftrightarrow\infty} = \lim_{\mu_s'\to\infty} \frac{1}{8\sqrt{2}\pi \mathrm{D}\mu_{\mathrm{eff}}}\left[\exp\left(-\mu_{\mathrm{eff}}\mathrm{z_a}\sqrt{\delta^2+1}\right) - \exp\left(-\mu_{\mathrm{eff}}\mathrm{z_a}\sqrt{\delta^2+(1+2\beta)^2}\right)\right] \qquad \text{(V-16)}$$

$$\lim_{\mu_s'\to\infty} I^{\Psi}_{\delta\mathrm{z_a}\leftrightarrow\infty} = \lim_{\mu_s'\to\infty} \frac{1}{8\sqrt{2}\pi}\left[\frac{exp\left(-\mu_{eff}z_a\sqrt{\delta^2+1}\right) - exp\left(-\mu_{eff}z_a\sqrt{\delta^2+(1+2\beta)^2}\right)}{D\mu_{eff}}\right] \qquad \text{(V-17)}$$

Apply $D = \frac{1}{[3(\mu_a+\mu_s')]} \to \frac{1}{3\mu_s'} = \frac{1}{3}z_a$, as $\mu_s' \to \infty$

$$\lim_{\mu_s'\to\infty} I^{\Psi}_{\delta \mathrm{z_a}\leftrightarrow\infty} = \frac{3}{8\sqrt{2}\pi}\left[\frac{exp\left(-\mu_{eff}z_a\sqrt{\delta^2+1}\right)-exp\left(-\mu_{eff}z_a\sqrt{\delta^2+(1+2\beta)^2}\right)}{\mu_{eff}z_a}\right] \tag{V-18}$$

Denote $x = \mu_{eff}z_a = \frac{\mu_{eff}}{\mu_s'} = \frac{\sqrt{3\mu_a(\mu_a+\mu_s')}}{\mu_s'} = \sqrt{\frac{3\mu_a(\mu_a+\mu_s')}{[\mu_s']^2}} \to 0$, as $\mu_s' \to \infty$

$$\lim_{\mu_s'\to\infty} I^{\Psi}_{\delta \mathrm{z_a}\leftrightarrow\infty} = \frac{3}{8\sqrt{2}\pi}\lim_{x\to 0}\frac{exp\left(-x\sqrt{\delta^2+(1+2\beta)^2}\right)-exp\left(-x\sqrt{\delta^2+1}\right)}{x}$$

$$= \frac{3}{8\sqrt{2}\pi}\left[\sqrt{\delta^2+\left(1+\frac{4A}{3}\right)^2}-\sqrt{\delta^2+1}\right] = \sim 36.78\% \tag{V-19}$$

The details of calculation above is shown in Appendix 3.

Now calculate the second term,

$$\lim_{\mu_s'\to\infty} I^{\Psi}_{b\leftrightarrow\infty} = \lim_{\mu_s'\to\infty}\frac{1}{8\sqrt{2}\pi \mathrm{D}\mu_{\mathrm{eff}}}\left[\exp\left(-\mu_{\mathrm{eff}}\mathrm{z_a}\sqrt{\xi^2+1}\right)-\exp\left(-\mu_{\mathrm{eff}}\mathrm{z_a}\sqrt{\xi^2+(1+2\beta)^2}\right)\right] \tag{V-20}$$

$$\lim_{\mu_s'\to\infty} I^{\Psi}_{b\leftrightarrow\infty} = \lim_{\mu_s'\to\infty}\frac{1}{8\sqrt{2}\pi}\left[\frac{exp\left(-\mu_{eff}\sqrt{b^2+(z_a)^2}\right)-exp\left(-\mu_{eff}\sqrt{b^2+(z_a+2z_b)^2}\right)}{D\mu_{eff}}\right] \tag{V-21}$$

Expand the two exponential terms above to Taylor series of the first two orders, and the derivation shows that the second term turns out to be zero, as detailed in appendix 4.

$$\lim_{\mu_s'\to\infty} I^{\Psi}_{b\leftrightarrow\infty} = \lim_{\mu_s'\to\infty}\frac{3}{8\sqrt{2}\pi}exp\left(-\mu_{eff}b\right)\frac{4\beta(1+\beta)}{\mu_s' d_{area}} = 0 \tag{V-22}$$

Finally, the master fluence rate component is

$$\lim_{\mu_s'\to\infty} I^{\Psi}_{\delta \mathrm{z_a}\leftrightarrow \mathrm{b}} = \sim 36.78\% \tag{V-23}$$

It matches our expectation according to physics understanding of diffuse reflectance collection from tissue. As tissue scattering increases but size of collection area is fixed as $b = d_{area}/2$, diffusely reflected photons tend to be remitted at region close to incident point and get collected within the area with $\rho = [0, b]$, while the total diffuse reflectance collected $\rho = b$ will become less and less. Then total diffuse reflectance collected from limited size of d_{area} will close to total diffuse reflectance collected from entire semi-infinite geometry.

b) Slave fluence rate component

$$\lim_{\mu_s' \to \infty} I^{\Psi^*}_{\delta z_a \leftrightarrow b} = \lim_{\mu_s' \to \infty} I^{\Psi^*}_{\delta z_a \leftrightarrow \infty} - \lim_{\mu_s' \to \infty} I^{\Psi^*}_{b \leftrightarrow \infty} \tag{V-24}$$

Calculate the first term,

$$\lim_{\mu_s' \to \infty} I^{\Psi^*}_{\delta z_a \leftrightarrow \infty} = \lim_{\mu_s' \to \infty} \frac{S^*}{8\sqrt{2}\pi D \mu_{eff}} \left[\exp\left(-\mu_{eff} z_a \sqrt{\delta^2 + \alpha^2}\right) - \exp\left(-\mu_{eff} z_a \sqrt{\delta^2 + (\alpha + 2\beta)^2}\right) \right]$$

$$\lim_{\mu_s' \to \infty} I^{\Psi^*}_{\delta z_a \leftrightarrow \infty} = \mathop{lim}_{\mu_s' \to \infty} \frac{3S^*}{8\sqrt{2}\pi} \left[\frac{exp\left(-\mu_{eff} z_a \sqrt{\delta^2 + \alpha^2}\right) - exp\left(-\mu_{eff} z_a \sqrt{\delta^2 + (\alpha + 2\beta)^2}\right)}{\mu_{eff} z_a} \right]$$

$$= \mathop{lim}_{\mu_s' \to \infty} \frac{3S^*}{8\sqrt{2}\pi} \times \mathop{lim}_{\mu_{eff} z_a \to 0} \left[\frac{exp\left(-\mu_{eff} z_a \sqrt{\delta^2 + \alpha^2}\right) - exp\left(-\mu_{eff} z_a \sqrt{\delta^2 + (\alpha + 2\beta)^2}\right)}{\mu_{eff} z_a} \right]$$

$$= \frac{3\eta}{8\sqrt{2}\pi} \times \mathop{lim}_{x \to 0} \left[\frac{exp\left(-x\sqrt{\delta^2+\alpha^2}\right) - exp\left(-x\sqrt{\delta^2+(\alpha+2\beta)^2}\right)}{x} \right] \tag{V-25}$$

By using L'Hospital's Rule, as detailed in Appendix 5,

The first term is

$$\lim_{\mu_s' \to \infty} I^{\Psi^*}_{\delta z_a \leftrightarrow \infty} = \frac{3\eta}{8\sqrt{2}\pi} \sqrt{\delta^2 + \left(\alpha + \frac{4A}{3}\right)^2} - \sqrt{\delta^2 + \alpha^2} = \sim 32.59\% \tag{V-26}$$

Calculate the second term,

$$\lim_{\mu_s' \to \infty} I^{\Psi^*}_{b \leftrightarrow \infty} = \lim_{\mu_s' \to \infty} \frac{S^*}{8\sqrt{2}\pi D \mu_{eff}} \left[\exp\left(-\mu_{eff} z_a \sqrt{\xi^2 + \alpha^2}\right) - \exp\left(-\mu_{eff} z_a \sqrt{\xi^2 + (\alpha + 2\beta)^2}\right) \right] \tag{V-27}$$

Rewrite it as

$$\lim_{\mu_s'\to\infty} I_{b\leftrightarrow\infty}^{\Psi^*} = \lim_{\mu_s'\to\infty} \frac{S^*}{8\sqrt{2}\pi}\left[\frac{exp\left(-\mu_{eff}\sqrt{b^2+(\alpha z_{\boldsymbol{a}})^2}\right)-exp\left(-\mu_{eff}\sqrt{b^2+(\alpha z_{\boldsymbol{a}}+2\beta z_a)^2}\right)}{D\mu_{eff}}\right] \quad \text{(V-28)}$$

Apply the following Taylor series expansion at x = 0 to the first two order in the derivation as detailed in Appendix 6,

$\sqrt{1+x} = 1+\frac{1}{2}x,$

$\sqrt{a^2+x} = a+\frac{1}{2a}x$, (a>0)

$exp(-x) = 1-x$

The second term result

$$\lim_{\mu_s'\to\infty} I_{b\leftrightarrow\infty}^{\Psi^*} = \lim_{\mu_s'\to\infty} \frac{3\eta}{8\sqrt{2}\pi}\left[exp\left(-\mu_{eff}b\right)\left(\frac{\frac{8A}{3}(\alpha+\frac{2A}{3})}{\mu_s' d_{area}}\right)\right] = 0 \quad \text{(V-29)}$$

At last, the slave fluence rate component is

$$\lim_{\mu_s'\to\infty} I_{\delta z_a\leftrightarrow b}^{\Psi^*} = \sim 32.59\% \quad \text{(V-30)}$$

c) Master flux z-direction component

$$\lim_{\mu_s'\to\infty} I_{\delta z_a\leftrightarrow b}^{JZ} = \lim_{\mu_s'\to\infty} I_{\delta z_a\leftrightarrow\infty}^{JZ} - \lim_{\mu_s'\to\infty} I_{b\leftrightarrow\infty}^{JZ} \quad \text{(V-31)}$$

Calculate the first term

$$\lim_{\mu_s'\to\infty} I_{\delta z_a\leftrightarrow\infty}^{JZ}$$

$$= \lim_{\mu_s'\to\infty} \frac{3}{8\sqrt{2}\pi}\left[\frac{1}{\sqrt{\delta^2+1}}\exp\left(-\mu_{eff} z_a\sqrt{\delta^2+1}\right)+\frac{(1+2\beta)}{\sqrt{\delta^2+(1+2\beta)^2}}\exp\left(-\mu_{eff} z_a\sqrt{\delta^2+(1+2\beta)^2}\right)\right] \quad \text{(V-32)}$$

Refer to Appendix 2, $\mu_{eff} z_a \to 0$ as $\mu_s' \to \infty$. The two exponential terms above approaches one, hence,

$$\lim_{\mu_s'\to\infty} I^{JZ}_{\delta z_a\leftrightarrow\infty} = \lim_{\mu_s'\to\infty} \frac{3}{8\sqrt{2}\pi}\left[\frac{1}{\sqrt{\delta^2+1}} + \frac{(1+2\beta)}{\sqrt{\delta^2+(1+2\beta)^2}}\right] \tag{V-33}$$

$$\lim_{\mu_s'\to\infty} I^{JZ}_{\delta z_a\leftrightarrow\infty} = \frac{3}{8\sqrt{2}\pi}\left[\frac{1}{\sqrt{\delta^2+1}} + \frac{\left(1+\frac{4A}{3}\right)}{\sqrt{\delta^2+\left(1+\frac{4A}{3}\right)^2}}\right] = \sim 15.95\% \tag{V-34}$$

Now calculate the second term

$$\lim_{\mu_s'\to\infty} I^{JZ}_{b\leftrightarrow\infty}$$

$$= \lim_{\mu_s'\to\infty} \frac{3}{8\sqrt{2}\pi}\left[\frac{1}{\sqrt{\xi^2+1}}\exp\left(-\mu_{\mathrm{eff}} z_a\sqrt{\xi^2+1}\right) + \frac{(1+2\beta)}{\sqrt{\xi^2+(1+2\beta)^2}}\exp\left(-\mu_{\mathrm{eff}} z_a\sqrt{\xi^2+(1+2\beta)^2}\right)\right] \tag{V-35}$$

Rewrite it as below:

$$\lim_{\mu_s'\to\infty} \frac{3}{8\sqrt{2}\pi}\left[\frac{z_a}{\sqrt{b^2+(z_a)^2}}exp\left(-\mu_{eff}\sqrt{b^2+(z_a)^2}\right) + \frac{(z_a+2z_b)}{\sqrt{b^2+(z_a+2z_b)^2}}exp\left(-\mu_{eff}\sqrt{b^2+(z_a+2z_b)^2}\right)\right] \tag{V-36}$$

Further simplify it by applying Taylor series expansion as detailed in Appendix 7.

The second term reaches zero:

$$\lim_{\mu_s'\to\infty} I^{JZ}_{b\leftrightarrow\infty} = \lim_{\mu_s'\to\infty} \frac{3}{8\sqrt{2}\pi} exp\left(-\mu_{eff} b\right)\frac{4\left(1+\frac{2A}{3}\right)}{\mu_s' d_{area}} = 0 \tag{V-37}$$

At last, the master flux z-direction component is

$$\lim_{\mu_s'\to\infty} I^{JZ}_{\delta z_a\leftrightarrow b} = \sim 15.95\% \tag{V-38}$$

d) Slave flux z-direction component

$$\lim_{\mu_s'\to\infty} I^{\mathrm{JZ}^*}_{\delta \mathrm{z_a}\leftrightarrow \mathrm{b}} = \lim_{\mu_s'\to\infty} I^{\mathrm{JZ}^*}_{\delta z_a\leftrightarrow\infty} - \lim_{\mu_s'\to\infty} I^{\mathrm{JZ}^*}_{b\leftrightarrow\infty} \tag{V-39}$$

Calculate the first term,

$I^{\mathrm{JZ}^*}_{\delta z_a \leftrightarrow \infty} =$

$$\frac{3S^*}{8\sqrt{2}\pi}\left[\frac{\alpha}{\sqrt{\delta^2+\alpha^2}}\exp\left(-\mu_{\mathrm{eff}}\mathrm{z_a}\sqrt{\delta^2+\alpha^2}\right)+\frac{(\alpha+2\beta)}{\sqrt{\delta^2+(\alpha+2\beta)^2}}\exp\left(-\mu_{\mathrm{eff}}\mathrm{z_a}\sqrt{\delta^2+(\alpha+2\beta)^2}\right)\right] \tag{V-40}$$

Refer to Appendix 2, $\mu_{\mathrm{eff}}\mathrm{z_a} \rightarrow 0$ as $\mu_s' \rightarrow \infty$. The two exponential terms above approaches to one.

So,

$$\lim_{\mu_s' \to \infty} I^{JZ}_{\delta z_a \leftrightarrow \infty} = \lim_{\mu_s' \to \infty} \frac{3S^*}{8\sqrt{2}\pi}\left[\frac{\alpha}{\sqrt{\delta^2+\alpha^2}}+\frac{(\alpha+2\beta)}{\sqrt{\delta^2+(\alpha+2\beta)^2}}\right] \tag{V-41}$$

$$\lim_{\mu_s' \to \infty} I^{JZ}_{\delta z_a \leftrightarrow \infty} = \frac{3\eta}{8\sqrt{2}\pi}\left[\frac{\alpha}{\sqrt{\delta^2+\alpha^2}}+\frac{\left(\alpha+\frac{4A}{3}\right)}{\sqrt{\delta^2+\left(\alpha+\frac{4A}{3}\right)^2}}\right] = \sim 8.38\% \tag{V-42}$$

Now calculate the second term,

$\lim\limits_{\mu_s' \to \infty} I^{\mathrm{JZ}^*}_{b \leftrightarrow \infty} =$

$$\frac{3S^*}{8\sqrt{2}\pi}\left[\frac{\alpha}{\sqrt{\xi^2+\alpha^2}}\exp\left(-\mu_{\mathrm{eff}}\mathrm{z_a}\sqrt{\xi^2+\alpha^2}\right)+\frac{(\alpha+2\beta)}{\sqrt{\xi^2+(\alpha+2\beta)^2}}\exp\left(-\mu_{\mathrm{eff}}\mathrm{z_a}\sqrt{\xi^2+(\alpha+2\beta)^2}\right)\right] \tag{V-43}$$

Rewrite it as

$$\lim_{\mu_s' \to \infty} I^{\mathrm{JZ}^*}_{b \leftrightarrow \infty} = \frac{3S^*}{8\sqrt{2}\pi}\left[\frac{z_a^*}{\sqrt{b^2+(z_a^*)^2}}exp\left(-\mu_{eff}\sqrt{b^2+(z_a^*)^2}\right)+\right.$$

$$\left.\frac{(z_a^*+2z_b)}{\sqrt{b^2+(z_a^*+2z_b)^2}}\exp\left(-\mu_{eff}\sqrt{b^2+(z_a^*+2z_b)^2}\right)\right] \tag{V-44}$$

Further simplify it by applying Taylor series expansion as detailed in Appendix 8.

The second term reaches zero.

$$\lim_{\mu_s' \to \infty} I^{JZ^*}_{b \leftrightarrow \infty} = \lim_{\mu_s' \to \infty} \frac{3\eta}{8\sqrt{2}\pi} exp\left(-\mu_{eff}b\right)\left\{\frac{4\left(\alpha+\frac{2A}{3}\right)}{\mu_s' d_{area}}\right\} = 0 \tag{V-45}$$

At last, the master flux z-direction component is

$$\lim_{\mu_s' \to \infty} I^{JZ^*}_{b \leftrightarrow \infty} = \sim 8.38\% \tag{V-46}$$

e) Summary of saturation level

$$\lim_{\mu_s'\to\infty} I_{0\leftrightarrow\delta \mathrm{z_a}} = \sim 4.86\%$$

$$\lim_{\mu_s'\to\infty} I^{\Psi}_{\delta \mathrm{z_a}\leftrightarrow \mathrm{b}} = \frac{3}{8\sqrt{2}\pi}\left[\sqrt{\delta^2+\left(1+\frac{4A}{3}\right)^2}-\sqrt{\delta^2+1}\right] = \sim 36.78\%$$

$$\lim_{\mu_s'\to\infty} I^{\Psi^*}_{\delta \mathrm{z_a}\leftrightarrow \mathrm{b}} = \frac{3\eta}{8\sqrt{2}\pi}\sqrt{\delta^2+\left(\alpha+\frac{4A}{3}\right)^2}-\sqrt{\delta^2+\alpha^2} = \sim 32.59\%$$

$$\lim_{\mu_s'\to\infty} I^{\mathrm{JZ}}_{\delta \mathrm{z_a}\leftrightarrow \mathrm{b}} = \frac{3}{8\sqrt{2}\pi}\left[\frac{1}{\sqrt{\delta^2+1}}+\frac{\left(1+\frac{4A}{3}\right)}{\sqrt{\delta^2+\left(1+\frac{4A}{3}\right)^2}}\right] = \sim 15.95\%$$

$$\lim_{\mu_s'\to\infty} I^{\mathrm{JZ}^*}_{\delta \mathrm{z_a}\leftrightarrow \mathrm{b}} = \frac{3\eta}{8\sqrt{2}\pi}\left[\frac{\alpha}{\sqrt{\delta^2+\alpha^2}}+\frac{\left(\alpha+\frac{4A}{3}\right)}{\sqrt{\delta^2+\left(\alpha+\frac{4A}{3}\right)^2}}\right] = \sim 8.38\%$$

The saturation predicted our model before including effect of numerical aperture is

$$\mathrm{I_{satu}} = \lim_{\mu_s'\to\infty} I_{0\leftrightarrow\delta \mathrm{z_a}} + \lim_{\mu_s'\to\infty} I^{\Psi}_{\delta \mathrm{z_a}\leftrightarrow \mathrm{b}} + \lim_{\mu_s'\to\infty} I^{\Psi^*}_{\delta \mathrm{z_a}\leftrightarrow \mathrm{b}} + \lim_{\mu_s'\to\infty} I^{\mathrm{JZ}}_{\delta \mathrm{z_a}\leftrightarrow \mathrm{b}} + \lim_{\mu_s'\to\infty} I^{\mathrm{JZ}^*}_{\delta \mathrm{z_a}\leftrightarrow \mathrm{b}} = 97.56\% \tag{V-47}$$

As scattering approaches infinite, light collection efficiency will collapse down to η_{lim}, equal of ~2.47% for a fiber with NA = 0.22, and tissue refraction index = 1.4.

$$\eta_c = \eta_{lim}\left[1+1.55\exp(-6.82\mu_s' d_{fiber})\right] = \eta_{lim} = \left(\frac{NA}{n_{tiss}}\right)^2 \tag{V-48}$$

The saturation predicted our model after including effect of numerical aperture is

$$\mathrm{I^{NA}_{satu}} = \eta_{lim} \times \mathrm{I_{satu}} = \sim 2.41\% \tag{V-49}$$

5.2.3 The transition point prior to saturation

From Eq. (IV-29), we know that inner-field contributed total diffuse reflectance is calculated by using adaptation technique with which any arbitrary μ_s' is mapped back to $\mu_s' = 1mm^{-1}$ case. Hence inner-field component no longer has dependency on scattering, and does not contribute to the calculation of transition point.

a) Transition point of master fluence rate component

Prior to saturation,

$$\lim_{\mu_s' \to \infty} I^{\Psi}_{\delta \mathrm{z_a} \leftrightarrow \mathrm{b}} = \frac{3}{8\sqrt{2}\pi}\left[\sqrt{\delta^2 + \left(1+\frac{4A}{3}\right)^2} - \sqrt{\delta^2+1}\right] - \lim_{\mu_s' \to \infty} \frac{3}{8\sqrt{2}\pi} exp\left(-\mu_{eff} b\right) \frac{4\beta(1+\beta)}{\mu_s' d_{area}} \quad \text{(V-50)}$$

$$\lim_{\mu_s' \to \infty} I^{\Psi}_{\delta \mathrm{z_a} \leftrightarrow \mathrm{b}} = \frac{3}{8\sqrt{2}\pi}\left[\sqrt{\delta^2 + \left(1+\frac{4A}{3}\right)^2} - \sqrt{\delta^2+1}\right] - \lim_{\mu_s' \to \infty} \frac{3}{8\sqrt{2}\pi} exp\left(-\mu_{eff} b\right) \frac{\frac{8A}{3}\left(1+\frac{2A}{3}\right)}{\mu_s' d_{area}} \quad \text{(V-51)}$$

$$\lim_{\mu_s' \to \infty} I^{\Psi}_{\delta \mathrm{z_a} \leftrightarrow \mathrm{b}} = \frac{3}{8\sqrt{2}\pi}\left[\sqrt{\delta^2 + \left(1+\frac{4A}{3}\right)^2} - \sqrt{\delta^2+1}\right] \lim_{\mu_s' \to \infty} \left[1 - exp\left(1-\mu_{eff} b\right) \frac{P_1}{\mu_s' d_{area}}\right] \quad \text{(V-52)}$$

Where

$$P_1 = \frac{\frac{8A}{3}\left(1+\frac{2A}{3}\right)}{\sqrt{\delta^2+\left(1+\frac{4A}{3}\right)^2} - \sqrt{\delta^2+1}} = \sim 6.48 \quad \text{(V-53)}$$

Denote transition factor T_{factor} as

$$T_{factor} = \frac{P_1}{\mu_s' d_{area}} = \frac{\sim 6.48}{\mu_s' d_{area}} \quad \text{(V-54)}$$

$$\lim_{\mu_s' \to \infty} I^{\Psi}_{\delta \mathrm{z_a} \leftrightarrow \mathrm{b}} = 36.78\% \times \lim_{\mu_s' \to \infty} \left[1 - exp\left(-\mu_{eff} b\right) T_{factor}\right] \quad \text{(V-55)}$$

As μ_s' is increasing toward infinite, $I^{\Psi}_{\delta \mathrm{z_a} \leftrightarrow \mathrm{b}}$ is moving upward saturation plateau, while the term $exp\left(-\mu_{eff} b\right) T_{factor}$ is decreasing downward to zero. Essentially, it is the decreasing speed of $exp\left(-\mu_{eff} b\right) T_{factor}$ that determines the increasing speed of $I^{\Psi}_{\delta \mathrm{z_a} \leftrightarrow \mathrm{b}}$and , T_{factor} further modulates the exponentially deceasing speed of $exp\left(-\mu_{eff} b\right)$.

When $T_{factor} > 1$, namely $\mu_s' d_{area} < 4.86$, $I^{\Psi}_{\delta \mathrm{z_a} \leftrightarrow \mathrm{b}}$ tends to increase fast and very sensitive to scattering change, as observed in diffusion region shown in Figure V-5.

When $T_{factor} < 1$, namely $\mu_s' d_{area} > 4.86$, $I^{\Psi}_{\delta \mathrm{z_a} \leftrightarrow \mathrm{b}}$ tends to increase slower than above case. Especially when $T_{factor} \to 0$, $I^{\Psi}_{\delta \mathrm{z_a} \leftrightarrow \mathrm{b}}$ will stop increasing, as observed in saturation zone in Figure V-5.

Hence, the $T_{factor} = 1$, namely $\mu_s' d_{area} = 4.86$, will correspond to a sensitive point where increasing rate of $I^{\Psi}_{\delta \mathrm{z_a} \leftrightarrow \mathrm{b}}$ undergoes a substantial change, which is the transition point we are seeking for slave fluence rate component.

b) Transition point of slave fluence rate component

Prior to saturation,

$$\lim_{\mu_s' \to \infty} I^{\Psi^*}_{\delta \mathrm{z_a} \leftrightarrow \mathrm{b}} = \frac{3\eta}{8\sqrt{2}\pi} \left[\sqrt{\delta^2 + \left(\alpha + \frac{4A}{3} \right)^2} - \sqrt{\delta^2 + \alpha^2} \right] - \lim_{\mu_s' \to \infty} \frac{3\eta}{8\sqrt{2}\pi} \left[exp\left(-\mu_{eff} b \right) \left(\frac{\frac{8A}{3}(\alpha + \frac{2A}{3})}{\mu_s' d_{area}} \right) \right] \quad \text{(V-56)}$$

$$\lim_{\mu_s' \to \infty} I^{\Psi^*}_{\delta \mathrm{z_a} \leftrightarrow \mathrm{b}} = \frac{3\eta}{8\sqrt{2}\pi} \left[\sqrt{\delta^2 + \left(\alpha + \frac{4A}{3} \right)^2} - \sqrt{\delta^2 + \alpha^2} \right] \lim_{\mu_s' \to \infty} \left[1 - exp\left(-\mu_{eff} b \right) \left(\frac{P_2}{\mu_s' d_{area}} \right) \right] \quad \text{(V-57)}$$

Where

$$P_2 = \frac{\frac{8A}{3}(\alpha + \frac{2A}{3})}{\sqrt{\delta^2 + \left(\alpha + \frac{4A}{3} \right)^2} - \sqrt{\delta^2 + \alpha^2}} = \sim 4.86 \quad \text{(V-58)}$$

Denote transition factor T_{factor} as

$$T_{factor} = \frac{P_2}{\mu_s' d_{area}} = \frac{4.86}{\mu_s' d_{area}} \quad \text{(V-59)}$$

$$\lim_{\mu_s' \to \infty} I^{\Psi^*}_{\delta \mathrm{z_a} \leftrightarrow \mathrm{b}} = 32.59\% \times \lim_{\mu_s' \to \infty} \left[1 - exp\left(-\mu_{eff} b \right) T_{factor} \right] \quad \text{(V-60)}$$

As μ_s' is increasing toward infinite, $I^{\Psi^*}_{\delta \mathrm{z_a} \leftrightarrow \mathrm{b}}$ is moving upward saturation plateau, while the term $exp(-\mu_{eff} b) T_{factor}$ is decreasing downward to zero. Essentially, it is the decreasing speed of

$exp\left(-\mu_{eff}b\right)T_{factor}$ that determines the increasing speed of $I^{\Psi^*}_{\delta \mathrm{z_a} \leftrightarrow \mathrm{b}}$, and , T_{factor} further modulates the exponentially deceasing speed of $exp\left(-\mu_{eff}b\right)$.

When $T_{factor} > 1$, namely $\mu_s' d_{area} < 4.86$, $I^{\Psi^*}_{\delta \mathrm{z_a} \leftrightarrow \mathrm{b}}$ tends to increase fast and very sensitive to scattering change, as observed in diffusion region shown in Figure V-5.

When $T_{factor} < 1$, namely $\mu_s' d_{area} > 4.86$, $I^{\Psi^*}_{\delta \mathrm{z_a} \leftrightarrow \mathrm{b}}$ tends to increase slower than above case. Especially when $T_{factor} \to 0$, $I^{\Psi^*}_{\delta \mathrm{z_a} \leftrightarrow \mathrm{b}}$ will stop increasing, as observed in saturation zone in Figure V-5..

Hence, the $T_{factor} = 1$, namely $\mu_s' d_{area} = 4.86$, will correspond to a sensitive point where increasing rate of $I^{\Psi^*}_{\delta \mathrm{z_a} \leftrightarrow \mathrm{b}}$ undergoes a substantial change, which is the transition point we are seeking for slave fluence rate component.

c) Transition point of master flux z-direction component

Prior to saturation,

$$\lim_{\mu_s' \to \infty} I^{JZ}_{\delta z_a \leftrightarrow b} = \frac{3}{8\sqrt{2}\pi}\left[\frac{1}{\sqrt{\delta^2+1}} + \frac{\left(1+\frac{4A}{3}\right)}{\sqrt{\delta^2+\left(1+\frac{4A}{3}\right)^2}}\right] - \lim_{\mu_s' \to \infty} \frac{3}{8\sqrt{2}\pi} exp\left(-\mu_{eff}b\right)\frac{4\left(1+\frac{2A}{3}\right)}{\mu_s' d_{area}} \qquad \text{(V-61)}$$

$$\lim_{\mu_s' \to \infty} I^{JZ}_{\delta z_a \leftrightarrow b} = \sim 15.95\% \times \lim_{\mu_s' \to \infty}\left[1 - exp\left(-\mu_{eff}b\right)\frac{P_3}{\mu_s' d_{area}}\right] \qquad \text{(V-62)}$$

Where

$$P_3 = \frac{4\left(1+\frac{2A}{3}\right)}{\frac{1}{\sqrt{\delta^2+1}} + \frac{\left(1+\frac{4A}{3}\right)}{\sqrt{\delta^2+\left(1+\frac{4A}{3}\right)^2}}} = \sim 6.70 \qquad \text{(V-63)}$$

Denote transition factor T_{factor} as

$$T_{factor} = \frac{P_3}{\mu_s' d_{area}} = \frac{6.70}{\mu_s' d_{area}} \qquad \text{(V-64)}$$

As μ_s' is increasing toward infinite, $I_{\delta z_a \leftrightarrow b}^{JZ}$ is moving upward saturation plateau, while the term $exp\left(-\mu_{eff} b\right) T_{factor}$ is decreasing downward to zero. Essentially, it is the decreasing speed of $exp\left(-\mu_{eff} b\right) T_{factor}$ that determines the increasing speed of$I_{\delta z_a \leftrightarrow b}^{JZ}$, and , T_{factor} further modulates the exponentially deceasing speed of $exp\left(-\mu_{eff} b\right)$.

When $T_{factor} > 1$, namely $\mu_s' d_{area} < 6.70$, $I_{\delta z_a \leftrightarrow b}^{JZ}$tends to increase fast and very sensitive to scattering change, as observed in diffusion region shown in Figure V-5.

When $T_{factor} < 1$, namely $\mu_s' d_{area} > 6.70$, $I_{\delta z_a \leftrightarrow b}^{JZ}$tends to increase slower than above case. Especially when $T_{factor} \rightarrow 0$, $I_{\delta z_a \leftrightarrow b}^{JZ}$ will stop increasing, as observed in saturation zone in Figure V-5.

Hence, the $T_{factor} = 1$, namely $\mu_s' d_{area} = 6.70$, will correspond to a sensitive point where increasing rate of $I_{\delta z_a \leftrightarrow b}^{JZ}$ undergoes a substantial change, which is the transition point we are seeking for slave fluence rate component.

d) Transition point of slave flux z-direction component

Prior to saturation,

$$\lim_{\mu_s' \to \infty} I_{b \leftrightarrow \infty}^{JZ^*} = \frac{3\eta}{8\sqrt{2}\pi} \left[\frac{\alpha}{\sqrt{\delta^2+\alpha^2}} + \frac{\left(\alpha+\frac{4A}{3}\right)}{\sqrt{\delta^2+\left(\alpha+\frac{4A}{3}\right)^2}} \right] - \lim_{\mu_s' \to \infty} \frac{3\eta}{8\sqrt{2}\pi} exp\left(-\mu_{eff} b\right) \left\{ \frac{4\left(\alpha+\frac{2A}{3}\right)}{\mu_s' d_{area}} \right\} \tag{V-65}$$

$$\lim_{\mu_s' \to \infty} I_{b \leftrightarrow \infty}^{JZ^*} = 8.38\% \times \lim_{\mu_s' \to \infty} \left[1 - exp\left(-\mu_{eff} b\right) \frac{P_4}{\mu_s' d_{area}} \right] \tag{V-66}$$

Where

$$P_4 = \frac{4\left(\alpha+\frac{2A}{3}\right)}{\frac{\alpha}{\sqrt{\delta^2+\alpha^2}} + \frac{\left(\alpha+\frac{4A}{3}\right)}{\sqrt{\delta^2+\left(\alpha+\frac{4A}{3}\right)^2}}} = \sim 8.73 \tag{V-67}$$

Denote transition factor T_{factor} as

$$T_{factor} = \frac{P_4}{\mu_s' d_{area}} = \frac{8.73}{\mu_s' d_{area}} \qquad \text{(V-68)}$$

As μ_s' is increasing toward infinite, $I_{b\leftrightarrow\infty}^{JZ^*}$ is moving upward saturation plateau, while the term $exp\left(-\mu_{eff}b\right)T_{factor}$ is decreasing downward to zero. Essentially, it is the decreasing speed of $exp\left(-\mu_{eff}b\right)T_{factor}$ that determines the increasing speed of $I_{b\leftrightarrow\infty}^{JZ^*}$, and , T_{factor} further modulates the exponentially deceasing speed of $exp\left(-\mu_{eff}b\right)$.

When $T_{factor} > 1$, namely $\mu_s' d_{area} < 8.73$, $I_{b\leftrightarrow\infty}^{JZ^*}$ tends to increase fast and very sensitive to scattering change, as observed in diffusion region shown in Figure V-5.

When $T_{factor} < 1$, namely $\mu_s' d_{area} > 8.73$, $I_{b\leftrightarrow\infty}^{JZ^*}$ tends to increase slower than above case. Especially when $T_{factor} \to 0$, $I_{b\leftrightarrow\infty}^{JZ^*}$ will stop increasing, as observed in saturation zone in Figure V-5.

Hence, the $T_{factor} = 1$, namely $\mu_s' d_{area} = 8.73$, will correspond to a sensitive point where increasing rate of $I_{b\leftrightarrow\infty}^{JZ^*}$ undergoes a substantial change, which is the transition point we are seeking for slave fluence rate component.

e) Summary of transition points

$$P_1 = \frac{\frac{8A}{3}\left(1 + \frac{2A}{3}\right)}{\sqrt{\delta^2 + \left(1 + \frac{4A}{3}\right)^2} - \sqrt{\delta^2 + 1}} = {\sim}6.48$$

$$P_2 = \frac{\frac{8A}{3}\left(\alpha + \frac{2A}{3}\right)}{\sqrt{\delta^2 + \left(\alpha + \frac{4A}{3}\right)^2} - \sqrt{\delta^2 + \alpha^2}} = {\sim}4.86$$

$$P_3 = \frac{4\left(1+\frac{2A}{3}\right)}{\frac{1}{\sqrt{\delta^2+1}}+\frac{\left(1+\frac{4A}{3}\right)}{\sqrt{\delta^2+\left(1+\frac{4A}{3}\right)^2}}} = \sim 6.70$$

$$P_4 = \frac{4\left(\alpha+\frac{2A}{3}\right)}{\frac{\alpha}{\sqrt{\delta^2+\alpha^2}}+\frac{\left(\alpha+\frac{4A}{3}\right)}{\sqrt{\delta^2+\left(\alpha+\frac{4A}{3}\right)^2}}} = \sim 8.73$$

The transition point for entire model is defined as the mean of above four transition points with each weighted by its corresponding saturation level divided by 92.71% which is sum of our components of outer-field total, as shown in equation below. Because inner-field model does not affect any transition, the weight calculation excludes the inner-field contributed saturation level in denominator.

$$P_{trans} = \frac{36.78\%}{92.71\%}P_1 + \frac{32.59\%}{92.71\%}P_2 + \frac{15.95\%}{92.71\%}P_3 + \frac{8.38\%}{92.71\%}P_4 = \sim 6.48 \qquad \text{(V-69)}$$

5.2 Results and Discussion

5.3.1 Saturation level

Our model predicts a saturation level of 97.56% before adding the effect of numerical aperture. To validate this result, we use MC simulated total diffuse reflectance collected from an absorption-free medium with large reduced scattering coefficient μ_s' of 1000 mm^{-1} for comparison, since we cannot simulate infinite large reduced scattering in monte-carlo. The collection area d_{area} is set 1mm, g = 0.9, $n_{tiss} = 1.4$, the medium thickness is 1000mm, and the rest parameters are consistent with previously used. Three different illumination geometries are investigated, including center-illumination, gaussian-type illumination with FWHM beam diameter of 0.5mm, and a uniform circular area illumination. For center-illumination geometry, the MC predicted saturation level is 95.62%; for area-illumination geometry with gaussian-type intensity profile, the MC predicted saturation level is 94.64%, and for area-illumination geometry with uniform intensity profile, the MC predicted saturation level is 94.30%.

After including the effect of numerical aperture, our model predicts a saturation level of 2.41% for SfRS measurement. Since we have no access to MC simulated data with NA included, we compare our results with the saturation level predicted by Kanick's model. When μ_s' goes to infinite, Kanick's model reduces to $\eta_{lim} =$ 2.47%, very close to our result.

From the section 5.2.2, we know that the saturation level is dependent upon anisotropy g and tissue refraction index n_{tiss}, which vary in a small range for biological tissue. The above results are calculated based on the typical value g=0.9 and $n_{tiss} = 1.4$. When g varies within [0.5, 0.99] and $n_{tiss} = 1.4$, the saturation level varies in a narrow band between 96.67% and 98.41%.

5.3.2 Transition point

Our model predicts a transition point of $\mu_s' d_{fib} =$ ~6.48, close to the visually observed transition point $\mu_s' d_{fib} =$ ~10 from MC simulated data with absorption coefficient μ_a equal to zero or very weak. From section 5.2.3, though the transition point also has dependency on anisotropy g and tissue refraction index n_{tiss}, numerical test shows that it stays stably at a value of 6.48 when g varies between [0.5, 0.99].

Interestingly, our derivation shows that the four components of outer-field model have different transition points, ~6.48 for master fluence rate component, ~4.86 for slave fluence rate component, ~6.70 for mater flux z-direction component, and ~8.73 for slave flux z-direction component. And the final transition point ~6.48 which is calculated as weighted mean of the four above, equals the transition point of master fluence rate component. Thus, we predict that when decomposing the outer-field model into four components and plotting them together against $\mu_s' d_{area}$, we shall be able to visually observe the following effects:

1) The slave fluence rate will transition into saturation stage earlier than other three components.

2) The master fluence rate component and master flux z-direction component will have approximate at the same position.

3) The slave flux z-direction component will the last one that transition into saturation stage.

4) The whole model shall transition to saturation at same position with master fluence rate.

5) The four components shall saturate at different levels at high scattering end, corresponding to the results derived in section 5.2.2.e.

To test above prediction, we plot the model decomposition against $\mu_s' d_{area}$ in an example described as below: $\mu_s' = [10^{-2}, 10^5]mm^{-1}$, g = 0.9, $d_{area} = 1mm^{-1}$, $\mu_a = 0.01mm^{-1}$, $n_{tiss} = 1.4$. As shown in following figure, when $\mu_s' d_{area}$ is larger than 2δ, namely $\mu_s' \geq 1mm^{-1}$ in this example, the entire model consists of five components, and they saturate at different level that match our derivation. The sequence of transition point also matches the expectation above.

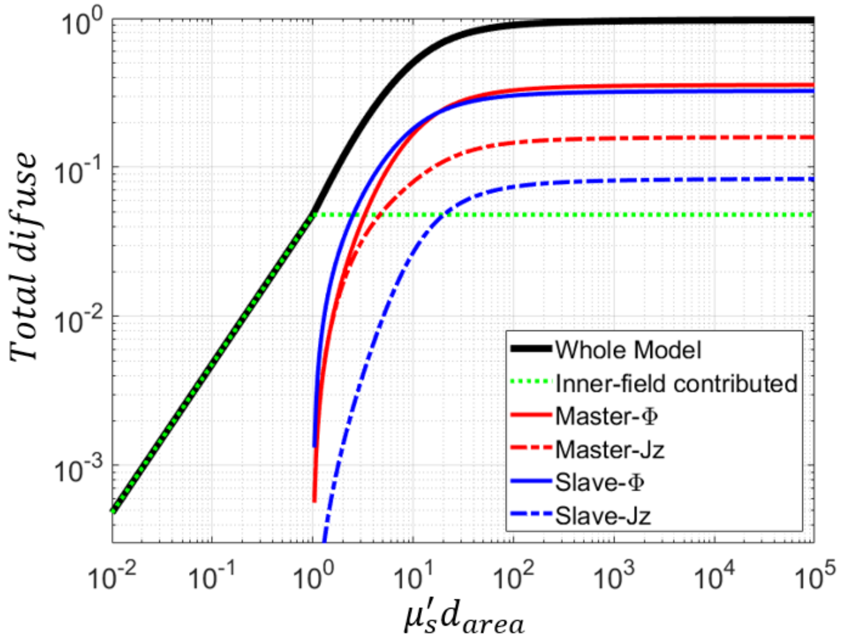

Figure V-5 Decomposition of model shows different levels of saturation and transition points as derived.

5.3.3 Anisotropy-sensitive zone

The g-sensitive zone is observed in low-scattering region. In our model construction, when $\mu_s' d_{area}$ is less than 2δ, namely $\mu_s' \leq 1mm^{-1}$ for $d_{area} = 1mm^{-1}$, the total diffuse reflectance collected by a single fiber probe is solely dominated by the inner-field model. Therefore, this g-sensitive zone is mainly affected by our inner-field model as formularized in Eq. (IV-29). The following figure presents the g-dependency predicted by our model. From part A, we see that g-sensitive zone is mainly observed from the region where inner-field model completely dominates. In part B, we choose three weak scattering conditions $\mu_s' = [0.01, 0.05, 0.1]mm^{-1}$ and plot total diffuse reflectance plotted against anisotropy factor g from 0.5 up to 0.99. As the increase of anisotropy factor, which means stronger forward scattering properties, the total diffuser reflectance tends to decrease as expected.

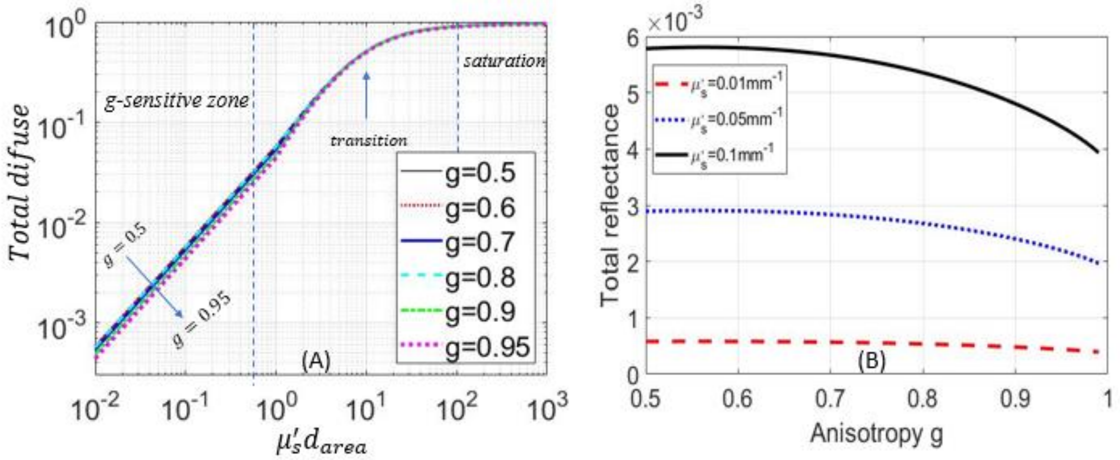

Figure V-6 the g-dependency in low scattering region modeled by inner-field model.

5.4 Summary

Chapter IV demonstrated an integration model for steady-state diffuse reflectance associated with a single-fiber applicator-probe that agrees numerically with a long-standing semi-empirical model [2, 18-20, 32, 34, 35, 39]. In this Chapter, the integration model is based upon to address several characteristic features manifested by Kanick's semi-empirical model. Kanick's semi-empirical model has pictured the following zones of single-fiber diffuse reflectance, at the absence of absorption: (1) A saturation zone wherein the diffuse reflectance approaches 0.97 before scaled down by fiber collection efficiency 2.47% at high-scattering end, as the dimensionless reduced scattering coefficient scaled to the fiber-diameter escalates to $\mu_s' d_{area}$~100. (2) A diffusion zone wherein the diffuse reflectance increases as the reduced scattering coefficient increases but remains insensitive to the anisotropy factor and that transits softly to the saturation zone at $\mu_s' d_{area}$ approximately within [5, 10]. (3) A weak-scattering zone, wherein the increase of the diffuse reflectance as a function of the reduced scattering coefficient is also affected by the anisotropy factor (for g=0.5 to 0.9 with the HG phase function). These features of steady-state single-fiber diffuse reflectance are examined by using the integration model of Chapter IV in the general presence of absorption. For the saturation zone, the integration model analytically arrives at a saturation level of 97.57% before scaled down by fiber collection efficiency 2.47% at high-scattering end. For the diffusion zone, the integration model mandates the transition from it to the saturation zone to occur at approximately $\mu_s' d_{fib} \sim 6.48$, in addition to revealing the dependence of the diffuse reflectance upon the reduced scattering. For the weak-scattering zone, the integration model conveniently delivers the dependence of the diffuse reflectance upon the anisotropy factor at the same level of reduced scattering. The analytically originated approach demonstrated in this thesis combined provides a model approach to diffuse reflectance associated with single fiber applicator probe that will also be useful to modeling time-domain and fluorescence-domain SfRS configurations wherein model-based understandings of the forward measurements have much to improve.

CHAPTER VI

MODELING OF TIME-DOMAIN SFRS

6.1 Introduction

Time-domain technique injects an extremely short pulse of light into tissue and measures the arrival time of reemitted photons that represents the path length one photon travels inside tissue, as illustrated in part A of Figure VI-1 . Hence, it provides the richest information about tissue morphology and physiology, compared to steady-state configuration.

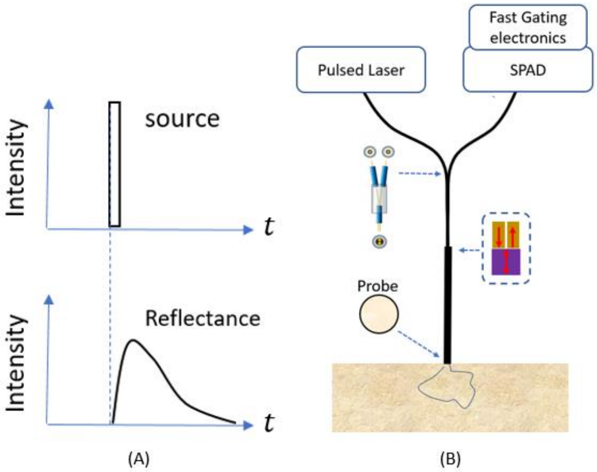

Figure VI-1 Part (A) The principle of time-domain technique; Part (B) An example of implantation of time-domain SfRS.

As shown in part B of Figure VI-1, Time-domain SfRS utilizes a pulsed laser to fire an extremely short pulse and used an ultrafast time-gated single photon avalanche diode (time-gated SPAD) as detector to measure temporal response from tissue. The probe at distal end both injecting light into and collecting remitted light from tissue, can be either a single-fiber probe or a single fiber-bundle probe which bundles small fibers together to form a larger probe dimension.

Time-domain SfRS was first demonstrated experimentally in 2012 by Erik, et al.[17], and so far their study remains the only published work in this field. As shown in Equation below, an incomplete empirical model that need Monte-Carlo simulated data as its input, was adopted to approximately describe time-resolved diffuse reflectance.

$$y_{diff}(\mu_a, \mu_s', t) = k_d(\mu_s') y_0(t) \exp(-\mu_a v t) \tag{VI-1}$$

Where $k_d(\mu_s')$ is a coefficient describing the intensity of diffuse reflectance, $y_0(t)$ is the shape of diffusely reflected curve, and v is the light speed in probed medium. It employs beer-lambert law to separate scattering contribution and absorption contribution, but the reason for its incompleteness is that both $k_d(\mu_s')$ and $y_0(t)$ are not modeled in specific form. To extract μ_a through data fitting, $k_d(\mu_s')$ has to be set as free parameter and $y_0(t)$ is generated by Monte-Carlo simulation at one fixed tissue condition chosen by empirical observation but used for all fittings, as described in their paper. The incompleteness of this model also makes it impossible to extract scattering information from measured time-resolved SfRS signal. More applications of time domain SfRS is impeded by inadequate understanding of the measurement characteristics.

6.2 Theory and Method

6.2.1 The structure of time-domain model

As shown in Figure VI-2, a center-illumination and area collection (CIAC) geometry on semi-infinite air-tissue interface is our concern in time-domain modeling work. The light source is described as $\delta(\rho)\delta(1 - \hat{s} \cdot \hat{z})\delta(t)$, a direction point source that launches a temporal impulse into a homogeneous medium from air along normal direction. The diffusely reflected photons hit at different position on the air-tissue interface at different time, and its spatial and temporal distribution is described by $R(\rho, t)$ due to its cylindrical symmetry to light source and termed as time-domain spatially resolved diffuse reflectance in this work. The circular collection area with diameter d_{area} is centered by the impulsive directional point source. The total diffuse reflectance collected via d_{area} is denoted as $I_{0\leftrightarrow \mathrm{b}}(d_{area}, t)$In addition, both $R(\rho, t)$ and $I_{0\leftrightarrow \mathrm{b}}(d_{area}, t)$ it also depends on tissue optical properties such as absorption coefficient μ_a, reduced scattering coefficient μ_s', anisotropy factor g, and tissue refraction index n_{tiss}, among which g is approximately 0.9 and $n_{tiss} = 1.4$ for biological tissue.

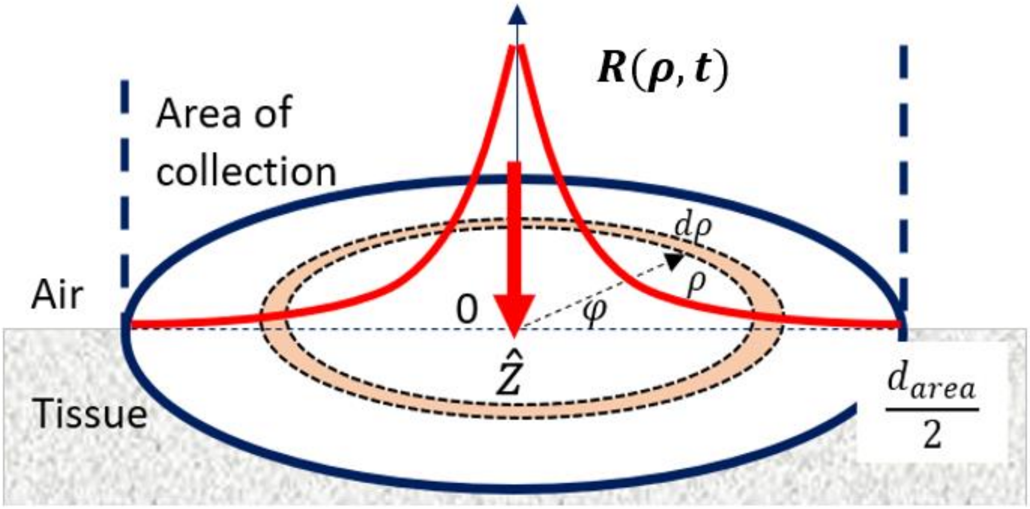

Figure VI-2 The geometry of concern in time-domain work.

The above geometry in this time-domain work is as same as the one in Chapter V steady-state work, except that light source changes to an impulsive directional point from a continuous wave directional point. Thus, for the problem of light propagation in turbid medium, there is an inherent connection between steady-state solution that was already developed in Chapter V and the time-domain solution in this Chapter:

$$R_{ss}(\rho) = \int_0^{\infty} R(\rho, t)dt \quad \text{(VI-2)}$$

$$I_{ss}(d_{area}) = \int_0^{\infty} I(d_{area}, t)dt \quad \text{(VI-3)}$$

Where $R_{ss}(\rho)$ and $I_{ss}(d_{area})$ refer to the models of spatially-resolved diffuse reflectance and total diffuse reflectance in steady-state configuration. Therefore, our time-domain model shares the same concatenation structure as steady-state model, both for $R(\rho, t)$ and $I(d_{area}, t)$. As shown in Figure VI-3, the time-domain spatially resolved diffuse reflectance $R(\rho, t)$ consists of an inner-field model $\mathrm{R}_{\leftarrow\delta}(\rho, \mathrm{t})$ and an outer field model $\mathrm{R}_{\delta\rightarrow}(\rho, \mathrm{t})$ that are bordered by δz_a. The outer-field $\mathrm{R}_{\delta\rightarrow}(\rho, \mathrm{t})$ still employs a master-slave dual sources configuration and has four components, but each component needs to be derived from time-variant diffusion equation. When radius of collection area b is less than δz_a, the total diffuse reflectance $I(d_{area}, t)$ is solely dominated by inner-field model; when b is larger than δz_a, $I(d_{area}, t)$ is contributed by both inner-field model and outer-field model.

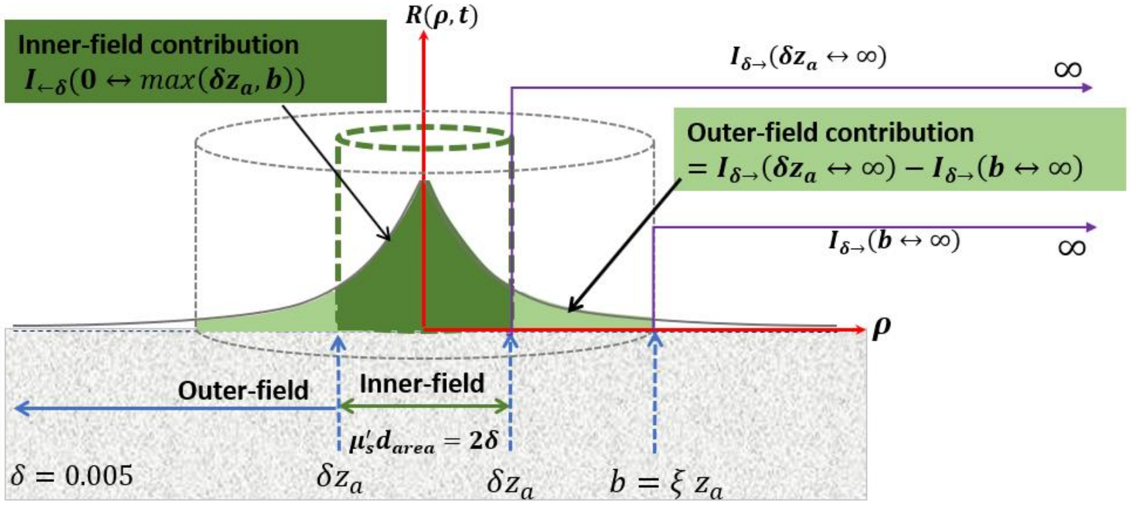

Figure VI-3 The structure of time-domain model

6.2.2 Time-domain spatially resolved diffuse reflectance

a) Inner-field model

The steady-state inner-field model as expressed in Equation (IV-5) is connected to time-domain inner field model $\mathrm{R}_{\delta\rightarrow}(\rho, t)$ by relation:

$$\frac{0.75^g}{2\pi}10^{-(1+p_1\gamma)}\frac{{\mu_s}^2(1-g)^g}{(\mu_s\rho)^{1+p_2\gamma}}\exp(-\gamma)=\int_0^\infty \mathrm{R}_{\leftarrow\delta}(\rho,\mathrm{t})dt \tag{VI-4}$$

The boundary condition that $\mathrm{R}_{\leftarrow\delta}(\rho,\mathrm{t})$ should meet is:

$$\mathrm{R}_{\leftarrow\delta}(\rho,\mathrm{t})|_{t=\infty}=0 \tag{VI-5}$$

We construct the solution of $\mathrm{R}_{\delta\rightarrow}(\rho,t)$ in the following form

$$\mathrm{R}_{\leftarrow\delta}(\rho,\mathrm{t})=\mathrm{h}(\rho)\exp(-\mu_a ct) \tag{VI-6}$$

Substitute it into the right-hand part of Equation (VI-2) and integrate it,

$$\int_0^\infty \mathrm{h}(\rho)\exp(-\mu_a ct)dt=\mathrm{h}(\rho)\frac{1}{-\mu_a c}\exp(-\mu_a ct)\,|_0^\infty=\frac{\mathrm{h}(\rho)}{\mu_a c} \tag{VI-7}$$

Thus $\mathrm{h}(\rho)$ could be easily solved:

$$\mathrm{h}(\rho)=\frac{0.75^g}{2\pi}10^{-(1+p_1\gamma)}\frac{{\mu_s}^2(1-g)^g}{(\mu_s\rho)^{1+p_2\gamma}}\exp(-\gamma)\mu_a c \tag{VI-8}$$

Then the time-domain inner field model is

$$R_{\leftarrow\delta}(\rho,t)=\frac{0.75^g}{2\pi}10^{-(1+p_1\gamma)}\frac{{\mu_s}^2(1-g)^g}{(\mu_s\rho)^{1+p_2\gamma}}exp(-\gamma)(\mu_a c)exp(-\mu_a ct) \tag{VI-9}$$

b) outer-field model

First consider the radiance in infinite homogeneous medium induced by an impulsive isotropic point light source with unity intensity. The time-variant diffusion equation regarding the fluence rate term is expressed in spherical coordinate system as:

$$\nabla^2\widehat{\Psi}(\vec{r},t)-\frac{\mu_a}{D}\widehat{\Psi}(\vec{r},t)-\frac{1}{Dc}\frac{\partial\widehat{\Psi}(\vec{r},t)}{\partial t}=-\frac{\hat{S}\delta\left(\vec{r}-\vec{r'}\right)\delta(t)}{D} \tag{VI-10}$$

Where μ_a is absorption coefficient, D is diffusion coefficient, $\overrightarrow{r'}$ is the position of light source, $\vec{r}$ is the observation point. The solution to above is well-studied and expressed as:

$$\Psi_{\mathrm{inf}}(\vec{r},t)=\frac{Sc}{(4\pi Dct)^{3/2}}\exp(-\frac{|\vec{r}-\overrightarrow{r'}|^2}{4Dct}-\mu_a ct) \tag{VI-11}$$

Where c is the speed of light in medium.

The flux term is parallel to the vector $(\vec{r}-\overrightarrow{r'})$ and expressed as:

$$\vec{J}_{inf}(\vec{r},t) = -D\nabla\Psi_{\text{inf}} = -D\frac{\partial\Psi_{\text{inf}}}{\partial \text{l}}\hat{l} \qquad \text{(VI-12)}$$

Where l=$|\vec{r}-\overrightarrow{r'}|$, and $\hat{l}$ is unity direction vector of l.

The radiance if expanded as the 1st order of spherical harmonic is expressed as

$$L(\overrightarrow{r},t,\hat{s}) = \Psi_{\text{inf}}(\vec{r},t) + \frac{3}{4\pi}\vec{J}_{inf}(\vec{r},t)\cdot\hat{s} \qquad \text{(VI-13)}$$

Now, let us consider the radiance at the interface between air and semi-infinite medium induced by an impulsive directional point source, which is the geometry of concern in this work as illustrated by Figure VI-2. We still adopt the master and slave dual-source configuration as used in steady-state modeling work, as represented as figure below.

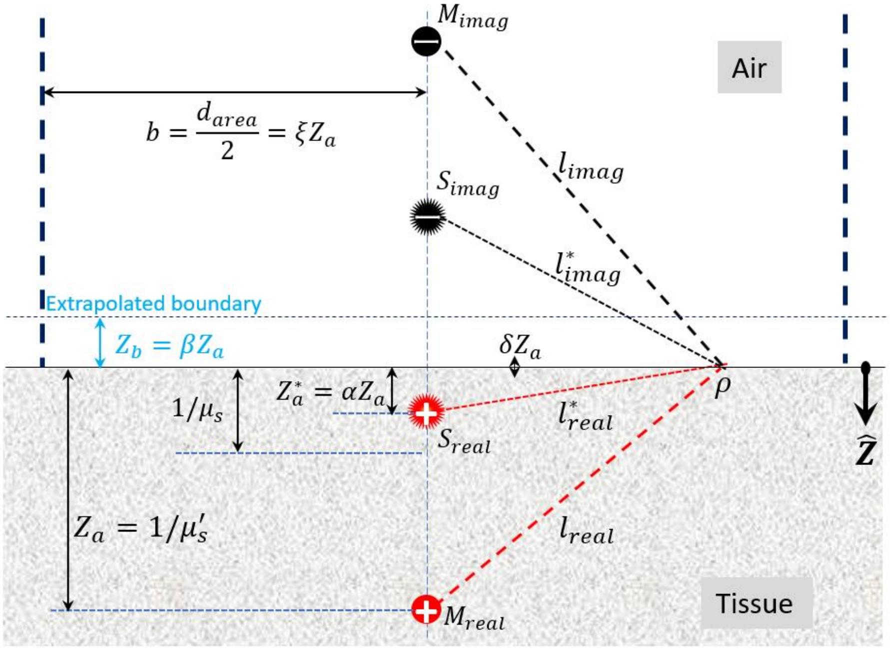

Figure VI-4 master and slave dual-source configuration for outer field

For the point illumination, a master-source [14] of intensity S=1 [unit: W·mm^{-3}] is set at a depth of $z_a = 1/\mu_s'$. A slave-source index is defined [14] as $\eta(g) = [g \cdot exp(1-g)]^{1/10}$. Then the slave-source is set at a depth of $z_a^* = (1-g)^2(1-\eta)z_a = \alpha z_a$ [unit: mm], and the intensity of the slave source is $S^* = \eta \cdot S \cdot exp\left[-\mu_{eff}\, z_a(1+\alpha)/2\right]$ [unit: W·mm^{-3}]. The medium-air boundary is accounted for by the extrapolated zero-boundary [15] that is set at a distance of $z_b = 2AD = \beta z_a$ [unit: mm] away from medium surface, where $A = (1+\xi)/(1-\xi)$, and $\xi = -1.44{n_{tiss}}^{-2} + 0.710{n_{tiss}}^{-1} +$ 0.668+0.0636n_{tiss}. For a position on the tissue-air interface of a distance of ρ [unit: mm] from the source, the following lengths [unit: mm] are defined:

$$\mathrm{l}_{\mathrm{real}}^{\mathrm{m}} = \sqrt{\rho^2 + \mathrm{z}_\mathrm{a}^2} \tag{VI-14}$$

$$\mathrm{l}_{\mathrm{imag}}^{\mathrm{m}} = \sqrt{\rho^2 + \mathrm{z}_\mathrm{a}^2(1+2\beta)^2} \tag{VI-15}$$

$$\mathrm{l}_{\mathrm{real}}^{\mathrm{s}} = \sqrt{\rho^2 + \mathrm{z}_\mathrm{a}^2\alpha^2} \tag{VI-16}$$

$$\mathrm{l}_{\mathrm{imag}}^{\mathrm{s}} = \sqrt{\rho^2 + \mathrm{z}_\mathrm{a}^2(\alpha+2\beta)^2} \tag{VI-17}$$

At extrapolated boundary $z = -z_b$, the Dirichlet Boundary Condition is met by real source and image source, both for master source and slave source.

$$\Psi_{\mathrm{semi}}(\rho,t) = \Psi_{inf}^{\mathrm{real}}(\rho,t) + \Psi_{inf}^{\mathrm{imag}}(\rho,t) \tag{VI-18}$$

The fluence rate contributed by master source are slave source are expressed as following two equations respectively:

$$\Psi_{\mathrm{semi}}^{\mathrm{m}} = \frac{Sc}{(4\pi Dct)^{3/2}}\exp(-\mu_a ct)\left[\exp\left(-\frac{(l_{real}^m)^2}{4Dct}\right) - \exp(-\frac{(l_{imag}^m)^2}{4Dct})\right] \tag{VI-19}$$

$$\Psi_{\mathrm{semi}}^{\mathrm{s}} = \frac{Sc}{(4\pi Dct)^{3/2}}\exp(-\mu_a ct)\left[\exp\left(-\frac{(l_{real}^s)^2}{4Dct}\right) - \exp(-\frac{(l_{imag}^s)^2}{4Dct})\right] \tag{VI-20}$$

The flux -z direction component that are contributed by master source are slave source, are expressed as following two equations respectively. See Appendix 9 for detailed derivation.

$$J_{semi}^{m}|_{-z}(\rho,t)=\frac{S}{2t(4\pi Dct)^{\frac{3}{2}}}\exp(-\mu_a ct)\,[z_a\exp\left(-\frac{(l_{real}^{m})^2}{4Dct}\right)+(z_a+2z_b)\exp\left(-\frac{(l_{imag}^{m})^2}{4Dct}\right)]$$

(VI-21)

$$J_{semi}^{s}|_{-z}(\rho,t)=\frac{S^*}{2t(4\pi Dct)^{\frac{3}{2}}}\exp(-\mu_a ct)\,[z_a^*\exp\left(-\frac{(l_{real}^{s})^2}{4Dct}\right)+(z_a^*+2z_b)\exp\left(-\frac{(l_{imag}^{s})^2}{4Dct}\right)]$$

(VI-22)

At last, the time-domain outer field model is expressed

$$\mathrm{R}_{\delta\rightarrow}(\rho,t)=\frac{1}{\sqrt{2}}[\frac{1}{4\pi}(\Psi_{\mathrm{semi}}^{\mathrm{m}}+\Psi_{\mathrm{semi}}^{\mathrm{s}})+\frac{3}{4\pi}(J_{semi}^{m}|_{-z}+J_{semi}^{s}|_{-z})] \quad \text{(VI-23)}$$

6.2.3 Time-domain total diffuse reflectance

a) Inner-field contribution

When radius of collection area b is less than δz_a, the total diffuse reflectance $I(d_{area},t)$ is solely dominated by inner-field model:

$$I_{0\leftrightarrow\mathrm{b}}(d_{area},t)=\int_0^{\xi \mathrm{z_a}}2\pi\rho\mathrm{R}_{\delta\rightarrow}(\rho,t)d\rho \quad \text{(VI-24)}$$

$$I_{0\leftrightarrow\mathrm{b}}(d_{area},t)=0.75^{g}10^{-(1+p_1\gamma)}(1-g)^{g}\exp(-\gamma)\frac{1}{1-p_2\gamma}\left(\frac{\xi}{1-g}\right)^{1-p_2\gamma}(\mu_a c)\exp(-\mu_a ct)$$

(VI-25)

When b is larger than δz_a, $I_{0\leftrightarrow\mathrm{b}}(d_{area},t)$ is contributed by both inner-field model and outer-field model.

$$I_{0\leftrightarrow\mathrm{b}}(d_{area},t)=\int_0^{\delta \mathrm{z_a}}2\pi\rho\mathrm{R}_{\leftarrow\delta}(\rho,t)d\rho+\int_{\delta \mathrm{z_a}}^{b}2\pi\rho\mathrm{R}_{\delta\rightarrow}(\rho,t)d\rho \quad \text{(VI-26)}$$

Decompose the outer-field contribution to four components corresponding to master fluence rate, slave fluence rate, master flux, and slave flux. We have $I_{0\leftrightarrow\mathrm{b}}(d_{area},t)$ in the form of

$$I_{0\leftrightarrow\mathrm{b}}(d_{area},t)=I_{0\leftrightarrow\delta\mathrm{z_a}}+I_{\delta z_a\leftrightarrow\mathrm{b}}^{\Psi}+I_{\delta z_a\leftrightarrow\mathrm{b}}^{\Psi^*}+I_{\delta z_a\leftrightarrow\mathrm{b}}^{\mathrm{JZ}}+I_{\delta z_a\leftrightarrow\mathrm{b}}^{\mathrm{JZ}^*} \quad \text{(VI-27)}$$

Among them, the inner-field component $I_{0\leftrightarrow\delta\mathrm{z_a}}$is,

$$I_{0\leftrightarrow\delta z_a} = 0.75^g 10^{-(1+p_1\gamma)}(1-g)^g \exp(-\gamma)\frac{1}{1-p_2\gamma}\left(\frac{\delta}{1-g}\right)^{1-p_2\gamma} \mu_a c\exp(-\mu_a ct) \quad \text{(VI-28)}$$

b) Master fluence rate component

Calculate it as the difference of two terms

$$I^{\Psi}_{\delta z_a\leftrightarrow b} = I^{\Psi}_{\delta z_a\leftrightarrow\infty} - I^{\Psi}_{b\leftrightarrow\infty} \quad \text{(VI-29)}$$

The first term is

$$I^{\Psi}_{\delta z_a\leftrightarrow\infty} = \frac{1}{2\sqrt{2}}\frac{Sc}{(4\pi Dct)^{3/2}}\exp(-\mu_a ct)\int_{\delta z_a}^{\infty}\left[\exp\left(-\frac{(l^m_{real})^2}{4Dct}\right) - \exp(-\frac{(l^m_{imag})^2}{4Dct})\right]\rho d\rho \quad \text{(VI-30)}$$

$$I^{\Psi}_{\delta z_a\leftrightarrow\infty} = \frac{1}{2\sqrt{2}}\frac{Sc}{(4\pi Dct)^{3/2}}\exp(-\mu_a ct)\int_{\delta z_a}^{\infty}\left[\exp\left(-\frac{\rho^2 + z_a^2}{4Dct}\right) - \exp(-\frac{\rho^2 + z_a^2(1+2\beta)^2}{4Dct})\right]\rho d\rho$$

(VI-31)

The indefinite integral is calculated as below, where k > 0.

$$\int \exp\left(-\frac{\rho^2 + k^2}{4Dct}\right)\rho d\rho = \frac{1}{2}\int \exp\left(-\frac{\rho^2 + k^2}{4Dct}\right)d(\rho^2 + k^2) = \frac{(-4Dct)}{2}\exp\left(-\frac{\rho^2 + k^2}{4Dct}\right) + C$$

(VI-32)

Apply above integral, we have

$$I^{\Psi}_{\delta z_a\leftrightarrow\infty} = \frac{1}{2\sqrt{2}}\frac{Sc}{(4\pi Dct)^{3/2}}\exp(-\mu_a ct)\ \frac{4Dct}{2}\left[\exp(-\frac{\rho^2 + z_a^2(1+2\beta)^2}{4Dct}) - \exp\left(-\frac{\rho^2 + z_a^2}{4Dct}\right)\right]\Big|^{\infty}_{\delta z_a}$$

$$= \frac{1}{2\sqrt{2}}\frac{Sc}{(4\pi Dct)^{3/2}}\exp(-\mu_a ct)\ \frac{4Dct}{2}\left[\exp\left(-\frac{(\delta z_a)^2 + z_a^2}{4Dct}\right) - \exp(-\frac{(\delta z_a)^2 + z_a^2(1+2\beta)^2}{4Dct})\right]$$

$$= \frac{1}{8\sqrt{2}\pi^{3/2}}\frac{Sc}{\sqrt{Dct}}\exp(-\mu_a ct)\ \left[\exp\left(-\frac{\delta^2+1}{4Dct}z_a^2\right) - \exp(-\frac{\delta^2+(1+2\beta)^2}{4Dct}z_a^2)\right] \quad \text{(VI-33)}$$

The second term could be easily found in same way by replacing δ with ξ in above derivation due to the definition $b = \xi z_a$.

$$I_{b\leftrightarrow\infty}^{\Psi} = \frac{1}{8\sqrt{2}\pi^{3/2}}\frac{Sc}{\sqrt{Dct}}\exp(-\mu_a ct)\ \left[\exp\left(-\frac{\xi^2+1}{4Dct}\mathrm{z}_\mathrm{a}^2\right) - \exp(-\frac{\xi^2+(1+2\beta)^2}{4Dct}\mathrm{z}_\mathrm{a}^2)\right] \tag{VI-34}$$

c) Slave fluence rate component

Same with the treatment on master fluence rate, we decompose it to two terms.

$$I_{\delta z_a\leftrightarrow \mathrm{b}}^{\Psi^*} = I_{\delta z_a\leftrightarrow\infty}^{\Psi^*} - I_{b\leftrightarrow\infty}^{\Psi^*} \tag{VI-35}$$

The first term is

$$I_{\delta z_a\leftrightarrow\infty}^{\Psi^*} = \frac{1}{2\sqrt{2}}\frac{S^* c}{(4\pi Dct)^{3/2}}\exp(-\mu_a ct)\int_{\delta\mathrm{z}_\mathrm{a}}^{\infty}\left[\exp\left(-\frac{\rho^2+\mathrm{z}_\mathrm{a}^2\alpha^2}{4Dct}\right) - \exp(-\frac{\rho^2+\mathrm{z}_\mathrm{a}^2(\alpha+2\beta)^2}{4Dct})\right]\rho\mathrm{d}\rho \tag{VI-36}$$

By comparing with the derivation demonstrated in master fluence rate component, we observe that essentially the integration type is same but with two differences, one for slave source intensity S^*, the other for slave source depth αz_a. This predicts that the result of slave fluence rate will take the following form:

$$I_{\delta z_a\leftrightarrow\infty}^{\Psi^*} = \frac{1}{8\sqrt{2}\pi^{3/2}}\frac{S^* c}{\sqrt{Dct}}\exp(-\mu_a ct)\ \left[\exp\left(-\frac{\delta^2+\alpha^2}{4Dct}\mathrm{z}_\mathrm{a}^2\right) - \exp(-\frac{\delta^2+(\alpha+2\beta)^2}{4Dct}\mathrm{z}_\mathrm{a}^2)\right] \tag{VI-37}$$

$$I_{b\leftrightarrow\infty}^{\Psi^*} = \frac{1}{8\sqrt{2}\pi^{3/2}}\frac{S^* c}{\sqrt{Dct}}\exp(-\mu_a ct)\ \left[\exp\left(-\frac{\xi^2+\alpha^2}{4Dct}\mathrm{z}_\mathrm{a}^2\right) - \exp(-\frac{\xi^2+(\alpha+2\beta)^2}{4Dct}\mathrm{z}_\mathrm{a}^2)\right] \tag{VI-38}$$

d) Master flux component

$$I_{\delta z_a\leftrightarrow \mathrm{b}}^{\mathrm{JZ}} = I_{\delta z_a\leftrightarrow\infty}^{\mathrm{JZ}} - I_{b\leftrightarrow\infty}^{\mathrm{JZ}} \tag{VI-39}$$

The first term is

$$\begin{aligned} I_{\delta z_a\leftrightarrow\infty}^{\mathrm{JZ}} &= \frac{3}{2\sqrt{2}}\frac{S}{2t(4\pi Dct)^{\frac{3}{2}}}\exp(-\mu_a ct)\int_{\delta\mathrm{z}_\mathrm{a}}^{\infty}[z_a\exp\left(-\frac{(l_{real}^m)^2}{4Dct}\right) + (z_a+2z_b)\exp\left(-\frac{(l_{imag}^m)^2}{4Dct}\right)]\,\rho\mathrm{d}\rho \\ &= \frac{3}{2\sqrt{2}}\frac{S}{2t(4\pi Dct)^{\frac{3}{2}}}\exp(-\mu_a ct)\int_{\delta\mathrm{z}_\mathrm{a}}^{\infty}[z_a\exp\left(-\frac{\rho^2+\mathrm{z}_\mathrm{a}^2}{4Dct}\right) + (z_a+2z_b)\exp\left(-\frac{\rho^2+\mathrm{z}_\mathrm{a}^2(1+2\beta)^2}{4Dct}\right)]\,\rho\mathrm{d}\rho \end{aligned} \tag{VI-40}$$

The indefinite integral is calculated as

$$\int\left[z_a \exp\left(-\frac{\rho^2+\mathrm{z}_\mathrm{a}^2}{4Dct}\right) + (z_a + 2z_b)\exp\left(-\frac{\rho^2+\mathrm{z}_\mathrm{a}^2(1+2\beta)^2}{4Dct}\right)\right]\rho d\rho$$

$$= \int z_a \exp\left(-\frac{\rho^2+\mathrm{z}_\mathrm{a}^2}{4Dct}\right)\rho d\rho + \int (z_a + 2z_b)\exp\left(-\frac{\rho^2+\mathrm{z}_\mathrm{a}^2(1+2\beta)^2}{4Dct}\right)\rho d\rho$$

$$= \frac{z_a}{2}(-4Dct)\exp\left(-\frac{\rho^2+\mathrm{z}_\mathrm{a}^2}{4Dct}\right) + \frac{(z_a+2z_b)}{2}(-4Dct)\exp\left(-\frac{\rho^2+\mathrm{z}_\mathrm{a}^2(1+2\beta)^2}{4Dct}\right) + C \qquad \text{(VI-41)}$$

Apply above definite integral result, we have the first term as

$$I^{\mathrm{JZ}}_{\delta z_a\leftrightarrow\infty} = \frac{3}{2\sqrt{2}}\frac{S}{2t(4\pi Dct)^{\frac{3}{2}}}\exp(-\mu_a ct)\left[\frac{z_a}{2}(4Dct)\exp\left(-\frac{\delta^2+1}{4Dct}\mathrm{z}_\mathrm{a}^2\right) + \frac{(z_a+2z_b)}{2}(4Dct)\exp\left(-\frac{\delta^2+(1+2\beta)^2}{4Dct}\mathrm{z}_\mathrm{a}^2\right)\right] \qquad \text{(VI-42)}$$

Rearrange it as

$$I^{\mathrm{JZ}}_{\delta z_a\leftrightarrow\infty} = \frac{3}{16\sqrt{2}\pi^{\frac{3}{2}}}\frac{S}{t(Dct)^{\frac{1}{2}}}\exp(-\mu_a ct)\left[z_a \exp\left(-\frac{\delta^2+1}{4Dct}\mathrm{z}_\mathrm{a}^2\right) + (z_a + 2z_b)\exp\left(-\frac{\delta^2+(1+2\beta)^2}{4Dct}\mathrm{z}_\mathrm{a}^2\right)\right] \qquad \text{(VI-43)}$$

Then the second term could be derived in parallel by replacing δ with ξ,

$$I^{\mathrm{JZ}}_{\xi z_a\leftrightarrow\infty} = \frac{3}{16\sqrt{2}\pi^{\frac{3}{2}}}\frac{S}{t(Dct)^{\frac{1}{2}}}\exp(-\mu_a ct)\left[z_a \exp\left(-\frac{\xi^2+1}{4Dct}\mathrm{z}_\mathrm{a}^2\right) + (z_a + 2z_b)\exp\left(-\frac{\xi^2+(1+2\beta)^2}{4Dct}\mathrm{z}_\mathrm{a}^2\right)\right] \qquad \text{(VI-44)}$$

e) Slave flux component

$$I^{\mathrm{JZ}^*}_{\delta z_a\leftrightarrow \mathrm{b}} = I^{\mathrm{JZ}^*}_{\delta z_a\leftrightarrow\infty} - I^{\mathrm{JZ}^*}_{b\leftrightarrow\infty} \qquad \text{(VI-45)}$$

With same principle demonstrated in deriving the slave fluence rate component, the slave flux component takes following form:

$$I_{\delta z_a\leftrightarrow\infty}^{\mathrm{JZ}^*}=\frac{3}{16\sqrt{2}\pi^{\frac{3}{2}}}\frac{S^*}{t(Dct)^{\frac{1}{2}}}\exp(-\mu_a ct)\left[z_a^*\exp\left(-\frac{\delta^2+\alpha^2}{4Dct}\mathrm{z}_\mathrm{a}^2\right)+(z_a^*+2z_b)\exp\left(-\frac{\delta^2+(\alpha+2\beta)^2}{4Dct}\mathrm{z}_\mathrm{a}^2\right)\right]$$

(VI-46)

$$I_{b\leftrightarrow\infty}^{\mathrm{JZ}^*}=\frac{3}{16\sqrt{2}\pi^{\frac{3}{2}}}\frac{S^*}{t(Dct)^{\frac{1}{2}}}\exp(-\mu_a ct)\left[z_a\exp\left(-\frac{\xi^2+\alpha^2}{4Dct}\mathrm{z}_\mathrm{a}^2\right)+(z_a+2z_b)\exp\left(-\frac{\xi^2+(\alpha+2\beta)^2}{4Dct}\mathrm{z}_\mathrm{a}^2\right)\right]$$

(VI-47)

To summarize, when $b \le \delta z_a$, the total diffuse reflectance in time-domain is

$$I_{0\leftrightarrow\mathrm{b}}(d_{area},t)=0.75^g 10^{-(1+p_1\gamma)}(1-g)^g\exp(-\gamma)\frac{1}{1-p_2\gamma}\left(\frac{\xi}{1-g}\right)^{1-p_2\gamma}\mu_a c\exp(-\mu_a ct) \quad \text{(VI-48)}$$

When $b > \delta z_a$, the total diffuse reflectance in time-domain is

$$I_{0\leftrightarrow\mathrm{b}}(d_{area},t)=I_{0\leftrightarrow\delta\mathrm{z}_\mathrm{a}}+\left[I_{\delta z_a\leftrightarrow\infty}^{\Psi}-I_{b\leftrightarrow\infty}^{\Psi}\right]+\left[I_{\delta z_a\leftrightarrow\infty}^{\Psi^*}-I_{b\leftrightarrow\infty}^{\Psi^*}\right]+\left[I_{\delta z_a\leftrightarrow\infty}^{\mathrm{JZ}}-I_{b\leftrightarrow\infty}^{\mathrm{JZ}}\right]+$$
$$[I_{\delta z_a\leftrightarrow\infty}^{\mathrm{JZ}^*}-I_{b\leftrightarrow\infty}^{\mathrm{JZ}^*}] \quad \text{(VI-49)}$$

6.2.4 Monte-Carlo simulation

Time-domain Monte-Carlo simulation has been performed on a 24-core Linux server by using the open source Monte Carlo Command Line (MCCL, v4.8.0Beta) application developed by Virtual Photonics. The same CIAC geometry illustrated in Figure VI-2 is used in simulation, where a directional point source sitting at the origin point (0,0,0) is injecting an impulse of photons into semi-infinite tissue medium along the positive z direction (0,0,1) and diffusely reflected photons are collected within a circular area with a radii $b = d_{area}/2$ measured from the origin point over a short span of collection time t_{mc}. A total of (M+1) spatial points and are linearly spaced between $\rho = [0, b]mm$, cutting the whole collection into N concentric element areas termed as spatial bins in monte-carlo. The area of m^{th} spatial bin is calculated as $\rho_{bin}(m) = [\pi\rho_{m+1}^2 - \pi\rho_m^2]$, where m is the integer index ranging from 1 to N, $\rho_1 = 0$ and $\rho_{M+1} = b$. Similarly, a total of (N+1) temporal points are linearly spaced between $t = [0, t_{mc}]$ns and cut the collection time into N element segments termed as temporal bins in monte-carlo. The length of each temporal is equal to same value of $t_{bin}(n) = t_{mc}/N$. Therefore, the time-domain spatially resolved diffuse reflectance $R(\rho_m, t_n)$

(unit : $ns^{-1}mm^{-1}$) generated from MC simulation has 2-dimension distribution over M spatial bins by N temporal bins, which is defined as the density of diffuse reflectance at a 2D time-domain Bin $Bin_{td} = \rho_{bin}(m)t_{bin}(n)$.

The time-domain total diffuse reflectance collected via $d_{area} = 2b = 2\rho_{M+1}$ at the temporal moment $t = t_n$, can be calculated by integrating $R(\rho_m, t_n)$ over the spatial dimension, as shown in following equation.

$$I(d_{area}, t_n) = \sum_{m=1}^{M} R(\rho_m, t_n) \times [\pi(\rho_{m+1})^2 - \pi(\rho_m)^2] \qquad \text{(VI-50)}$$

$I(d_{area}, t_n)$ has a unit of $1/ns$, which means the power of total diffuse reflectance collected via d_{area} at the moment $t = t_n$.

6.3 Results and Discussion

6.3.1 Model dependency on reduced scattering coefficient

Figure VI-5 presents the temporal total diffuse reflectance collected via $d_{area} = 1mm^{-1}$ at three different reduced scattering coefficients $\mu_s' = [0.1, 1.0, 10]mm^{-1}$ representing weak, typical and strong scattering mediums. The absorption coefficient $\mu_a = 1mm^{-1}$ and anisotropy factor g = 0.9, typical for biological tissue, are kept same for all three cases. The black solid line in the figure represents the model-predicted temporal total diffuse reflectance, and the discrete markers represent MC simulated results. From Part (A) that plots the time axis in linear scale, we could observe that after injection of light impulse, total diffuse reflectance drops down very sharply within the first 0.1nanosecond approximately, and decreases more and more slowly as time goes. Our model predicts the same change trend as well as a good match with MC simulated results. To look closely at the characteristics in the first 0.1ns. we display the time axis in logarithm scale in part (B). MC data shows that the total diffuse reflectance reaches a summit in the first 3 picoseconds after the impulse inject, and from this peak, it starts to drop down sharply as observed before. In weaker scattering medium, this summit shows up later than stronger scattering case. Our model does not quantify the summit feature well, especially when scattering is weak.

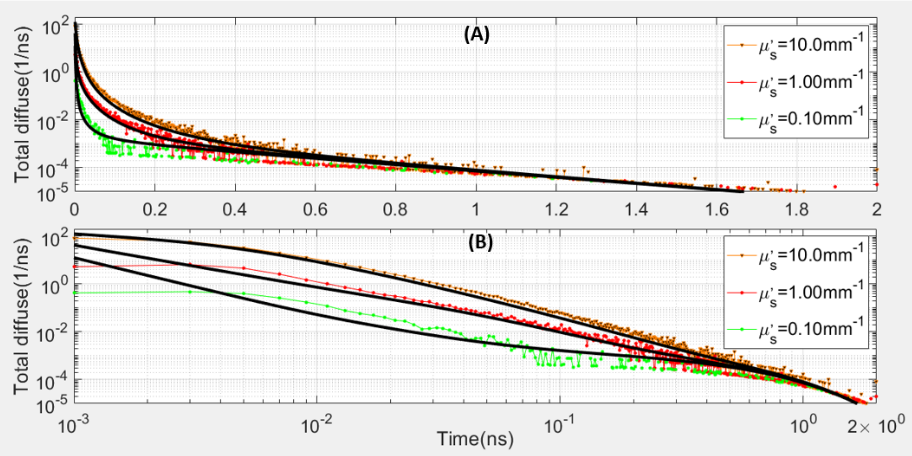

Figure VI-5 temporal total diffuse reflectance at different reduced scattering coefficients

The photons that arrives earlier have shorter path length when propagating inside tissue, which are mainly collected from the area close to incident point. These early arrival photons normally undergo larger angle scattering events. The photons that arrives relatively later have longer path length inside tissue, which are mainly contributed from the area with larger source-detector distance.

6.3.2 Model dependency on absorption coefficient

Figure VI-6 presents the temporal total diffuse reflectance collected via $d_{area} = 1mm^{-1}$ at four different reduced scattering coefficients $\mu_a = [0.001, 0.01, 0.1, 1.0]mm^{-1}$. The reduced scattering coefficient $\mu_s' = 1mm^{-1}$ and anisotropy factor g = 0.9 are chosen based on their typical value for biological tissue. Part (A) displays time axis in linear scale and part (B) display the same data in logarithm scale. As expected, temporal total diffuse reflectance presents the same decreasing trend as time goes, and the stronger the absorption, the faster it drops. It is observed that our model matches MC simulated result well generally. In stronger absorption case of $\mu_a = 1mm^{-1}$, our model does not quantify the later arrival photon well.

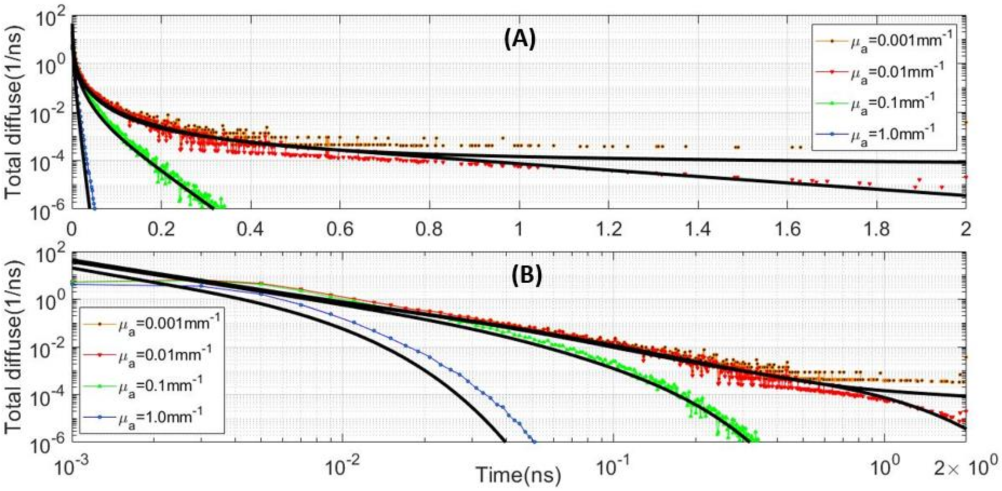

Figure VI-6 temporal total diffuse reflectance at different absorption coefficients

6.3.3 Model dependency on anisotropy factor g

Figure VI-7 presents temporal total diffuse reflectance collected via $d_{area} = 1mm^{-1}$ at 6 different anisotropy factor g = [0.5, 0.6, 0.7, 0.8, 0.9, 0.95]. The reduced scattering coefficient $\mu_s' = 1mm^{-1}$ and absorption coefficient $\mu_a = 0.01mm^{-1}$ are chosen based on their typical value for biological tissue. Since only subtle difference are observed among 6 cases with different g values, we present the MC simulated results in part (A) and part (C), and model-predicted results in part (B) and (D), and display time axis in linear scale in part (A) and (B), and display time axis in logarithm scale in part (C) and (D).

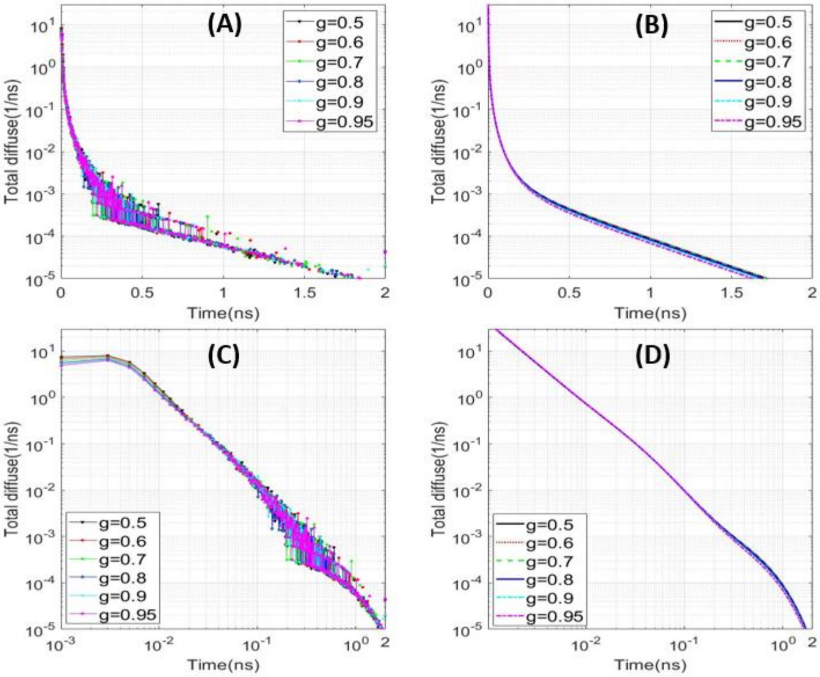

Figure VI-7 temporal total diffuse reflectance at different anisotropy factor values

From MC results, it is observed from MC data that the effect of different g on total diffuse reflectance is small and become visible in the first 0.02 nanosecond when both X axis and Y axis are zoomed in logarithm scale, especially during the first 3 picoseconds when total diffuse reflectance reaches summit. During t > 0.1 nanosecond, as the collected photons become less and less, and effect of random noise in MC simulation also becomes severe, it is hard to visually observe the effect of anisotropy and is also hard to judge whether it exists or not. As observed in part (B) and part (D), during the time duration very close to incident moment, our model cannot quantify the summit feature, but our model predicts that the photons arriving in later time displays the difference caused by anisotropy factor. Since early arrival photons are mainly collected via area close to incident point due to large angle scattering event, the smaller anisotropy factor which represents larger probability of larger angle scattering, will reveal larger amounts of photons at early time, particularly the first 0.02 nanosecond.

6.3.4 Model dependency on collection area

Figure VI-8 presents the total diffuse reflectance collected at different d_{area} at same temporal moment t = 0.01 nanosecond to evaluate model's dependency on size of collection area. The tissue properties are set as below: reduced scattering coefficient $\mu_s' = 1mm^{-1}$, absorption coefficient $\mu_a = 0.01mm^{-1}$, anisotropy g = 0.9. The connected green markers represent MC results that is calculated by integrating $R(\rho_m, t_n)$ over different size of collection area, while the black solid line represents our model predicted results.

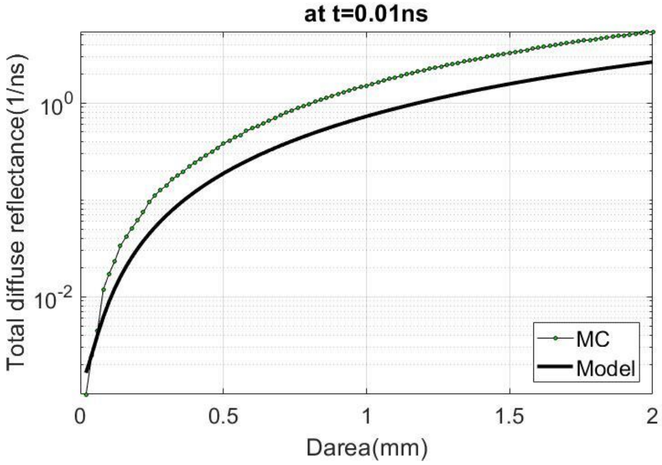

Figure VI-8 total diffuse reflectance collected at t = 0.01ns against different size of collection area

It is observed that out model predicts the correct trend as collection area increases, but also tends to over-estimate the total diffuse reflectance compared with MC results. And the deviation tends to increase as d_{area} increases.

6.4 Summary

This work demonstrated the first analytical model for time-domain single-fiber diffuse reflectance spectroscopy. By comparing with MC simulated data in various condition, our model could predicts the correct temporal changing pattern under conditions of different tissue scattering, absorption and anisotropy g as well as different collection area. Though still having difficulty in quantify summit feature during the first 3 picoseconds, our model generally matches MC results in most conditions evaluated in this work, which proves the correctness of our methodology used in developing time-domain model. It also indicates that our current time-domain still need to be further refined. Currently the dimension border point δ is set as 0.005, we may need update it when we further adjust inner-field model to meet Monte-Carlo predicted results

CHAPTER VII

FINAL REMARKS

7.1 Contributions of this work

This work develops analytically-driven models of total diffuse reflectance of single fiber reflectance spectroscopy (SfRS) measurement in steady-state and time-domain, and demonstrates a few methods that are new to the modeling of diffuse reflectance at the scales relevant to SfRS: (1) concatenate two models of spatially-resolved diffuse reflectance to construct one effective model based on center illumination and area collection geometries that works at a reduced scattering pathlength scaled dimension as small as 10^{-5}. (2) Derive the total diffuse reflectance by integrating the spatially resolved diffuse reflectance over the entire area of collection. The analytically arrived steady-state model of total diffuse reflectance, as validated by Monte-Carlo simulations and phantom experiment, could potentially provide more robust tissue properties recovering than existing empirical model in practical use. In addition, for the first time, it offers transparent understanding about three steady-state patterns previously observed as well as accurate quantification of the saturation level and transition point. The modeling methodology developed in steady-state work is also extended to the development of time-domain model and renders the first analytical description of time-domain features of SfRS measurement, which will power more clinical application with time-domain SfRS.

The modeling methodology demonstrated in steady-state and time-domain opens the potential of being transferred to frequency-domain SfRS and fluorescence SfRS.

7.2 Future work

The intended future work includes following directions:

1) Refine current time-domain model of SfRS

The time-domain model developed in Chapter VI reveals correct temporal patterns and model dependency on scattering, absorption and collection area. However, our current model does not quantify the summit feature observed during the first 3 picoseconds. In a lower scattering medium, our model shows deviation from MC simulated data during earlier time of collection. These issues may be addressed by further refining our inner-field model component through comparing with MC results simulated in broader range of tissue properties. The current time-domain simulation launches 1 million photons into tissue medium, but to make the later arrival photons more visible, more than 1 million photons per simulation may be needed.

2) Model the average optical path length of a single fiber probe

The time-domain MC present the temporal total diffuse reflectance collected via a circular area. The arrival time t_m uniquely corresponds to the optical path length that the photon travels inside tissue before being collected, e.g. for photons that arrives at t = t_m, their path length is calculated as $l_m = ct_m$. Then the average optical path length can be calculated as the weighted mean of l_m, as shown in equation below, where the weight is defined as number of photons collected over d_{area} at TimeBin(m) divided by total number of photons collected over d_{area} from t = 0 up to t = infinite, and M is a large integer number set in MC simulation to numerically emulate t= infinite.

$$L_{MC} = \sum_{m=1}^{M} \frac{I(d_{area}, t=[t_m, t_m+\Delta t])}{I(d_{area}, t=[0, M\Delta t])} \times (ct_m) \qquad \text{(VII-1)}$$

The model-predicted average optical path length could be calculated by using modified Beer-Lambert Law, as shown in following equation (VII-2), or by directly deriving from time-domain model as shown in equation (VII-3).

$$L_{Model} = -\frac{ln(I/I_{scat})}{\mu_a} \tag{VII-2}$$

$$L_{Model} = \int_0^{d_{area}/2} 2\pi\rho[\int_0^{\infty} R_{td}(\rho,t)(ct)dt]d\rho \tag{VII-3}$$

3) Transfer modeling methodology to frequency-domain SfRS configuration and fluorescence steady-state SfRS

The same modeling methodology demonstrated in steady-state and time-domain work could be applied to frequency-domain SfRS and fluorescence steady-state SfRS where the model or analytical understanding of observed feature is still blank.

4) Develop graphic user interface provide convenient use of our models for data-fitting

Compared with empirical model, diffusion-based analytical model usually possesses a bulky form. To provides convenience use of our models in their data-fitting tasks, it is worth to encapsulate our models into easy-to-use graphic user interface (GUI) and widely publish them online. Matlab Live Script will be our first choice to this GUI development due to its highly flexibility and easy deployment. Live scripts contain output and graphics with the code that produced them, together in a single interactive environment called the Live Editor. The GUI will be designed to allow user to upload reflectance spectrums and fiber specifications, and extract absorption spectrum $\mu_a(\lambda)$ and scattering spectrum $\mu_s'(\lambda)$ through data-fitting with our models.

REFERENCES

1. Wang, L.V. and H.-i. Wu, *Biomedical optics: principles and imaging*. 2012: John Wiley & Sons.
2. Kanick, S., et al., *Measurement of the reduced scattering coefficient of turbid media using single fiber reflectance spectroscopy: fiber diameter and phase function dependence.* Biomedical optics express, 2011. **2**(6): p. 1687-1702.
3. Hariri Tabrizi, S., et al., *Comparison between performance of single-fiber reflectance spectroscopy (SFRS) system and colposcopy: a phase III trial.* Lasers in Medical Science, 2017. **32**(9): p. 2139-2144.
4. Yu, L. and K. Murari. *Design of a single-fiber, wavelength-resolved system for monitoring deep tissue oxygenation*. in *Engineering in Medicine and Biology Society (EMBC), 2014 36th Annual International Conference of the IEEE*. 2014. IEEE.
5. Amelink, A., T. Christiaanse, and H.J.C.M. Sterenborg, *Effect of hemoglobin extinction spectra on optical spectroscopic measurements of blood oxygen saturation.* Optics Letters, 2009. **34**(10): p. 1525-1527.
6. Denkçeken, T., et al., *Elastic light single-scattering spectroscopy for the detection of cervical precancerous ex vivo.* IEEE Transactions on Biomedical Engineering, 2013. **60**(1): p. 123-127.
7. Rajaram, N., et al., *Experimental validation of the effects of microvasculature pigment packaging on in vivo diffuse reflectance spectroscopy.* Lasers Surg Med, 2010. **42**(7): p. 680-8.
8. Piao, D., et al., *In vivo assessment of diet-induced rat hepatic steatosis development by percutaneous single-fiber spectroscopy detects scattering spectral changes due to fatty infiltration.* Journal of biomedical optics, 2015. **20**(11): p. 117002.
9. Piao, D., et al., *In vivo percutaneous reflectance spectroscopy of fatty liver development in rats suggests that the elevation of the scattering power is an early indicator of hepatic steatosis.* Journal of Innovative Optical Health Sciences, 2018: p. 1850019.
10. Yu, L., et al., *In-vivo monitoring of tissue oxygen saturation in deep brain structures using a single fiber optical system.* Biomedical Optics Express, 2016. **7**(11): p. 4685-4694.
11. Piao, D., et al., *A low-cost needle-based single-fiber reflectance spectroscopy method to probe scattering changes associated with mineralization in intervertebral discs in chondrodystrophoid canine species – A pilot study.* Photonics & Lasers in Medicine, 2012. **1**(2).
12. Sun, T., et al. *Orthotopic AY-27 rat bladder urothelial cell carcinoma model presented an elevated methemoglobin proportion in the increased total hemoglobin content when evaluated in vivo by single-fiber reflectance spectroscopy*. in *Therapeutics and Diagnostics in Urology: Lasers, Robotics, Minimally Invasive, and Advanced Biomedical Devices*. 2017. International Society for Optics and Photonics.

13. Canpolat, M. and J.R.J.A.O. Mourant, *Particle size analysis of turbid media with a single optical fiber in contact with the medium to deliver and detect white light.* 2001. **40**(22): p. 3792-3799.
14. Piao, D., et al., *Percutaneous single-fiber reflectance spectroscopy of canine intervertebral disc: is there a potential for in situ probing of mineral degeneration?* Lasers Surg Med, 2014. **46**(6): p. 508-19.
15. Tabrizi, S.H., et al., *Single fiber reflectance spectroscopy on cervical premalignancies: the potential for reduction of the number of unnecessary biopsies.* Journal of Biomedical Optics, 2013. **18**(1): p. 017002.
16. Stegehuis, P.L., et al. *Toward optical guidance during endoscopic ultrasound-guided fine needle aspirations of pancreatic masses using single fiber reflectance spectroscopy: a feasibility study*. 2017. SPIE.
17. Alerstam, E., et al., *Single-fiber diffuse optical time-of-flight spectroscopy.* Optics letters, 2012. **37**(14): p. 2877-2879.
18. Kanick, S.C., et al., *Monte Carlo analysis of single fiber reflectance spectroscopy: photon path length and sampling depth.* Phys Med Biol, 2009. **54**(22): p. 6991-7008.
19. Kanick, S.C., H.J. Sterenborg, and A. Amelink, *Empirical model of the photon path length for a single fiber reflectance spectroscopy device.* Opt Express, 2009. **17**(2): p. 860-71.
20. Gamm, U., et al., *Measurement of tissue scattering properties using multi-diameter single fiber reflectance spectroscopy: in silico sensitivity analysis.* Biomedical optics express, 2011. **2**(11): p. 3150-3166.
21. Kanick, S.C., et al. *Integration of single-fiber reflectance spectroscopy into ultrasound-guided endoscopic lung cancer staging of mediastinal lymph nodes*. 2010. SPIE.
22. Piao, D., et al., *Percutaneous single ‐ fiber reflectance spectroscopy of canine intervertebral disc: Is there a potential for in situ probing of mineral degeneration?* Lasers in surgery and medicine, 2014. **46**(6): p. 508-519.
23. Piao, D., *Single-Fiber Reflectance Spectroscopy of Isotropic-Scattering Medium: An Analytic Perspective to the Ratio-of-Remission in Steady-State Measurements.* 2014.
24. Seo, I., C.K. Hayakawa, and V. Venugopalan, *Radiative transport in the delta-P1 approximation for semi-infinite turbid media.* Med Phys, 2008. **35**(2): p. 681-93.
25. Shendeleva, M.L., *Single-scattering solutions to radiative transfer in infinite turbid media.* JOSA A, 2013. **30**(11): p. 2169-2174.
26. Vitkin, E., et al., *Photon diffusion near the point-of-entry in anisotropically scattering turbid media.* Nature communications, 2011. **2**: p. 587.
27. Farrell, T.J., M.S. Patterson, and B. Wilson, *A diffusion theory model of spatially resolved, steady ‐ state diffuse reflectance for the noninvasive determination of tissue optical properties in vivo.* Medical physics, 1992. **19**(4): p. 879-888.
28. Piao, D. and S. Patel, *Simple empirical master–slave dual-source configuration within the diffusion approximation enhances modeling of spatially resolved diffuse reflectance at short-path and with low scattering from a semi-infinite homogeneous medium.* Applied Optics, 2017. **56**(5): p. 1447.
29. Xu, M., *Diagnosis of the phase function of random media from light reflectance.* Scientific reports, 2016. **6**: p. 22535.
30. Zhu, C. and Q.J.J.o.b.o. Liu, *Review of Monte Carlo modeling of light transport in tissues.* 2013. **18**(5): p. 050902.

31. Zonios, G. and A. Dimou, *Modeling diffuse reflectance from homogeneous semi-infinite turbid media for biological tissue applications: a Monte Carlo study.* Biomedical Optics Express, 2011. **2**(12): p. 3284-3294.
32. Kanick, S.C., et al., *Integration of single-fiber reflectance spectroscopy into ultrasound-guided endoscopic lung cancer staging of mediastinal lymph nodes.* Journal of biomedical optics, 2010. **15**(1): p. 017004.
33. Gamm, U.A., et al. *Measurements of tissue scattering properties using multi-diameter single fiber reflectance spectroscopy: experimental validation*. in *Biomedical Optics and 3-D Imaging*. 2012. Miami, Florida: Optical Society of America.
34. Kanick, S.C., et al., *Method to quantitate absorption coefficients from single fiber reflectance spectra without knowledge of the scattering properties.* Optics letters, 2011. **36**(15): p. 2791-2793.
35. Kanick, S.C., et al., *Method to quantitatively estimate wavelength-dependent scattering properties from multidiameter single fiber reflectance spectra measured in a turbid medium.* Optics letters, 2011. **36**(15): p. 2997-2999.
36. Chen, Y.-W., et al., *Artificial neural networks for retrieving absorption and reduced scattering spectra from frequency-domain diffuse reflectance spectroscopy at short source-detector separation.* Biomedical optics express, 2016. **7**(4): p. 1496-1510.
37. Chen, Y.-W. and S.-H. Tseng, *Efficient construction of robust artificial neural networks for accurate determination of superficial sample optical properties.* Biomedical optics express, 2015. **6**(3): p. 747-760.
38. Tsui, S.-Y., et al., *Modelling spatially-resolved diffuse reflectance spectra of a multi-layered skin model by artificial neural networks trained with Monte Carlo simulations.* Biomedical Optics Express, 2018. **9**(4): p. 1531-1544.
39. Gamm, U., et al., *Quantification of the reduced scattering coefficient and phase-function-dependent parameter γ of turbid media using multidiameter single fiber reflectance spectroscopy: experimental validation.* Optics letters, 2012. **37**(11): p. 1838-1840.
40. van Leeuwen-van Zaane, F., et al., *In vivo quantification of the scattering properties of tissue using multi-diameter single fiber reflectance spectroscopy.* Biomedical Optics Express, 2013. **4**(5): p. 696-708.
41. Siegel, R.L., K.D. Miller, and A. Jemal, *Cancer statistics, 2015.* CA Cancer J Clin, 2015. **65**(1): p. 5-29.
42. Satoh, E., et al., *Prediction of muscle invasion of bladder cancer by cystoscopy.* Eur Urol, 2002. **41**(2): p. 178-81.
43. Klan, R., V. Loy, and H. Huland, *Residual tumor discovered in routine second transurethral resection in patients with stage T1 transitional cell carcinoma of the bladder.* J Urol, 1991. **146**(2): p. 316-8.
44. Lundbeck, F., F. Jacobsen, and M. Vaeth, *Impact of the category of early tumor recurrence on tumor progression in bladder tumors treated by transurethral resection.* Eur Urol, 1989. **16**(4): p. 291-4.
45. Hall, R.R. and G.R. Prout, *Staging of bladder cancer: is the tumor, node, metastasis system adequate?* Semin Oncol, 1990. **17**(5): p. 517-23.
46. Tuffaha, H., G.L. Shaw, and T. Briggs, *Augmented cecal mucosa appears pink under hexylaminolevulinate "blue light" fluorescence cystoscopy.* J Endourol, 2010. **24**(6): p. 943-4.
47. Geavlete, B., et al., *[Hexvix induced fluorescence blue light cystoscopy--a new perspective in superficial bladder tumors diagnosis].* Chirurgia (Bucur), 2008. **103**(5): p. 559-64.
48. Muggia, F.M., *Doxorubicin-polymer conjugates: further demonstration of the concept of enhanced permeability and retention.* Clin Cancer Res, 1999. **5**(1): p. 7-8.

49. Jesser, C.A., et al., *High resolution imaging of transitional cell carcinoma with optical coherence tomography: feasibility for the evaluation of bladder pathology.* Br J Radiol, 1999. **72**(864): p. 1170-6.
50. Palmer, G.M., et al., *Comparison of multiexcitation fluorescence and diffuse reflectance spectroscopy for the diagnosis of breast cancer (March 2003).* IEEE Trans Biomed Eng, 2003. **50**(11): p. 1233-42.
51. Jobsis, F.F., *Noninvasive, infrared monitoring of cerebral and myocardial oxygen sufficiency and circulatory parameters.* Science, 1977. **198**(4323): p. 1264-7.
52. Kienle, A., et al., *Spatially resolved absolute diffuse reflectance measurements for noninvasive determination of the optical scattering and absorption coefficients of biological tissue.* Appl Opt, 1996. **35**(13): p. 2304-14.
53. Keller, M.D., et al., *Autofluorescence and diffuse reflectance spectroscopy and spectral imaging for breast surgical margin analysis.* Lasers Surg Med, 2010. **42**(1): p. 15-23.
54. Sharma, V., et al., *Auto-fluorescence lifetime and light reflectance spectroscopy for breast cancer diagnosis: potential tools for intraoperative margin detection.* Biomed Opt Express, 2012. **3**(8): p. 1825-40.
55. Kennedy, S., et al., *Optical breast cancer margin assessment: an observational study of the effects of tissue heterogeneity on optical contrast.* Breast Cancer Res, 2010. **12**(6): p. R91.
56. Nilsson, J.H., et al., *Diffuse Reflectance Spectroscopy for Surface Measurement of Liver Pathology.* Eur Surg Res, 2017. **58**(1-2): p. 40-50.
57. Donoso, M. and E.S. Ghaly, *Prediction of drug dissolution from tablets using near-infrared diffuse reflectance spectroscopy as a nondestructive method.* Pharm Dev Technol, 2004. **9**(3): p. 247-63.
58. de Oliveira, G.A., et al., *Comparison of NIRS approach for prediction of internal quality traits in three fruit species.* Food Chemistry, 2014. **143**: p. 223-230.
59. Katsev, I.L., et al., *Efficient technique to determine backscattered light power for various atmospheric and oceanic sounding and imaging systems.* Journal of the Optical Society of America a-Optics Image Science and Vision, 1997. **14**(6): p. 1338-1346.
60. Yu, L., et al., *In-vivo monitoring of tissue oxygen saturation in deep brain structures using a single fiber optical system.* Biomed Opt Express, 2016. **7**(11): p. 4685-4694.
61. Koenig, F., et al., *Spectroscopic measurement of diffuse reflectance for enhanced detection of bladder carcinoma.* Urology, 1998. **51**(2): p. 342-5.
62. Goel, U.O., et al., *Feasibility of quantitative diffuse reflectance spectroscopy for targeted measurement of renal ischemia during laparoscopic partial nephrectomy.* J Biomed Opt, 2014. **19**(10): p. 107001.
63. Greening, G.J., et al., *Fiber-bundle microendoscopy with sub-diffuse reflectance spectroscopy and intensity mapping for multimodal optical biopsy of stratified epithelium.* Biomed Opt Express, 2015. **6**(12): p. 4934-50.
64. Zonios, G. and A. Dimou, *Modeling diffuse reflectance from homogeneous semi-infinite turbid media for biological tissue applications: a Monte Carlo study.* Biomed Opt Express, 2011. **2**(12): p. 3284-94.
65. Post, A.L., et al., *Modeling subdiffusive light scattering by incorporating the tissue phase function and detector numerical aperture.* Journal of Biomedical Optics, 2017. **22**(5).
66. Vitkin, E., et al., *Photon diffusion near the point-of-entry in anisotropically scattering turbid media.* Nat Commun, 2011. **2**: p. 587.
67. Liemert, A. and A. Kienle, *Exact and efficient solution of the radiative transport equation for the semi-infinite medium.* Sci Rep, 2013. **3**: p. 2018.

68. Gamm, U.A., et al., *Measurement of tissue scattering properties using multi-diameter single fiber reflectance spectroscopy: in silico sensitivity analysis.* Biomed Opt Express, 2011. **2**(11): p. 3150-66.
69. Kanick, S.C., et al., *Method to quantitate absorption coefficients from single fiber reflectance spectra without knowledge of the scattering properties.* Opt Lett, 2011. **36**(15): p. 2791-3.
70. van Leeuwen-van Zaane, F., et al., *In vivo quantification of the scattering properties of tissue using multi-diameter single fiber reflectance spectroscopy.* Biomed Opt Express, 2013. **4**(5): p. 696-708.
71. Hariri Tabrizi, S., et al., *Single fiber reflectance spectroscopy on cervical premalignancies: the potential for reduction of the number of unnecessary biopsies.* J Biomed Opt, 2013. **18**(1): p. 17002.
72. Kanick, S.C., et al., *Integration of single-fiber reflectance spectroscopy into ultrasound-guided endoscopic lung cancer staging of mediastinal lymph nodes.* J Biomed Opt, 2010. **15**(1): p. 017004.
73. Stegehuis, P.L., et al., *Toward optical guidance during endoscopic ultrasound-guided fine needle aspirations of pancreatic masses using single fiber reflectance spectroscopy: a feasibility study.* J Biomed Opt, 2017. **22**(2): p. 24001.
74. Zhang, X.U., et al., *Single fiber reflectance spectroscopy calibration.* Journal of Biomedical Optics, 2017. **22**(10).
75. Bargo, P.R., S.A. Prahl, and S.L. Jacques, *Collection efficiency of a single optical fiber in turbid media.* Applied Optics, 2003. **42**(16): p. 3187-3197.
76. Zemp, R.J., *Phase-function corrected diffusion model for diffuse reflectance of a pencil beam obliquely incident on a semi-infinite turbid medium.* J Biomed Opt, 2013. **18**(6): p. 067005.
77. Hollmann, J.L. and L.V. Wang, *Multiple-source optical diffusion approximation for a multilayer scattering medium.* Appl Opt, 2007. **46**(23): p. 6004-9.
78. Jia, M., et al., *Virtual-source diffusion approximation for enhanced near-field modeling of photon-migration in low-albedo medium.* Opt Express, 2015. **23**(2): p. 1337-52.
79. Bevilacqua, F. and C. Depeursinge, *Monte Carlo study of diffuse reflectance at source-detector separations close to one transport mean free path.* Journal of the Optical Society of America a-Optics Image Science and Vision, 1999. **16**(12): p. 2935-2945.
80. Piao, D.Q. and S. Patel, *Simple empirical master-slave dual-source configuration within the diffusion approximation enhances modeling of spatially resolved diffuse reflectance at short-path and with low scattering from a semi-infinite homogeneous medium.* Applied Optics, 2017. **56**(5): p. 1447-1452.
81. Xu, M., *Diagnosis of the phase function of random media from light reflectance.* Sci Rep, 2016. **6**: p. 22535.
82. Jacques, S.L. and S.A. Prahl, *Modeling Optical and Thermal Distributions in Tissue during Laser Irradiation.* Lasers in Surgery and Medicine, 1987. **6**(6): p. 494-503.
83. Haskell, R.C., et al., *Boundary-Conditions for the Diffusion Equation in Radiative-Transfer.* Journal of the Optical Society of America a-Optics Image Science and Vision, 1994. **11**(10): p. 2727-2741.
84. Farrell, T.J., M.S. Patterson, and B. Wilson, *A diffusion theory model of spatially resolved, steady-state diffuse reflectance for the noninvasive determination of tissue optical properties in vivo.* Med Phys, 1992. **19**(4): p. 879-88.
85. Piao, D., et al., *Effects of capsule on surface diffuse reflectance spectroscopy of the subcapsular parenchyma of a solid organ.* J Biomed Opt, 2018. **23**(12): p. 1-23.

86. Kanick, S.C., et al., *Measurement of the reduced scattering coefficient of turbid media using single fiber reflectance spectroscopy: fiber diameter and phase function dependence.* Biomed Opt Express, 2011. **2**(6): p. 1687-702.
87. Yariv, I., H. Duadi, and D. Fixler, *Optical method to extract the reduced scattering coefficient from tissue: theory and experiments.* Opt Lett, 2018. **43**(21): p. 5299-5302.
88. Groenhuis, R.A., J.J. Ten Bosch, and H.A. Ferwerda, *Scattering and absorption of turbid materials determined from reflection measurements. 2: measuring method and calibration.* Appl Opt, 1983. **22**(16): p. 2463-7.
89. Shendeleva, M.L., *Single-scattering solutions to radiative transfer in infinite turbid media.* J Opt Soc Am A Opt Image Sci Vis, 2013. **30**(11): p. 2169-74.
90. Shutic, S., et al., *Forensic identification of pharmaceuticals via portable X-ray fluorescence and diffuse reflectance spectroscopy.* Forensic science international, 2017. **279**: p. 22-32.
91. Hu, J., et al., *Rapid evaluation of the quality of chestnuts using near-infrared reflectance spectroscopy.* Food chemistry, 2017. **231**: p. 141-147.
92. Hu, W., et al., *Nondestructive detection of underlying moldy lesions of apple using frequency domain diffuse optical tomography.* Postharvest Biology and Technology, 2019. **153**: p. 31-42.
93. Zonios, G. and A. Dimou, *Modeling diffuse reflectance from semi-infinite turbid media: application to the study of skin optical properties.* Opt Express, 2006. **14**(19): p. 8661-74.
94. Mantis, G. and G. Zonios, *Simple two-layer reflectance model for biological tissue applications.* Applied optics, 2009. **48**(18): p. 3490-3496.
95. Sandell, J.L. and T.C.J.J.o.b. Zhu, *A review of in‐vivo optical properties of human tissues and its impact on PDT.* 2011. **4**(11‐12): p. 773-787.
96. Zhang, Q., et al., *A near-infrared calibration method suitable for quantification of broadband data in humans.* Journal of neuroscience methods, 2010. **188**(2): p. 181-186.

APPENDICES

APPENDIX A: Evaluation of the second term of Eq. (III.12) with respect to the first term

How much the second term of Eq. (III.12) affects the radial diffuse reflectance in comparison to the first term is assessed as shown in Fig.A1 over the following ranges: ($\mu_s'\rho$)=[10^{-5} 10^{0}], g=[0.5, 0.6, 0.7, 0.8, 0.9, 0.95] at μ_s' =1 mm^{-1} and μ_a =[0.001, 0.01. 0.1, 1]mm^{-1}. One example corresponding to μ_a=0.01 mm^{-1} and g=0.9 is shown in Fig. A-1. The maximal contribution of the second term to the radial diffuse reflectance over the range of ($\mu_s'\rho$)=[10^{-5} 10^{-1}] is less than 2%.

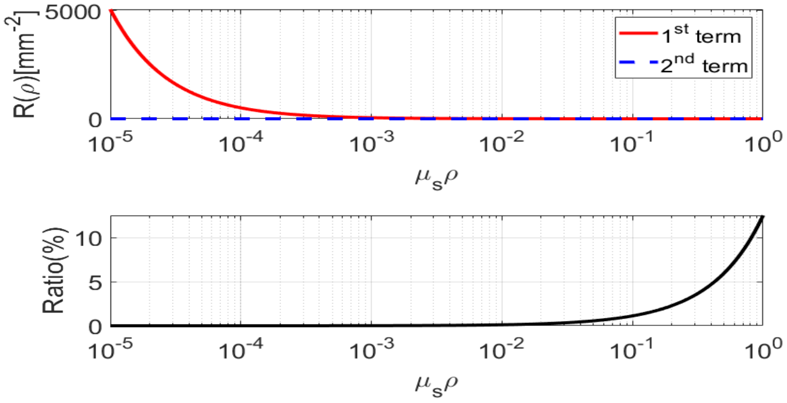

Figure A-1 (A) The absolute values of the two terms of Eq. (III.12). (B) The relative value of the second term versus the first term.

APPENDIX B: The upper limit of the total diffuse radiance from a center-illuminated and an area-collected round-geometry corresponding to isotropic tissue scattering

We use the special case of a homogeneous infinite medium that is isotropic and free of absorption to estimate the upper limit of the diffuse radiance in a center-illuminated and area-collected geometry that has the same lateral dimension as the one given in. This upper limit of the diffuse radiance, when adding the absorption effect, also enlightens the form of the diffuse irradiance at near-the-entry, following which the near-field model of Eq. (IV.5) has been developed.

Consider the homogeneous, isotropic, and non-absorbing infinite medium as shown in Figure A-2. The light of intensity 1 (W$\cdot\ mm^{-3}$) that is injected at a position within the medium (the origin of the coordinate) will experience the first isotropic scattering event at a distance of $1/\mu_s$ from the position of injection and long the direction of injection. The resulted radiance will be distributed uniformly over the entire 4π steradian. If the medium does not absorb, the total radiance on a spherical surface centered at the first scattering event remains constant (equaling the source intensity). Now we evaluate the total radiance at a thin circular strip on the plane lateral to the light injection and at the origin that has a radius of ρ and a differential thickness of $d\rho$. The area of the circular strip is $2\pi\rho \cdot d\rho$, and the distance of any segment of the circular strip to the position of the first scattering event is $\sqrt{\rho^2 + (1/\mu_s)^2}$. As a result the differential spatial angle that this circular strip forms with respect to the position of the first scattering event is $d\Omega = 2\pi\rho \cdot d\rho/[\rho^2 + (1/\mu_s)^2]$. The total irradiance $dI(\rho)$ received by this circular strip is thus

$$dI(\rho) = \frac{d\Omega}{4\pi} = \frac{1}{4\pi}\frac{2\pi\rho\cdot d\rho}{\rho^2+(1/\mu_s)^2} = \frac{1}{2}\mu_s\frac{\mu_s\rho}{(\mu_s\rho)^2+1}d\rho$$

Integration of Eq. (A.1) from the origin to ρ gives the total radiance $I(\rho)$ over the circular area of radius ρ as the following

$$I(\rho) = \int_0^\rho dI(\rho) = \frac{1}{4}\mu_s \int_0^\rho \frac{2\mu_s\rho}{(\mu_s\rho)^2+1} d\rho = \frac{1}{4} ln[(\mu_s\rho)^2 + 1]$$

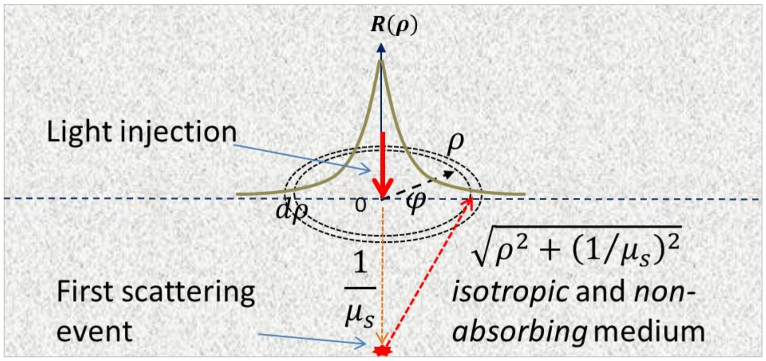

Figure A-2 (A) The depth of the slave-source as determined by the term $(1-\eta)$, thus represents $(z_a z_a^*)(\mu_s)^2$. (B) The relative intensity of the slave-source with respect to the product of the intensity S and the tissue property dependent term, as a function of g, at different.

Equation (A.2) sets the limit of the radiance at the circular area that has a scattering coefficient scaled radius of $\mu_s\rho$. This $I(\rho)$ can also be obtained by the integration of the irradiance $R(\rho)$ over the circular are of radius ρ. By defining $\mathbb{R}(\rho) = R(\rho) \cdot \rho$; and $\overbrace{\Re(\rho)} = \int \mathbb{R}(\rho) \cdot d\rho$, we have the following alternative expression of $I(\rho)$:

$$I(\rho) = 2\pi \int_0^\rho R(\rho) \cdot \rho \cdot d\rho = 2\pi \int_0^\rho \mathbb{R}(\rho) \cdot d\rho$$

$$= 2\pi \left[\overbrace{\Re(\rho)} - \overbrace{\Re(0)}\right] = \frac{1}{4}\left[ln[(\mu_s\rho)^2 + 1] - ln[(\mu_s 0)^2 + 1]\right]$$

With Eq. (A.3), we can have

$$\overbrace{\Re(\rho)} = \frac{1}{8\pi} ln[(\mu_s\rho)^2 + 1]$$

And

$$R(\rho) = \frac{1}{\rho}\frac{d}{d\rho}\overbrace{\Re(\rho)} = \frac{1}{4\pi}\frac{(\mu_s)^2}{(\mu_s\rho)^2+1}$$

When there is absorption and there

$$R(\rho) = \frac{1}{4\pi}\frac{(\mu_s)^2}{(\mu_s\rho)^2+1}exp\left(-2\mu_a\frac{1}{\mu_s}\right)$$

APPENDIX C: Relations and approximations when scattering approaches infinite

n=10, g=0.9, $n_{tiss} = 1.4$, $\delta = 0.5$

$$\eta = [g \cdot exp(1-g)]^{1/n} = 0.999$$

$$\alpha = (1-g)^2(1-\eta) = 5.36 \times 10^{-6}$$

$$\xi = -1.44{n_{tiss}}^{-2} + 0.710{n_{tiss}}^{-1} + 0.668 + 0.0636n_{tiss}.$$

$$A = \frac{1+\xi}{1-\xi} = 3.255$$

$$\alpha \ll \delta < 1 < \left(\alpha + \frac{4A}{3}\right) < (1 + \frac{4A}{3})$$

When $\mu_s' \to \infty$

$$z_a = \frac{1}{\mu_s'} \to 0$$

$$D = \frac{1}{[3(\mu_a + \mu_s')]} \to \frac{1}{3\mu_s'} = \frac{1}{3} z_a \to 0$$

$$\beta = \frac{z_b}{z_a} = \frac{2AD}{z_a} = \frac{2A\mu_s'}{[3(\mu_a + \mu_s')]} \to \frac{2A}{3}$$

$$z_a^* = \alpha z_{\boldsymbol{a}} \to 0$$

$$z_b = \beta z_a \to 0$$

$$\mu_{eff} = \sqrt{\frac{\mu_a}{D}} = \sqrt{3\mu_a(\mu_a + \mu_s')} \rightarrow \sqrt{\frac{3\mu_a}{z_a}} \rightarrow \infty$$

$$\mu_{eff}D = \sqrt{\mu_a D} = \sqrt{\frac{\mu_a}{[3(\mu_a + \mu_s')]}} \rightarrow \sqrt{\frac{\mu_a z_a}{3}} \rightarrow 0$$

$$\mu_{eff}z_a = \frac{\mu_{eff}}{\mu_s'} = \frac{\sqrt{3\mu_a(\mu_a + \mu_s')}}{\mu_s'} = \sqrt{\frac{3\mu_a(\mu_a + \mu_s')}{[\mu_s']^2}} \rightarrow \sqrt{3\mu_a z_a} \rightarrow 0$$

$$\mu_{eff}z_a^* = \alpha\mu_{eff}z_a \rightarrow 0$$

$$\mu_{eff}z_b = 2AD\mu_{eff} \rightarrow 2A\sqrt{\frac{\mu_a z_a}{3}} \rightarrow 0$$

$$S^* = S \cdot \exp\left(-\mu_{eff}\frac{z_a + z_a^*}{2}\right) \cdot \eta \rightarrow S \cdot \left(1 - \mu_{eff}\frac{z_a + z_a^*}{2}\right) \cdot \eta = S\left(1 - \mu_{eff}z_a\frac{1 + \alpha}{2}\right)\eta \rightarrow S\eta$$

APPENDIX D: The calculation of the first term in section 5.2.2.a

As $\mu_s' \to \infty$, $x = \mu_{eff} z_a = \frac{\mu_{eff}}{\mu_s'} = \frac{\sqrt{3\mu_a(\mu_a+\mu_s')}}{\mu_s'} = \sqrt{\frac{3\mu_a(\mu_a+\mu_s')}{[\mu_s']^2}} \to 0.$

$$\frac{3}{8\sqrt{2}\pi} \lim_{x\to 0} \frac{exp\left(-x\sqrt{\delta^2+1}\right) - exp\left(-x\sqrt{\delta^2+(1+2\beta)^2}\right)}{x}$$

$$= \frac{3}{8\sqrt{2}\pi} \lim_{x\to 0} \frac{exp\left(-\mu_{eff} z_a\sqrt{\delta^2+1}\right)\left(-\sqrt{\delta^2+1}\right) - exp\left(x\sqrt{\delta^2+(1+2\beta)^2}\right)\left(-\sqrt{\delta^2+(1+2\beta)^2}\right)}{1}$$

$$= \frac{3}{8\sqrt{2}\pi} \lim_{x\to 0} \frac{\left(-\sqrt{\delta^2+1}\right) - \left(-\sqrt{\delta^2+(1+2\beta)^2}\right)}{1}$$

$$= \frac{3}{8\sqrt{2}\pi} \lim_{\mu_s'\to\infty} (\sqrt{\delta^2+(1+2\beta)^2} - \sqrt{\delta^2+1})$$

$$= \frac{3}{8\sqrt{2}\pi} \left[\sqrt{\delta^2+\left(1+\frac{4A}{3}\right)^2} - \sqrt{\delta^2+1}\right]$$

APPENDIX E: The calculation of the second term in section 5.2.2.a

The following Taylor series expansion is applied in later derivation.

$$\sqrt{b^2 + (z_a)^2} = b + \frac{(z_a)^2}{2b}$$

$$\sqrt{b^2 + (z_a + 2z_b)^2} = b + \frac{(z_a + 2z_b)^2}{2b}$$

$$exp\left(-\mu_{eff}\frac{(z_a)^2}{2b}\right) = (1-\mu_{eff}\frac{(z_a)^2}{2b})$$

$$exp\left(-\mu_{eff}\frac{(z_a + 2z_b)^2}{2b}\right) = (1-\mu_{eff}\frac{(z_a + 2z_b)^2}{2b})$$

$$\lim_{\mu_s'\to\infty}\frac{1}{8\sqrt{2}\pi}\left[\frac{exp\left(-\mu_{eff}\sqrt{b^2+(z_a)^2}\right) - exp\left(-\mu_{eff}\sqrt{b^2+(z_a+2z_b)^2}\right)}{D\mu_{eff}}\right]$$

$$= \lim_{\mu_s'\to\infty}\frac{1}{8\sqrt{2}\pi}\frac{\left(exp\left(-\mu_{eff}\left(b+\frac{(z_a)^2}{2b}\right)\right) - exp\left(-\mu_{eff}\left(b+\frac{(z_a+2z_b)^2}{2b}\right)\right)\right)}{D\mu_{eff}}$$

$$= \lim_{\mu_s'\to\infty}\frac{1}{8\sqrt{2}\pi}\frac{\left(exp\left(-\mu_{eff}b\right)exp(-\mu_{eff}\frac{(z_a)^2}{2b}) - exp\left(-\mu_{eff}b\right)exp(-\mu_{eff}\frac{(z_a+2z_b)^2}{2b})\right)}{D\mu_{eff}}$$

$$= \lim_{\mu_s'\to\infty}\frac{1}{8\sqrt{2}\pi}\frac{\left(exp\left(-\mu_{eff}b\right)(1-\mu_{eff}\frac{(z_a)^2}{2b}) - exp\left(-\mu_{eff}b\right)(1-\mu_{eff}\frac{(z_a+2z_b)^2}{2b})\right)}{D\mu_{eff}}$$

$$= \lim_{\mu_s' \to \infty} \frac{1}{8\sqrt{2}\pi} \exp(-\mu_{eff} b) \frac{\left(\left(1 - \mu_{eff} \frac{(z_a)^2}{2b}\right) - \left(1 - \mu_{eff} \frac{(z_a + 2z_b)^2}{2b}\right)\right)}{D\mu_{eff}}$$

$$= \lim_{\mu_s' \to \infty} \frac{1}{8\sqrt{2}\pi} ex\, p(-\mu_{eff} b) \frac{\left(\mu_{eff} \frac{(z_a + 2z_b)^2}{2b} - \mu_{eff} \frac{(z_a)^2}{2b}\right)}{D\mu_{eff}}$$

$$= \lim_{\mu_s' \to \infty} \frac{1}{8\sqrt{2}\pi} ex\, p(-\mu_{eff} b) \frac{((z_a + 2z_b)^2 - (z_a)^2)}{2bD}$$

$$= \lim_{\mu_s' \to \infty} \frac{1}{8\sqrt{2}\pi} ex\, p(-\mu_{eff} b) \frac{4z_b(z_a + z_b)}{2bD}$$

$$= \lim_{\mu_s' \to \infty} \frac{1}{8\sqrt{2}\pi} ex\, p(-\mu_{eff} b) \frac{4\beta z_a(z_a + \beta z_a)}{2b\frac{1}{3}z_a}$$

$$= \lim_{\mu_s' \to \infty} \frac{3}{8\sqrt{2}\pi} ex\, p(-\mu_{eff} b) \frac{4\beta(1 + \beta)}{\mu_s' d_{area}}$$

$$= \lim_{\mu_s' \to \infty} \frac{3}{8\sqrt{2}\pi} ex\, p(-\mu_{eff} b) \frac{4\beta(1 + \beta)}{\mu_s' d_{area}}$$

APPENDIX F: The calculation of first term in section 5.2.2.b

$$\lim_{x\to 0}\left[\frac{exp\left(-x\sqrt{\delta^2+\alpha^2}\right)-exp\left(-x\sqrt{\delta^2+(\alpha+2\beta)^2}\right)}{x}\right]$$

$$=\lim_{x\to 0}\left[\frac{exp\left(-x\sqrt{\delta^2+\alpha^2}\right)-exp\left(-x\sqrt{\delta^2+(\alpha+2\beta)^2}\right)}{x}\right]$$

$$==\lim_{x\to 0}\left[\frac{exp\left(-x\sqrt{\delta^2+\alpha^2}\right)(-\sqrt{\delta^2+\alpha^2})-exp\left(-x\sqrt{\delta^2+(\alpha+2\beta)^2}\right)(-\sqrt{\delta^2+(\alpha+2\beta)^2})}{1}\right]$$

$$=\lim_{\mu_s'\to\infty}\left(-\sqrt{\delta^2+\alpha^2}\right)+\sqrt{\delta^2+(\alpha+2\beta)^2}$$

$$=\sqrt{\delta^2+\left(\alpha+\frac{4A}{3}\right)^2}-\sqrt{\delta^2+\alpha^2}$$

APPENDIX G: The calculation of second term in section 5.2.2.b

$$\lim_{\mu_s'\to\infty} I^{\Psi^*}_{b\leftrightarrow\infty} = \underset{\mu_s'\to\infty}{lim} \frac{S^*}{8\sqrt{2}\pi}\left[\frac{exp\left(-\mu_{eff}(b+\frac{(\alpha z_a)^{\mathbf{2}}}{2b})\right) - exp\left(-\mu_{eff}(b+\frac{(\alpha z_{\boldsymbol{a}}+2\beta z_a)^2}{2b})\right)}{D\mu_{eff}}\right]$$

$$= \underset{\mu_s'\to\infty}{lim} \frac{S^*}{8\sqrt{2}\pi}\left[\frac{\exp(-\mu_{eff}b)\exp(-\mu_{eff}\frac{(\alpha z_a)^2}{2b}) - exp(-\mu_{eff}b)\, exp(-\mu_{eff}\frac{(\alpha z_{\boldsymbol{a}}+2\beta z_a)^2}{2b})}{D\mu_{eff}}\right]$$

$$= \underset{\mu_s'\to\infty}{lim} \frac{S^*}{8\sqrt{2}\pi}\left[exp(-\mu_{eff}b)\frac{\left(1-\mu_{eff}\frac{(\alpha z_a)^2}{2b}\right) - (1-\mu_{eff}\frac{(\alpha z_{\boldsymbol{a}}+2\beta z_a)^2}{2b})}{D\mu_{eff}}\right]$$

$$= \underset{\mu_s'\to\infty}{lim} \frac{S^*}{8\sqrt{2}\pi}\left[exp(-\mu_{eff}b)\frac{\left(\mu_{eff}\frac{(\alpha z_{\boldsymbol{a}}+2\beta z_a)^2}{2b} - \mu_{eff}\frac{(\boldsymbol{\alpha z_a})^{\mathbf{2}}}{2b}\right)}{D\mu_{eff}}\right]$$

$$= \underset{\mu_s'\to\infty}{lim} \frac{S^*}{8\sqrt{2}\pi}\left[exp(-\mu_{eff}b)\frac{\left(\frac{4\beta \boldsymbol{z_a}^{\mathbf{2}}}{2b}(\alpha+\beta)\right)}{D}\right]$$

$$D = \frac{1}{[3(\mu_a+\mu_s')]} \to \frac{1}{3\mu_s'} = \frac{1}{3}z_a$$

$$\frac{\left(\frac{4\beta \boldsymbol{z_a}^{\mathbf{2}}}{2b}(\alpha+\beta)\right)}{D} = \frac{\left(\frac{4\beta \boldsymbol{z_a}^{\mathbf{2}}}{2b}(\alpha+\beta)\right)}{\frac{1}{3}z_a} = \left(\frac{12\beta \boldsymbol{z_a}}{2b}(\alpha+\beta)\right) = \left(\frac{12\beta}{\mu_s' d_{area}}(\alpha+\beta)\right)$$

$$= \underset{\mu_s'\to\infty}{lim} \frac{S^*}{8\sqrt{2}\pi}\left[exp(-\mu_{eff}b)\left(\frac{12\beta}{\mu_s' d_{area}}(\alpha+\beta)\right)\right]$$

$$= \lim_{\mu_s' \to \infty} \frac{3\eta}{8\sqrt{2}\pi} \left[exp\left(-\mu_{eff} b\right) \left(\frac{4\beta(\alpha + \beta)}{\mu_s' d_{area}} \right) \right]$$

$$= \lim_{\mu_s' \to \infty} \frac{3\eta}{8\sqrt{2}\pi} \left[exp\left(-\mu_{eff} b\right) \left(\frac{\frac{8A}{3}(\alpha + \frac{2A}{3})}{\mu_s' d_{area}} \right) \right]$$

APPENDIX H: The calculation of second term in section 5.2.2.c

Apply Taylor series expansion

$$\sqrt{b^2+(z_a)^2} = b + \frac{(z_a)^2}{2b}$$

$$\sqrt{b^2+(z_a+2z_b)^2} = b + \frac{(z_a+2z_b)^2}{2b}$$

$$\lim_{\mu_s'\to\infty} I^{JZ}_{b\leftrightarrow\infty} = \lim_{\mu_s'\to\infty} \frac{3}{8\sqrt{2}\pi}\left[\frac{z_a}{\sqrt{b^2+(z_a)^2}} exp\left(-\mu_{eff}\sqrt{b^2+(z_a)^2}\right)\right.$$

$$\left. + \frac{(z_a+2z_b)}{\sqrt{b^2+(z_a+2z_b)^2}} exp\left(-\mu_{eff}\sqrt{b^2+(z_a+2z_b)^2}\right)\right]$$

$$= \lim_{\mu_s'\to\infty} \frac{3}{8\sqrt{2}\pi}\left[\frac{z_a}{\sqrt{b^2+(z_a)^2}} exp\left(-\mu_{eff}\left(b+\frac{(z_a)^2}{2b}\right)\right)\right.$$

$$\left. + \frac{(z_a+2z_b)}{\sqrt{b^2+(z_a+2z_b)^2}} exp\left(-\mu_{eff}\left(b+\frac{(z_a+2z_b)^2}{2b}\right)\right)\right]$$

$$= \lim_{\mu_s'\to\infty} \frac{3}{8\sqrt{2}\pi}\left[\frac{z_a}{\sqrt{b^2+(z_a)^2}} exp\left(-\mu_{eff}b\right) exp(-\mu_{eff}\frac{(z_a)^2}{2b})\right.$$

$$\left. + \frac{(z_a+2z_b)}{\sqrt{b^2+(z_a+2z_b)^2}} exp\left(-\mu_{eff}b\right) exp(-\mu_{eff}\frac{(z_a+2z_b)^2}{2b})\right]$$

$$
\begin{aligned}
= \lim_{\mu_s' \to \infty} \frac{3}{8\sqrt{2}\pi} exp\left(-\mu_{eff} b\right) \Bigg[& \frac{z_a}{\sqrt{b^2 + (z_a)^2}} (1 - \mu_{eff} \frac{(z_a)^2}{2b}) \\
& + \frac{(z_a + 2z_b)}{\sqrt{b^2 + (z_a + 2z_b)^2}} (1 - \mu_{eff} \frac{(z_a + 2z_b)^2}{2b}) \Bigg]
\end{aligned}
$$

$$
\begin{aligned}
= \lim_{\mu_s' \to \infty} \frac{3}{8\sqrt{2}\pi} exp\left(-\mu_{eff} b\right) \Bigg\{ & \left(\frac{z_a}{\sqrt{b^2 + (z_a)^2}} + \frac{(z_a + 2z_b)}{\sqrt{b^2 + (z_a + 2z_b)^2}} \right) \\
& - \frac{\mu_{eff} z_a}{2b} \left[\frac{(z_a)^2}{\sqrt{b^2 + (z_a)^2}} + (1 + 2\beta) \frac{(z_a + 2z_b)^2}{\sqrt{b^2 + (z_a + 2z_b)^2}} \right] \Bigg\}
\end{aligned}
$$

Refer to Appendix 2, when $\mu_s' \to \infty$, $z_a \to 0$. We apply following approximating by discarding the second order small variable $(z_a)^2$ appearing at denominator.

$$
\left(\frac{z_a}{\sqrt{b^2 + (z_a)^2}} + \frac{(z_a + 2z_b)}{\sqrt{b^2 + (z_a + 2z_b)^2}} \right) = \left(\frac{z_a}{b} + \frac{(z_a + 2z_b)}{b} \right) = \frac{2z_a(1 + \beta)}{b} = \frac{4(1 + \beta)}{\mu_s' d_{area}}
$$

$$
\begin{aligned}
& \frac{\mu_{eff} z_a}{2b} \left[\frac{(z_a)^2}{\sqrt{b^2 + (z_a)^2}} + (1 + 2\beta) \frac{(z_a + 2z_b)^2}{\sqrt{b^2 + (z_a + 2z_b)^2}} \right] \\
& \qquad = \frac{\mu_{eff} z_a}{2b} \left[\frac{(z_a)^2}{b} + (1 + 2\beta) \frac{(z_a + 2z_b)^2}{b} \right] = \frac{2\mu_{eff} z_a}{2b} \frac{(z_a)^2}{2b} [1 + (1 + 2\beta)^3] \\
& \qquad = \frac{2\mu_{eff} z_a}{(\mu_s' d_{area})^2} [1 + (1 + 2\beta)^3]
\end{aligned}
$$

$$
= \lim_{\mu_s' \to \infty} \frac{3}{8\sqrt{2}\pi} exp\left(-\mu_{eff} b\right) \left\{ \frac{4(1 + \beta)}{\mu_s' d_{area}} - \frac{2\mu_{eff} z_a}{(\mu_s' d_{area})^2} [1 + (1 + 2\beta)^3] \right\}
$$

$$
= \lim_{\mu_s' \to \infty} \frac{3}{8\sqrt{2}\pi} exp\left(-\mu_{eff} b\right) \frac{4(1 + \beta)}{\mu_s' d_{area}} = \lim_{\mu_s' \to \infty} \frac{3}{8\sqrt{2}\pi} exp\left(-\mu_{eff} b\right) \frac{4\left(1 + \frac{2A}{3}\right)}{\mu_s' d_{area}}
$$

APPENDIX I: The calculation of second term in section 5.2.2.d

Apply Taylor series expansion

$$\sqrt{b^2 + (z_a^*)^2} = b + \frac{(z_a^*)^2}{2b}$$

$$\sqrt{b^2 + (z_a^* + 2z_b)^2} = b + \frac{(z_a^* + 2z_b)^2}{2b}$$

$$\lim_{\mu_s' \to \infty} I_{b \leftrightarrow \infty}^{\mathrm{JZ}^*} = \underset{\mu_s' \to \infty}{lim} \frac{3S^*}{8\sqrt{2}\pi} \left[\frac{z_a^*}{\sqrt{b^2 + (z_a^*)^2}} exp\left(-\mu_{eff}\sqrt{b^2 + (z_a^*)^2}\right) \right.$$

$$\left. + \frac{(z_a^* + 2z_b)}{\sqrt{b^2 + (z_a^* + 2z_b)^2}} \exp\left(-\mu_{eff}\sqrt{b^2 + (z_a^* + 2z_b)^2}\right) \right]$$

$$= \underset{\mu_s' \to \infty}{lim} \frac{3S^*}{8\sqrt{2}\pi} \left[\frac{z_a^*}{\sqrt{b^2 + (z_a^*)^2}} exp\left(-\mu_{eff}\left(b + \frac{(z_a^*)^2}{2b}\right)\right) \right.$$

$$\left. + \frac{(z_a^* + 2z_b)}{\sqrt{b^2 + (z_a^* + 2z_b)^2}} exp\left(-\mu_{eff}\left(b + \frac{(z_a^* + 2z_b)^2}{2b}\right)\right) \right]$$

$$= \underset{\mu_s' \to \infty}{lim} \frac{3S^*}{8\sqrt{2}\pi} \left[\frac{z_a^*}{\sqrt{b^2 + (z_a^*)^2}} exp\left(-\mu_{eff} b\right) exp(-\mu_{eff} \frac{(z_a^*)^2}{2b}) \right.$$

$$\left. + \frac{(z_a^* + 2z_b)}{\sqrt{b^2 + (z_a^* + 2z_b)^2}} exp\left(-\mu_{eff} b\right) exp(-\mu_{eff} \frac{(z_a^* + 2z_b)^2}{2b}) \right]$$

$$= \underset{\mu_s' \to \infty}{lim} \frac{3S^*}{8\sqrt{2}\pi} exp\left(-\mu_{eff} b\right) \left[\frac{z_a^*}{\sqrt{b^2 + (z_a^*)^2}} (1 - \mu_{eff} \frac{(z_a^*)^2}{2b}) \right.$$

$$\left. + \frac{(z_a^* + 2z_b)}{\sqrt{b^2 + (z_a^* + 2z_b)^2}} (1 - \mu_{eff} \frac{(z_a^* + 2z_b)^2}{2b}) \right]$$

$$= \lim_{\mu_s'\to\infty} \frac{3S^*}{8\sqrt{2}\pi} exp\left(-\mu_{eff}b\right)\left\{\left(\frac{z_a^*}{\sqrt{b^2+(z_a^*)^2}} + \frac{(z_a^*+2z_b)}{\sqrt{b^2+(z_a^*+2z_b)^2}}\right)\right.$$

$$\left. - \frac{\mu_{eff}{z_a}^3}{2b}\left[\frac{\alpha^3}{\sqrt{b^2+(z_a)^2}} + \frac{(1+2\beta)^3}{\sqrt{b^2+(z_a+2z_b)^2}}\right]\right\}$$

Refer to Appendix 2, when $\mu_s' \to \infty, z_a \to 0$. We apply following approximating by discarding the second order small variable $(z_a)^2$ appearing at denominator.

$$\left(\frac{z_a^*}{\sqrt{b^2+(z_a^*)^2}} + \frac{(z_a^*+2z_b)}{\sqrt{b^2+(z_a^*+2z_b)^2}}\right) = \left(\frac{z_a^*}{b} + \frac{(z_a^*+2z_b)}{b}\right) = \frac{2z_a(\alpha+\beta)}{b} = \frac{4(\alpha+\beta)}{\mu_s' d_{area}}$$

$$\frac{\mu_{eff}{z_a}^3}{2b}\left[\frac{\alpha^3}{\sqrt{b^2+(z_a)^2}} + \frac{(1+2\beta)^3}{\sqrt{b^2+(z_a+2z_b)^2}}\right] = \frac{\mu_{eff}{z_a}^3}{2b}\left[\frac{\alpha^3}{b} + \frac{(1+2\beta)^3}{b}\right]$$

$$= \frac{2\mu_{eff}z_a}{2b}\frac{(z_a)^2}{2b}\left[\alpha^3+(1+2\beta)^3\right] = \frac{2\mu_{eff}z_a}{(\mu_s' d_{area})^2}\left[\alpha^3+(1+2\beta)^3\right]$$

$$\lim_{\mu_s'\to\infty} I_{b\leftrightarrow\infty}^{\mathrm{JZ}^*} = \lim_{\mu_s'\to\infty} \frac{3S^*}{8\sqrt{2}\pi} exp\left(-\mu_{eff}b\right)\left\{\frac{4(\alpha+\beta)}{\mu_s' d_{area}} - \frac{2\mu_{eff}z_a}{(\mu_s' d_{area})^2}\left[\alpha^3+(1+2\beta)^3\right]\right\}$$

$$= \frac{3\eta}{8\sqrt{2}\pi}\lim_{\mu_s'\to\infty} exp\left(-\mu_{eff}b\right)\left\{\frac{4(\alpha+\beta)}{\mu_s' d_{area}}\right\}$$

$$= \frac{3\eta}{8\sqrt{2}\pi}\lim_{\mu_s'\to\infty} exp\left(-\mu_{eff}b\right)\left\{\frac{4\left(\alpha+\frac{2A}{3}\right)}{\mu_s' d_{area}}\right\}$$

APPENDIX J: The derivation of flux -z component in section 6.2.2.b

$$\vec{J}_{semi}(\rho,t) = \vec{J}_{inf}^{\mathrm{real}} + \vec{J}_{inf}^{\mathrm{imag}}$$

$$\vec{J}_{inf}^{\mathrm{real}} = -D\frac{\partial\Psi_{inf}^{\mathrm{real}}}{\partial \mathrm{l}_{\mathrm{real}}}\hat{l}_{real} = -D\frac{Sc}{(4\pi Dct)^{\frac{3}{2}}}\exp(-\mu_a ct)\frac{\partial \exp\left(-\frac{l_{real}^2}{4Dct}\right)}{\partial \mathrm{l}_{\mathrm{real}}}\hat{l}_{real}$$

$$= -D\frac{Sc}{(4\pi Dct)^{\frac{3}{2}}}\exp(-\mu_a ct)\frac{-2l_{real}}{4Dct}\exp\left(-\frac{l_{real}^2}{4Dct}\right)\hat{l}_{real}$$

$$= \frac{S}{2t(4\pi Dct)^{\frac{3}{2}}}\exp(-\mu_a ct)l_{real}\exp\left(-\frac{l_{real}^2}{4Dct}\right)\hat{l}_{real}$$

$$\vec{J}_{inf}^{\mathrm{imag}} = -D\frac{\partial\Psi_{inf}^{imag}}{\partial \mathrm{l}_{\mathrm{imag}}}\hat{l}_{imag} = \frac{-S}{2t(4\pi Dct)^{\frac{3}{2}}}\exp(-\mu_a ct)l_{imag}\exp\left(-\frac{l_{imag}^2}{4Dct}\right)\hat{l}_{imag}$$

$$\vec{J}_{semi}(\rho,t) = \frac{S}{2t(4\pi Dct)^{\frac{3}{2}}}\exp(-\mu_a ct)\;[l_{real}\exp\left(-\frac{l_{real}^2}{4Dct}\right)\hat{l}_{real} - l_{imag}\exp\left(-\frac{l_{imag}^2}{4Dct}\right)\hat{l}_{imag}]$$

For master source,

$$J_{semi}^{m}|_{-z}(\rho,t) = \frac{S}{2t(4\pi Dct)^{\frac{3}{2}}}\exp(-\mu_a ct)\;[l_{real}^{m}\exp\left(-\frac{(l_{real}^{m})^2}{4Dct}\right)\frac{z_a}{l_{real}^{m}}$$

$$+\,l_{imag}^{m}\exp\left(-\frac{(l_{imag}^{m})^2}{4Dct}\right)\frac{(z_a+2z_b)}{l_{imag}^{m}}$$

$$J_{semi}^{m}|_{-z}(\rho,t) = \frac{S}{2t(4\pi Dct)^{\frac{3}{2}}} \exp(-\mu_a ct)\,[z_a \exp\left(-\frac{(l_{real}^{m})^2}{4Dct}\right) + (z_a + 2z_b)\exp\left(-\frac{(l_{imag}^{m})^2}{4Dct}\right)]$$

Similarly, for slave source,

$$J_{semi}^{s}|_{-z}(\rho,t) = \frac{S^*}{2t(4\pi Dct)^{\frac{3}{2}}} \exp(-\mu_a ct)\,[z_a^* \exp\left(-\frac{(l_{real}^{s})^2}{4Dct}\right) + (z_a^* + 2z_b)\exp\left(-\frac{(l_{imag}^{s})^2}{4Dct}\right)]$$

APPENDIX K: Matlab code of steady-state model of total diffuse reflectance in Chapter IV

```
function [Hybrid_SF]...    % calcualte the TDF in substraction method
    = model_hybrid_sub(mua, g, mus, Nrel, Rfib, delta)

b = Rfib;
Trans = 0.9988; % transimission
border = delta/(mus*(1-g));
Dfib = 2*Rfib;

p2 = 0.1;  %
p3 = 2*Dfib + 0.2;

if ( b <= border)  % inner-field convers entire fiber, equ (13)
     musp = mus*(1-g);
     MUSP = 1;
     MUS = MUSP/(1-g);
     B = b*musp /MUSP; % musp*dfib are same
     XIB = B/(1/MUSP);
     GAMMA = 2*mua/MUS;

     Hybrid_SF = (0.75^g)*10^(-(1+p3*GAMMA))*((1-g)^g)*exp(-GAMMA)/(1-
p2*GAMMA)*(XIB/(1-g))^(1-p2*GAMMA);  % v1228

elseif(border < b)   % equ (27)
    %% inner-field integral, from zero to delta*Za, equ (16)

     MUSP = 1;
     MUS = MUSP/(1-g);
     GAMMA = 2*mua/MUS;

     Nearmodel_SF = (0.75^g)*10^(-(1+p3*GAMMA))*((1-g)^g)*exp(-
GAMMA)/(1-p2*GAMMA)*(delta/(1-g))^(1-p2*GAMMA);  % v1228

    %% far-field integral, from border to Rfib = Farfield(delta*Za -->
inf) - Farfield(b --> inf), eqn (15-27)


    n = 10;
    S = 1;

    musp = mus*(1-g); % unit = um^-1
    D = 1/(3*(mua + musp)); % unit = um
    mueff = sqrt(mua/D); % unit = um^-1
    Za = 1/musp;     % unit = um
```

```
    eta = (g*exp(1-g))^(1/n);
    alpha = (1-g)^2*(1-eta);
    Zas = alpha*Za;    % unit = um
    Ss = S*exp(-mueff*(Za + Zas)/2)*eta;

    ksi = -1.44*Nrel^(-2) + 0.71*Nrel^(-1) + 0.668 + 0.0636*Nrel;
    A = (1+ksi)/(1-ksi);
    Zb = 2*A*D; % unit = um
    beta = Zb/Za;

    XIB = b/Za;


    Im_phi_delta2inf = S/(8*sqrt(2)*pi*D*mueff)*(exp(-
mueff*Za*sqrt(delta^2 + 1))- exp(-mueff*Za*sqrt(delta^2 +
(1+2*beta)^2))); % eqn(19)

    Im_phi_b2inf =     S/(8*sqrt(2)*pi*D*mueff)*(exp(-
mueff*Za*sqrt(XIB^2 + 1))- exp(-mueff*Za*sqrt(XIB^2 + (1+2*beta)^2)));
% eqn(20)


    Is_phi_delta2inf = Ss/(8*sqrt(2)*pi*D*mueff)*(exp(-
mueff*Za*sqrt(delta^2 + alpha^2))- exp(-mueff*Za*sqrt(delta^2 +
(alpha^2+2*beta)^2))); % eqn(21)

    Is_phi_b2inf =     Ss/(8*sqrt(2)*pi*D*mueff)*(exp(-
mueff*Za*sqrt(XIB^2 + alpha^2))- exp(-mueff*Za*sqrt(XIB^2 +
(alpha^2+2*beta)^2))); % eqn(22)


    Im_jz_delta2inf = 3*S/(8*sqrt(2)*pi)*(1/sqrt(delta^2+1)*exp(-
mueff*Za*sqrt(delta^2+1)) + ...

(1+2*beta)/sqrt(delta^2+(1+2*beta)^2)*exp(-
mueff*Za*sqrt(delta^2+(1+2*beta)^2))); % eqn(23)

    Im_jz_b2inf = 3*S/(8*sqrt(2)*pi)*(1/sqrt(XIB^2+1)*exp(-
mueff*Za*sqrt(XIB^2+1)) + ...

(1+2*beta)/sqrt(XIB^2+(1+2*beta)^2)*exp(-
mueff*Za*sqrt(XIB^2+(1+2*beta)^2)));  % eqn(24)

    Is_jz_delta2inf =
3*Ss/(8*sqrt(2)*pi)*(alpha/sqrt(delta^2+alpha^2)*exp(-
mueff*Za*sqrt(delta^2+alpha^2)) + ...

(alpha+2*beta)/sqrt(delta^2+(alpha+2*beta)^2)*exp(-
mueff*Za*sqrt(delta^2+(alpha+2*beta)^2))); % eqn(25)

    Is_jz_b2inf = 3*Ss/(8*sqrt(2)*pi)*(alpha/sqrt(XIB^2+alpha^2)*exp(-
mueff*Za*sqrt(XIB^2+alpha^2)) + ...
```

```
(alpha+2*beta)/sqrt(XIB^2+(alpha+2*beta)^2)*exp(-
mueff*Za*sqrt(XIB^2+(alpha+2*beta)^2))); % eqn(26)


    %%

    Hybrid_SF = Nearmodel_SF + Trans*((Im_phi_delta2inf - Im_phi_b2inf)
+ (Is_phi_delta2inf - Is_phi_b2inf) +...
                                      (Im_jz_delta2inf - Im_jz_b2inf) +
(Is_jz_delta2inf - Is_jz_b2inf));

else
    Hybrid_SF = -1;
    disp('check you code');
end
end
```

APPENDIX L: Matlab code of time-domain model of total diffuse reflectance in Chapter VI

```
function [td_Hybrid_SF]...     % calcualte the TDF
    = tdModel(t, mua, g, mus, Nrel, Rfib, delta)

b = Rfib;
Trans = 0.9988; % transimission
border = delta/(mus*(1-g));
c = 3e11; % mm/s;
Dfib = 2*Rfib;

p2 = 0.1;  %
p3 = 2*Dfib + 0.2;


if ( b <= border)  % inner-field convers entire fiber,
     musp = mus*(1-g);
     MUSP = 1;
     MUS = MUSP/(1-g);
     B = b*musp /MUSP; % musp*dfib are same
     XIB = B/(1/MUSP);
     GAMMA = 2*mua/MUS;

     td_Hybrid_SF = (0.75^g)*10^(-(1+p3*GAMMA))*((1-g)^g)*exp(-
GAMMA)/(1-p2*GAMMA)*(XIB/(1-g))^(1-p2*GAMMA)*mua*c*exp(-mua*c*t); %
v1228

elseif(border < b)
    %% inner-field integral, from zero to delta*Za,

     MUSP = 1;
     MUS = MUSP/(1-g);
     GAMMA = 2*mua/MUS;

     Nearmodel_SF = (0.75^g)*10^(-(1+p3*GAMMA))*((1-g)^g)*exp(-
GAMMA)/(1-p2*GAMMA)*(delta/(1-g))^(1-p2*GAMMA)*mua*c*exp(-mua*c*t);  %
v1228


    n = 10;
    S = 1;

    musp = mus*(1-g); % unit = um^-1
    D = 1/(3*(mua + musp)); % unit = um
    mueff = sqrt(mua/D); % unit = um^-1
```

```
    Za = 1/musp;     % unit = um

    eta = (g*exp(1-g))^(1/n);
    alpha = (1-g)^2*(1-eta);
    Zas = alpha*Za;    % unit = um
    Ss = S*exp(-mueff*(Za + Zas)/2)*eta;

    ksi = -1.44*Nrel^(-2) + 0.71*Nrel^(-1) + 0.668 + 0.0636*Nrel;
    A = (1+ksi)/(1-ksi);
    Zb = 2*A*D; % unit = um
    beta = Zb/Za;

    XIB = b/Za;


    Im_phi_delta2inf = 1/(8*sqrt(2)*pi^(3/2))*S*c/sqrt(D*c*t)*exp(-
mua*c*t)*(exp(-(delta^2+1)/(4*D*c*t)*Za^2) - exp(-
(delta^2+(1+2*beta)^2)/(4*D*c*t)*Za^2)); %

    Im_phi_b2inf = 1/(8*sqrt(2)*pi^(3/2))*S*c/sqrt(D*c*t)*exp(-
mua*c*t)*(exp(-(XIB^2+1)/(4*D*c*t)*Za^2) - exp(-
(XIB^2+(1+2*beta)^2)/(4*D*c*t)*Za^2)); %


    Is_phi_delta2inf = 1/(8*sqrt(2)*pi^(3/2))*Ss*c/sqrt(D*c*t)*exp(-
mua*c*t)*(exp(-(delta^2+alpha^2)/(4*D*c*t)*Za^2) - exp(-
(delta^2+(alpha+2*beta)^2)/(4*D*c*t)*Za^2)); %

    Is_phi_b2inf = 1/(8*sqrt(2)*pi^(3/2))*Ss*c/sqrt(D*c*t)*exp(-
mua*c*t)*(exp(-(XIB^2+alpha^2)/(4*D*c*t)*Za^2) - exp(-
(XIB^2+(alpha+2*beta)^2)/(4*D*c*t)*Za^2)); %


    Im_jz_delta2inf = 3/(16*sqrt(2)*pi^(3/2))*S/(t*sqrt(D*c*t))*exp(-
mua*c*t)*(Za*exp(-(delta^2+1)/(4*D*c*t)*Za^2) + (Za+2*Zb)*exp(-
(delta^2+(1+2*beta)^2)/(4*D*c*t)*Za^2));

    Im_jz_b2inf = 3/(16*sqrt(2)*pi^(3/2))*S/(t*sqrt(D*c*t))*exp(-
mua*c*t)*(Za*exp(-(XIB^2+1)/(4*D*c*t)*Za^2) + (Za+2*Zb)*exp(-
(XIB^2+(1+2*beta)^2)/(4*D*c*t)*Za^2));


    Is_jz_delta2inf = 3/(16*sqrt(2)*pi^(3/2))*Ss/(t*sqrt(D*c*t))*exp(-
mua*c*t)*(Za*exp(-(delta^2+alpha^2)/(4*D*c*t)*Za^2) + (Za+2*Zb)*exp(-
(delta^2+(alpha+2*beta)^2)/(4*D*c*t)*Za^2));

    Is_jz_b2inf = 3/(16*sqrt(2)*pi^(3/2))*Ss/(t*sqrt(D*c*t))*exp(-
mua*c*t)*(Za*exp(-(XIB^2+alpha^2)/(4*D*c*t)*Za^2) + (Za+2*Zb)*exp(-
(XIB^2+(alpha+2*beta)^2)/(4*D*c*t)*Za^2));

    %%
```

```
    td_Hybrid_SF = Nearmodel_SF + Trans*((Im_phi_delta2inf - 
Im_phi_b2inf) + (Is_phi_delta2inf - Is_phi_b2inf) +...
                                      (Im_jz_delta2inf - Im_jz_b2inf) + 
(Is_jz_delta2inf - Is_jz_b2inf));

else
    td_Hybrid_SF = -1;
    disp(‘check your code');
end


end
```

VITA

Tengfei Sun

Candidate for the Degree of

Doctor of Philosophy

Dissertation: MODELS AND METHODS OF QUANTITATIVE SINGLE-FIBER REFLECTANCE SPECTROSCOPY OF TISSUE PROPERTIES

Major Field: Electrical Engineering

Biographical:

Education:

Completed the requirements for the Doctor of Philosophy in Electrical Engineering at Oklahoma State University, Stillwater, Oklahoma in December 2019.

Completed the requirements for the Master of Science in Plasma Physics at Institute of Plasma Physics, University of Chinese Academy of Sciences, Hefei, China in 2013.

Completed the requirements for the Bachelor of Science in Physics at Luoyang Normal University, Luoyang, China in 2010.

Experience:

Dissertation research: Optical spectroscopy models and applications.
Oklahoma State University (8/2014--present)
Research Assistant: 1) Spectroscopic feature associated with rat bladder cancer when evaluated with single-fiber reflectance spectroscopy (8/2014--5/2015); 2) Alternating magnetic field induced heating of magnetic nanoparticles for releasing chemotherapy drug encapsulated in low temperature sensitive liposome. (1/2016--8/2016)
Teaching Assistant of ECEN3714 Network Analysis. (8/2015--present)

Professional Memberships:

Student Member of The International Society for Optics and Photonics
Member of The Optical Society of America Student Chapter of OSU